REVIEW

ADVANCED MATERIALS
www.advmat.de

Electrochemical Cell Designs for Efficient Carbon Dioxide Reduction and Water Electrolysis: Status and Perspectives

Zhangsen Chen, Lei Zhang, Shuhui Sun,* and Gaixia Zhang**

Integrating renewable electricity and concentrated CO_2 from direct air capture, electrochemical CO_2 reduction reactions (eCO_2RR) offer a promising pathway for converting CO_2 into fuel chemicals, enabling the closure of the carbon loop in a sustainable manner. The clean H_2 produced via the hydrogen evolution reaction (HER) during water electrolysis can replace traditional fossil fuels without additional CO_2 emissions. Achieving large-scale and high-efficiency eCO_2RR and HER requires the development of rational electrolyzer designs, which are crucial for industrial implementation. This review examines recent innovations in system designs for eCO_2RR, HER, and the latest advances in in situ cell designs for operando characterization during electrochemical reactions. It focuses on cell improvements in flow patterns, membrane electrode assemblies, and electrolyte engineering to maximize catalytic activities at the industrial level. Besides, the review discusses optimizing counter-anodic reactions to improve the energy efficiency of eCO_2RR and water electrolysis, offering insights into the design of catalytic systems with efficient energy utilization. Furthermore, it explores the integration of eCO_2RR and HER with other electrochemical systems (e.g., fuel cells), highlighting their potential role in the decarbonization of future industrial processes. Finally, the summary, challenge, and outlook on the industrial-scale eCO_2RR and water electrolysis system designs are concluded.

1. Introduction

1.1. Electrochemical CO_2 Reduction

The atmospheric concentration of CO_2 has exceeded 424 ppm as of February 2024, far surpassing the 350 ppm safe threshold.[1] Excessive CO_2 emissions contribute to environmental crises such as global warming, extreme weather events, biodiversity loss, and ocean acidification. To mitigate these issues, significant efforts are required to achieve a carbon-neutral economy and limit global temperature rise to within 1.5 or 2 °C through international cooperation.[2] Carbon capture and utilization technologies show promise to achieve the net-zero carbon emission goal.[3] The direct air capture (DAC) method is known as one of the most effective approaches for removing CO_2 from the atmosphere.[4] CO_2 reduction reactions (CO_2RR) can convert the captured CO_2 from the atmosphere into valuable products. However, due to the inert nature of CO_2, these reactions require significant energy input. Electrochemical CO_2 reduction reactions (eCO_2RR) offer substantial potential to transform anthropogenic CO_2 emissions to high-value fuels and chemicals.[5] **Table 1** summarizes various reactions involved in producing different CO_2RR products, alongside the competing hydrogen evolution reaction (HER). The complex CO_2RR pathways lead to multiple products, each with distinct redox potentials, depending on the number of protons and electrons involved. Since the redox potential of HER is close to that of certain CO_2RR products, H_2 becomes a major competitive by-product during CO_2RR. This competition, combined with the variety of possible CO_2RR products, makes the selective production of a single product particularly challenging. eCO_2RR offers several advantages, such as adjustable operating parameters, mild reaction conditions, and scalability.[6] In a typical electricity-driven eCO_2RR setup, CO_2RR occurs at the cathode while the counter-oxidation reactions (e.g., oxygen evolution reaction, OER) take place at the anode. When coupled with renewable electricity (such as from solar and hydropower) and concentrated CO_2 from DAC, eCO_2RR provides a promising pathway to close the carbon loop in a sustainable manner.[7] The ultimate goal is to conduct CO_2RR economically, achieving high product selectivity, activity, and stability.

Z. Chen, S. Sun
Institut National de la Recherche Scientifique (INRS)
Centre Énergie Matériaux Télécommunications
Varennes, Québec J3×1P7, Canada
E-mail: shuhui.sun@inrs.ca

L. Zhang
Clean Energy Innovation (CEI) Research Center
National Research Council of Canada (NRC)
Vancouver, BC V6T 1W5, Canada
E-mail: Lei.Zhang@nrc-cnrc.gc.ca

G. Zhang
Department of Electrical Engineering
École de Technologie Supérieure (ÉTS)
Montréal, Québec H3C 1K3, Canada
E-mail: gaixia.zhang@etsmtl.ca

The ORCID identification number(s) for the author(s) of this article can be found under https://doi.org/10.1002/adma.202505287

DOI: 10.1002/adma.202505287

Table 1. Redox reactions for different CO_2RR products.[8]

CO_2RR Products	Reactions	*E* [V]
—	$CO_2 + e^- \rightarrow CO_2^{\cdot -}$	− 1.90
HCO_2H	$CO_2 + 2H^+ + 2e^- \rightarrow HCO_2H$	− 0.61
CO	$CO_2 + 2H^+ + 2e^- \rightarrow CO + H_2O$	− 0.53
HCHO	$CO_2 + 4H^+ + 4e^- \rightarrow HCHO + H_2O$	− 0.48
CH_3OH	$CO_2 + 6H^+ + 6e^- \rightarrow CH_3OH + H_2O$	− 0.38
CH_4	$CO_2 + 8H^+ + 8e^- \rightarrow CH_4 + 2H_2O$	− 0.24
C_2H_4	$2CO_2 + 12H^+ + 12e^- \rightarrow C_2H_4 + 4H_2O$	− 0.34
C_2H_5OH	$2CO_2 + 12H^+ + 12e^- \rightarrow C_2H_5OH + 3H_2O$	− 0.33
C	$CO_2 + 4H^+ + 4e^- \rightarrow C + 2H_2O$	− 0.20
—	$2H^+ + 2e^- \rightarrow H_2$	− 0.42

E is reported at a pH = 7 aqueous solution versus normal hydrogen electrode.

1.2. H_2 Production from Water Electrolysis

Anthropogenic activities, particularly fossil fuel consumption, significantly contribute to CO_2 emissions. Therefore, developing renewable and clean energy alternatives to fossil fuels is essential to accelerating the transition to a carbon-neutral economy. H_2, a clean energy carrier, is an ideal replacement for fossil fuels in applications such as fuel cell vehicles, which produce no CO_2 emissions.[9] Moreover, H_2 can play a critical role in decarbonizing difficult-to-abate sectors. However, the production of fossil fuel-derived H_2 (i.e., gray H_2, produced from natural gas reforming) should be phased out to avoid additional carbon emissions. Instead, green H_2, produced entirely from renewable energy sources, is pivotal to achieving the global net-zero emission targets.[10] For example, at least 74 green H_2-based projects, primarily in Europe, are currently underway or planned to decarbonize industrial operations in port areas.[11] Large-scale green H_2 production relies on efficient water electrolysis for HER.[12] In typical water electrolysis, the HER (0 V vs reversible hydrogen electrode, RHE) occurs at the cathode, reducing H^+ to H_2 while OER (1.23 V vs RHE) takes place at the anode, generating O_2. The relatively sluggish OER limits the overall efficiency of HER in water electrolysis. Besides, the high capital cost of water electrolyzer makes it less cost-effective than the more widely used method of steam methane reforming.[13] To enable the industrial-scale deployment of CO_2RR and HER, other than the catalytic properties of electrocatalysts, high-performing electrolyzers that operate at high current densities with excellent product selectivity are critical. The design of the electrochemical cell, particularly with respect to its kinetic properties, can significantly enhance overall performance.[14]

1.3. Current Advantages and Disadvantages of Cell Design for eCO_2RR and Water Electrolyzer

Currently, three main types of eCO_2RR cells (i.e., H-cell, flow cell, and membrane exchange assembly, MEA) are under active investigation. While H-cells are not practical for industrialization, flow cells and membrane electrode assemblies (MEAs) have their respective advantages and limitations. **Table 2** outlines the pros and cons of different eCO_2RR cell designs. For water electrolysis, alkaline water electrolysis (AWE) is a mature technology but offers fewer prospects for advancement compared to proton exchange membrane water electrolysis (PEMWE), anion exchange membrane water electrolysis (AEMWE), and solid oxide electrolysis cells (SOEC).

Each of these technologies has its own set of advantages and drawbacks, as shown in **Table 3**. Understanding the detailed mechanism in electrochemical devices is essential for the development of the next-generation electrochemical cell designs for CO_2RR and water electrolysis.

CO_2RR and HER, both catalytic reduction reactions, share many similarities. This review explores the recent advanced cell designs for CO_2RR and water electrolysis, alongside the state-of-the-art in situ cell designs for the operando characterizations to monitor the evolution of catalyst structures and chemical properties during the electrochemical reactions. These developments are illustrated in **Figure 1**, which highlights key components related to flow patterns, MEA designs, and electrolyte engineering. The review also emphasizes the role of rational counter-anodic reactions in improving the efficiency of both CO_2RR and HER. The integration of CO_2RR and HER electrolyzers with other electrochemical systems, such as fuel cells and battery technologies, is also considered, showcasing the potential for a future decarbonized industrial value chain. Finally, the review concludes with a summary, challenges, and perspectives on the system designs needed to scale CO_2RR and HER for industrial applications.

2. Rational System Design for eCO_2RR

2.1. Flow Cell System

In the early research stage, eCO_2RR can utilize H-cells that saturate CO_2 in the electrolyte media through bubbling with the submerged electrodes to screen the catalyst performance for fundamental studies.[8,17] However, limited by the dissolution and transport of CO_2, H-cells can only allow the current density at a low range (<50 mA cm^{-2}).[18] The low current density limit of H-cells fails the expectation of scale-up industrialization. Recent eCO_2RR studies commonly apply a flow cell system (**Figure 2a**, left) to evaluate the catalytic performance of CO_2RR, which is inspired by the successful fuel cell configurations that enhance

Table 2. Pros and cons of different eCO_2RR reaction cells.[15]

	Pros	Cons
H-cell	Easy to operate	Limited mass transfer
	Cathode and anode sides separation	High ohmic loss
	Quick primary studies	Low current density
	Inexpensive	Stability issue
		Not for industrialization
Flow cell	Gas diffusion electrode (GDE) application	Salt precipitation
	Improved mass transfer	Carbonate crossover
	Highly alkaline electrolytes	Electrolyte consumption
	Suppress competitive HER	High solution resistance
	High product selectivity	Electrode wetting
	High current density	Stability issue
	Modular design	
MEA	GDE application	Salt precipitation at high current densities
	Improved mass transfer	CO_2 crossover to the anode side
	Suppress competitive HER	Cation crossover from the anode side
	Catholyte free	Carbonate formation at the cathode side
	Reduced ohmic resistance	Product crossover
	Low cell potential	Flooding issue after long operation
	Controllable operating temperature	Complex membrane design
	Various membrane options	Stability issue
	High current density	
	High product selectivity	
	High energy efficiency (EE)	
	Modular design, easy to scale up	

the electrochemical activities.[19] A GDE (Figure 2a, right) is employed in the flow cell system where CO_2 is directly supplied to the catalyst layer. It avoids the dissolution of CO_2 in the electrolyte, allowing better mass transfer for CO_2RR in the flow cells than in the traditional H-cells. Hence, the flow cell system provides high current densities up to ampere level (industrially relevant level) in eCO_2RR.[20] Figure 2b depicts a typical flow cell stack for eCO_2RR. Normally, it contains a cathode current collector, a cathode GDE, an ion exchange membrane, a membrane holder, an insulator element, an anode catalyst, and an anode current collector. GDE-based flow cells offer higher catalytic activities than those of conventional H-cells but come with some drawbacks like salt precipitation, carbonate crossover, high solution resistance, and electrode wetting. Given the complex cell structure, one can work on many aspects to further improve the catalytic performance and potentially address the above-mentioned issues of flow cells for eCO_2RR.

2.1.1. *Optimize the Flow Pattern to Further Improve Mass Transfer*

The CO_2 gas supply is introduced through the gas pattern on the cathode side. In this case, the gas pattern in the flow cell stack affects the interaction of CO_2 with the GDE cathode. The proper design of the flow patterns and interface in the large-scale eCO_2RR reactor can achieve uniform flow distribution, realizing a high production rate. Based on this concept, Jung et al. employed a 3D computational fluid dynamics (CFD) model to investigate the performance of CO_2—CO in a large-scale (catalyst electrode area >50 cm^2) eCO_2RR electrolyzer with novel flow pattern designs.[21] CFD constructs a precise physical model by integrating continuity equations of momentum, mass, energy balances, and the transport of substances involved in the reaction. The authors introduced a unidirectional uniform distribution flow (UDF) pattern to improve the mass transfer of the eCO_2RR electrolyzer. Three different flow patterns were analyzed (Figure 2c–e), based on the pressure difference between two points (e.g., AB, CD, A′B′, C′D′, A″B″, C″D″, E″F″ in Figure 2d,e) from the Hagen–Poiseuille Equation (1).

$$\Delta P_{AB} = P_A - P_B = \frac{128\mu\left(\frac{Q_{tot}}{4}\right)}{\pi D_{eff}^4}\left(\pi R_{cell}\right) = \frac{32\mu Q_{tot}}{D_{eff}^4} R_{cell} \tag{1}$$

where μ is the dynamic viscosity ($Pa \cdot s$), Q_{tot} is the total volumetric flow rate of the feed gas ($m^3\ s^{-1}$), D_{eff} is the effective diameter of the flow channel (m), and R_{cell} is the radius of the cell (m). Combined with Darcy's law, the pressure difference between the two points becomes the driving force of the advection flow across the rib Equation (2).

$$q = -\frac{K}{\mu}\nabla P \tag{2}$$

Table 3. Advantages and disadvantages of different water electrolyzers.[16]

	Advantages	Disadvantages
AWE	Matured commercialization Cost-efficient Large-scale production	Corrosive liquid electrolyte Slow response time Low current densities Gas crossover Difficult to couple with renewable energies
PEMWE	Commercialized Modular cell design High H_2 purity High response time High operating pressure High current densities Coupling with renewable energies Higher EE	Noble metal-based catalysts High operation cost Corrosive environment
AEMWE	Less corrosive electrolyte Non-noble metal-based catalysts Modular cell design High H_2 purity High response time High operating pressure High current densities Coupling with renewable energies Higher EE	Early commercialization stage Membrane stability issue Inadequate durability
SOEC	Non-noble metal-based catalysts Modular cell design High H_2 purity High operating pressure High current densities High efficiency	Early commercialization stage High operation temperature Long start-up time Low durability

where q is the discharge per unit area (m s^{-1}), K is the permeability (m^2), μ is the dynamic viscosity (Pa · s), and ∇P is the pressure gradient (Pa m^{-1}). The higher pressure difference represents the higher convective flux in the porous GDE. The reference case flow pattern in Figure 2c is adapted from ref. [22] where the inefficiency arises due to the short flow length (πR_{cell}) and the low volumetric flow rate ($Q_{\text{tot}}/4$). The reference case flow pattern in Figure 2d is adapted from ref. [23] where a long trajectory increases the pressure difference with a single-channel gas feed, improving the convective mass transfer. The final ΔP_{AB} is eight times higher than that of $\Delta P_{\text{A}'\text{B}'}$. However, the two opposing vectors between A′ and B′ (flow toward the outlet) and C′ and D′ (flow toward the inlet) vanish in the permeable GDE, which reduces the advection. The UDF pattern in Figure 2e integrates flow segregation and unidirectional flow, directing the flow toward the outlet in every direction in the cell. The shorter flow length in the UDF pattern is compensated by the flow segregation, resulting in a higher $\Delta P_{\text{E}''\text{F}''}$ than that of $\Delta P_{\text{A}'\text{B}'}$. Figure 2f–h depicts the velocities in the GDE of different flow patterns. The black arrows indicate the flow direction in the GDE. The separate paths pattern (as in Figure 2c) demonstrates poor performance due to the low ΔP (Figure 2f). The single path with flow retrace pattern (as in Figure 2d) demonstrates higher velocity than that of the separate paths pattern (Figure 2g), but requires additional compression power to supply the feed gas, increasing the operational cost. The UDF pattern (as in Figure 2e) utilizes a one-path flow to guide all flow components directing from inlet to outlet. It improves the convective mass transfer while retaining the flow uniformity (Figure 2h). The reference case flow patterns demonstrate the best CO_2—CO performance at 1 м $KHCO_3$. As illustrated in Figure 2i, the UDF design contributes to an ≈28% increase in the CO partial current density in the 1 м $KHCO_3$ electrolyte and a 60% increase in the 1 м KOH electrolyte. It reveals that the convective mass transfer favors the CO production rate, which highlights the significance of the flow pattern design in the eCO_2RR electrolyzer.

2.1.2. Acidic Electrolytes to Address Salt Precipitation

To suppress the competing reaction HER during CO_2RR, alkaline electrolytes are usually employed. In alkaline electrolytes, HER has slow kinetics of the Volmer step (first water reduction step) that lowers the surface coverage of adsorbed hydrogen, thus affecting the subsequent Heyrovsky and Tafel steps.[26] During the eCO_2RR process, the pH of the near catalyst sur-

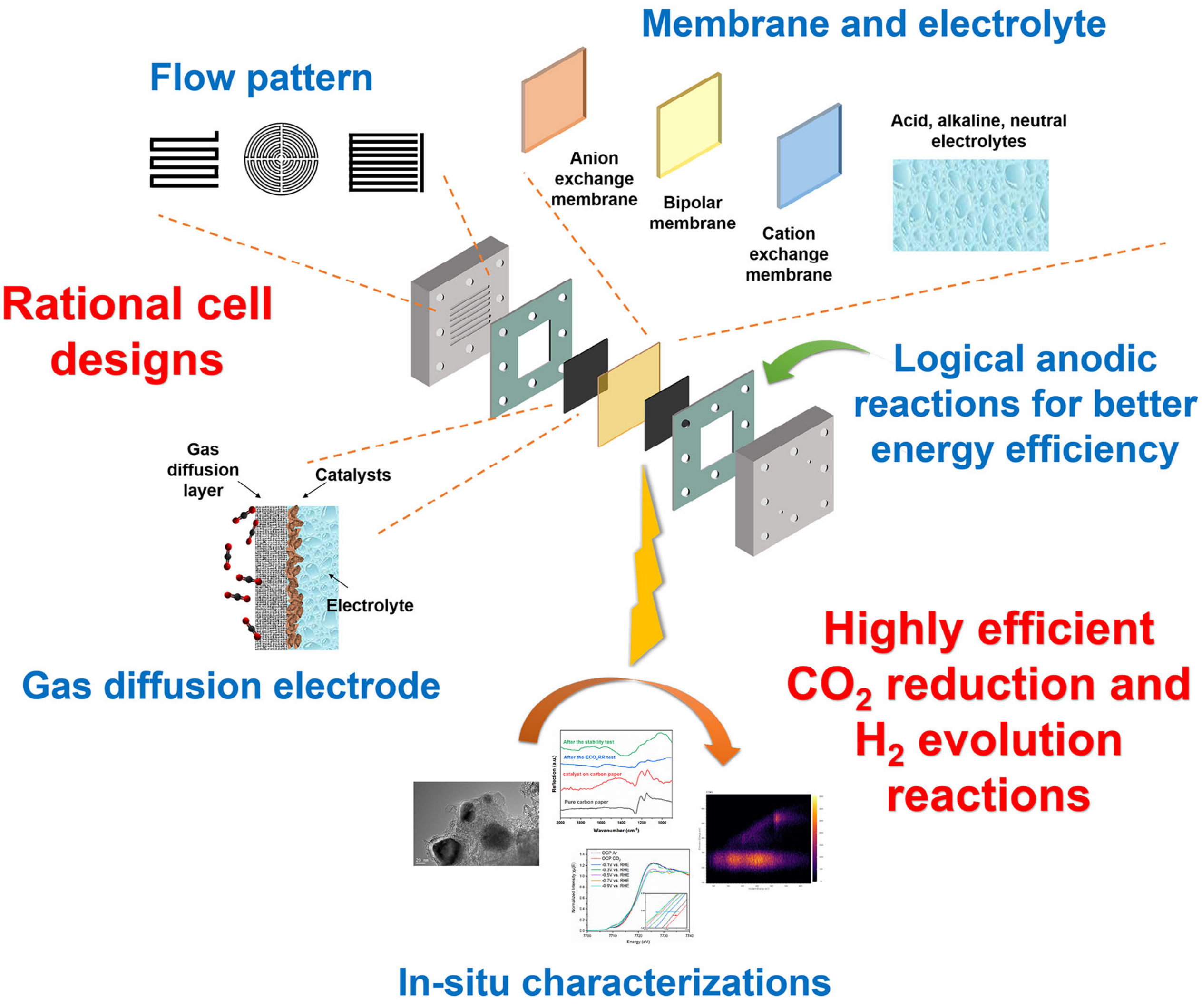

Figure 1. Overall illustration of rational system designs for highly efficient CO_2RR and HER.

face region increases as the proton donor is consumed. It contributes to suppressing the competing HER.[27] However, in a strong basic environment, CO_2 tends to convert to carbonates Equation (3) or bicarbonates Equation (4), causing the flooding issue.[28]

$$CO_2 + 2OH^- = CO_3^{2-} + H_2O \tag{3}$$

$$CO_2 + OH^- = HCO_3^- \tag{4}$$

It also decreases the single pass carbon efficiency (SPCE; the carbon fraction in CO_2 supply that is transformed to the reduction products) in CO_2RR. To address the carbonation accumulation, other than constantly interrupting the reaction to remove the (bi)carbonates and to refresh the GDE,[29] here are some promising directions.

The Cation Strategy and Operando Activation in Acid and Neutral Media: One of the quickest approaches to suppress the carbonation during eCO_2RR is to avoid the alkaline environment. However, by switching the electrolyte from the strong basic environment to neutral or acidic environments, it risks losing the high CO_2RR activity under alkaline media.[30] Many works report that it is the alkali metal cation effect that helps the activation of CO_2 and the stabilization of the key CO_2RR intermediates.[31] Zhang et al. used the simulation of ab initio molecular dynamics to investigate the effect of alkali metal cations (from Li^+ to Cs^+) on the CO_2RR initiation on the Cu surface.[32] **Figure 3a** depicts the $^*CO_2$ chemisorbed final state (FS) configurations with different alkali metal cations in the $Cu{-}^*CO_2{-}H_2O$ system. Na^+ and Li^+ coordinate with only one O atom of $^*CO_2$ by side configuration. K^+ and Cs^+ coordinate with both O atoms of $^*CO_2$ by a bridge configuration. This is due to the radius differences between the cations. By using the CO_2 absorption energy to probe the activity, Li^+ has the strongest $^*CO_2$ adsorption (Figure 3c). In the meantime, the free energies of Na^+, K^+, and Cs^+ are very close to each other. The CO_2 activation free energy profile from the initial state (IS) to the transition state (TS) to FS without metal cations is shown in Figure 3b,c to indicate a reference 0.22 eV kinetic barrier in the $Cu{-}^*CO_2{-}H_2O$ system. The free energy profiles of Li^+ (0.17 eV), Na^+ (0.16 eV), K^+ (0.12 eV), and Cs^+ (0.10 eV) are

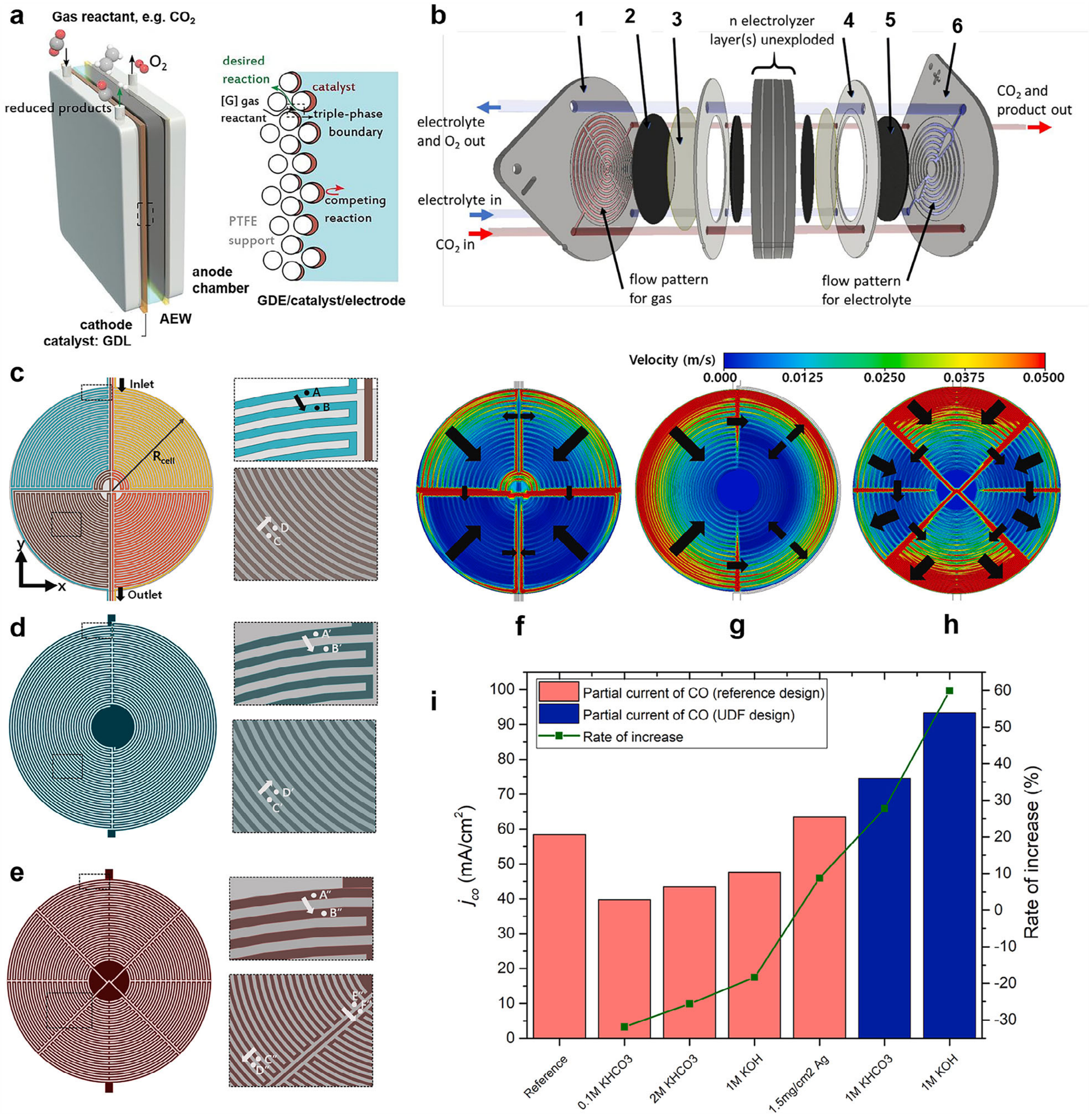

Figure 2. a) Left: a typical flow-cell illustration with reactant gases feeding through the back of a GDE catalyst, aqueous electrolyte, anion-exchange membrane (AEM), and gas-diffusion layer (GDL). Right: detailed illustration of the tri-phase boundary in a GDE. Reproduced with permission.[24] Copyright 2020, The American Association for the Advancement of Science. b) The schematic of the eCO_2RR electrolyzer cell stack. 1: the current collector for the cathode; 2: the cathode GDE; 3: the ion exchange membrane; 4: the membrane holder and the insulator element; 5: the anode catalyst; 6: the current collector for the anode. Reproduced with permission from.[25] Copyright 2019 American Chemical Society. Designs of flow pattern channel of eCO_2RR electrolyzer: c) the separate paths, d) the single path with flow retrace, and (e) the unidirectional uniform distribution flow with channel segregation. Velocity contour for geometries of f) the separate paths, g) the single-path with flow retrace, and (h) the unidirectional flow with segregation. i) Experimental results of 1 mg cm^{-2} Ag catalyst loading in flow pattern effect, interface, and pH to mass transfer on eCO_2RR with a flow rate of 400 SCCM, under a cell voltage of 3 V in 1 м $KHCO_3$. Reproduced with permission from.[21] Copyright 2021 Published by Elsevier B.V.

displayed in Figure 3c. The energy barriers gradually decrease from Li^+ to Cs^+. Besides, the free energy barrier difference between the two groups of Li^+/Na^+ and K^+/Cs^+ is 0.05 eV, which corresponds to the increased reaction rate by a factor of five, agreeing with the experimental performance results. Figure 3d shows the coordination numbers in the first solvation shell of metal cations with and without $^*CO_2$ at TS. For the Li^+/Na^+ group, the coordination with CO_2 in the first solvation shell involves an oxygen atom exchange from H_2O, which leads to an almost unchanged total coordination number. For Cs^+ and K^+,

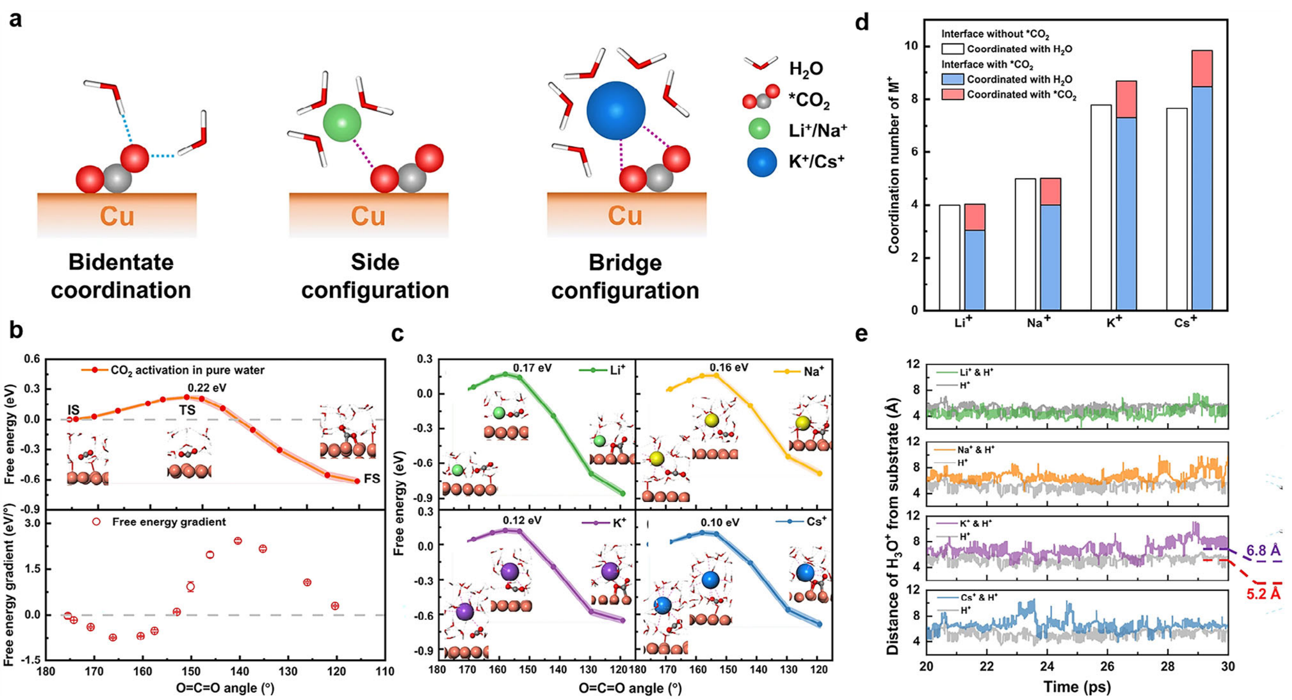

Figure 3. a) The interactions between cations, $*CO_2$, and H_2O at Cu(100) surface in the Cu—$^*CO_2$—H_2O system. Left: the $*CO_2$ bidentate adsorption at Cu surface with one O atom and C coordinating with Cu while the other O atom bonding with the hydrogen of H_2O (blue dashed lines). Middle: the Na^+ or Li^+ side configuration, coordinating with one O atom of $*CO_2$ (red dashed line). Right: The Cs^+ or K^+ bridge configuration, coordinating with both O atoms of $*CO_2$. b) Top: The free energy profile with IS, TS, and FS structures for the CO_2 adsorption in the Cu—$*CO_2$—H_2O system without metal cations. The zero value is indicated by the gray dashed lines. Bottom: The corresponding free energy gradient at each calculated collective variable in the top Figure, with an error bar. The positions of FS, IS, and TS are indicated by the crossover points with a dashed line. c) The IS, TS, and FS free energy profiles and representative structures in the Cu—$*CO_2$—M^+ system of the top left: Li^+, top right: Na^+, bottom left: K^+, and bottom right: Cs^+. In the local structures, H_2O is illustrated as white and red sticks, Cu is illustrated as reddish-brown spheres, CO_2 is illustrated as red and gray spheres, and the cations of Cs^+, K^+, Li^+, and Na^+ are represented by blue, green, purple, and yellow spheres, respectively. The cation coordination with O atoms in the first solvation shells is illustrated by magenta dashed lines. d) The number of coordinated O for Cs^+, Li^+, K^+, and Na^+ cations at the interface of Cu(100)–electrolyte without and with $*CO_2$. e) The H_3O^+ distribution in the solvent without and with alkali metal cations. The excess proton from the Cu substrate in the 10 ps production timescale without and with the K^+ cation is represented by the purple and red dashed lines, respectively. Reproduced with permission from[32] under the terms of the Creative Commons CC BY license.

the coordination number increases by 2.2 and 0.9, respectively. The better coordination structure of Cs^+ and K^+ than that of Na^+ and Li^+ is attributed to the large cation radius that can coordinate with the oxygen atoms from both CO_2 and H_2O, facilitating the electron transfer to activate CO_2. Figure 3e demonstrates the excess proton–interface distance distribution. For the case of Li^+, the proton–interface distance is even smaller than that of a single H_3O^+ due to the small solvation shell of Li^+. It allows H_3O^+ to coexist with the solvated Li^+. For the cases of Na^+, Cs^+, and K^+, the excess proton is confined in the first solvation shells and repelled away from the second water layer. H^+ is constrained and repelled from the interface because of the presence of large metal cations, suppressing the competing HER. With all these analyses, the necessity of alkali metal cations in CO_2RR for CO_2 activation and the HER prohibition is profoundly explained. In addition, it is found that the periodic addition of acids (e.g., HCl) to the neutral catholyte (e.g., KCl) during the eCO_2RR process can effectively alleviate the carbonation effect.[33]

Combining both the concepts of the cation effect and the periodic addition, Endrődi et al. developed an operando regeneration and activation process on a zero-gap electrolyzer cell periodically infused with alkali metal cation-containing solutions in the cathode side to enable the DI water-feed electrolyzers to function with the CO_2RR catalytic performance equivalent to those utilizing alkaline electrolytes.[34] **Figure 4a,b** shows the scanning electron microscopy–energy-dispersive X-ray analysis (SEM–EDX) image and the microtomography image of the cross-section of the GDE after CO_2 electrolysis in the 1 м KOH anolyte, respectively. It reveals the severe precipitation of $KHCO_3$ on the GDE during eCO_2RR in the alkaline electrolyte due to the unintended crossover of the alkali metal cations through the anion exchange membrane (AEM) from the anode side. To avoid this metal cation cross-over issue, the authors utilized pure water as anolyte, along with an electrolyte (0.5 м KOH) injection method to create the alkali metal cation-infused GDE in the cathode as demonstrated in Figure 4c. During the periodical electrolyte infusion, the CO_2 gas feed pushes the electrolyte through the cell. The precipitate can only be generated at a limited contact area between the solution and the gas, resulting in a constant presence of the activating alkali metal cations but avoiding accumulation at the cathode GDE. Besides, each new infusion of the electrolyte dissolves the precipitates generated from the last infusion. This periodic electrolyte infusion approach not only introduces alkali metal

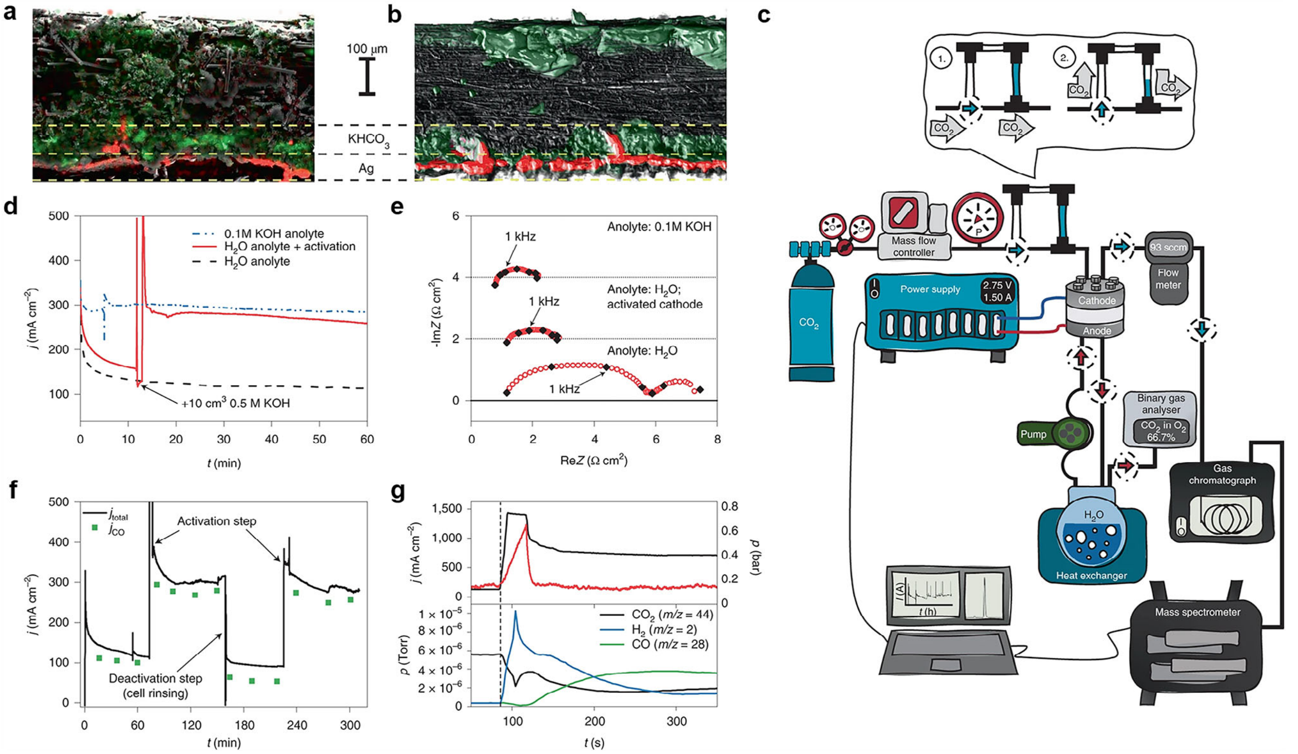

Figure 4. The cross-section images of a) SEM–EDX and b) microtomography images of a GDE in a zero-gap cell after continuous CO_2 electrolysis in 1 M KOH anolyte at 3.0 V and 50 °C. The green and red colors in the microtomography and SEM–EDX images indicate K and Ag atoms, respectively. c) The schematic diagram of the instrumentation and piping framework is applied. d) The chronoamperometric curves and e) the electrochemical impedance spectroscopy before and after the cathode GDE activation with 10 cm^3 of 0.5 M KOH solution in a 3:1 water/isopropanol mixture at 3.1 V and 60 °C with a CO_2 feed rate of 12.5 cm^3 cm^{-2} min^{-1}. f) The CO current density is measured under the same conditions as in (d). The cathode GDE was deactivated by rinsing with 10 cm^3 of a 3:1 water/isopropanol mixture. g) The time-resolved top: current density and CO_2 inlet pressure and bottom: product stream composition change during the periodical infusion in the electrolyzer with 3 cm^3 of 1 M CsOH solution in a 3:1 water/isopropanol mixture at 3.2 V and 60 °C with a CO_2 feed rate of 12.5 cm^3 cm^{-2} min^{-1}. Reproduced with permission from.[34] Copyright 2021, B. Endrődi et al., under exclusive license to Springer Nature Limited.

cations to the GDE but also removes the generated precipitates in the GDE. Activating the cathode GDE by the proposed electrolyte infusion method provides the current in the pure water-fed electrolyzer to a level equivalent to that of a 0.1 M KOH-fed electrolyzer (Figure 4d). In addition, the charge transfer resistance of the pure water-fed electrolyzer decreases to a similar value to that of the alkaline electrolyte-fed electrolyzer with the periodical infusion approach (Figure 4e). Figure 4f demonstrates that the activation provided by this electrolyte infusion is reversible. By injecting the solution without alkali metal cations, the cell activity decreases to the original level, which indicates the importance of the cathode interface role in the CO_2RR electrolyzer. The monitoring of time pressure in Figure 4g also shows that the activation takes about 50 s for the injected electrolyte to leave the electrolyzer and gradually stabilizes after around 120 s. With this periodical infusion approach, the pure water-fed CO_2RR electrolyzer was able to run for over 200 h at a current density of around 420 mA cm^{-2}. Notably, for this electrolyte infusion approach, the solvent mixture of the electrolyte must be optimized to properly wet the GDE for the infusion to happen.

Creating the Local Alkaline Environment in Acid Media: Other than the neutral media, the acid media are also widely studied to overcome the precipitation issues in the alkaline media while improving the SPCE. In acid media, H_3O^+ provides the proton for CO_2RR rather than H_2O in alkaline media. Thus, no CO_2 is consumed with OH^- to form (bi)carbonates in the acidic electrolyte. However, with the acidic environment, HER becomes dominant during the electrolysis.[35] How to prohibit the competing HER during eCO_2RR is the top priority for the acid media cases. Intriguingly, when the reaction happens at a large current density (e.g., >1 A cm^{-2}), a local proton-depletion microenvironment (high pH condition) can be created where the locally generated OH^- surpasses the proton influx from the acid electrolyte.[36] By adopting this strategy, Chi et al. fabricated a GDE with Bi nanosheets to confine the in situ formed OH^-, creating a local alkaline environment at a moderate current density (≈200–500 mA cm^{-2}) to promote eCO_2RR in acid media.[37] The authors vertically grew sheet-shaped Bi catalyst on GDL to form a GDE that constructs electrolyte reservoirs, preventing the diffusion of the outward OH^- and the inward proton. **Figure 5a** depicts the proton transport of the conventional particulate catalyst environment in acid media, where the proton around the catalyst layer is rapidly replenished, resulting in a proton-rich local environment. Figure 5b depicts the proton transport of the electrolyte reservoir situation. Under these circumstances,

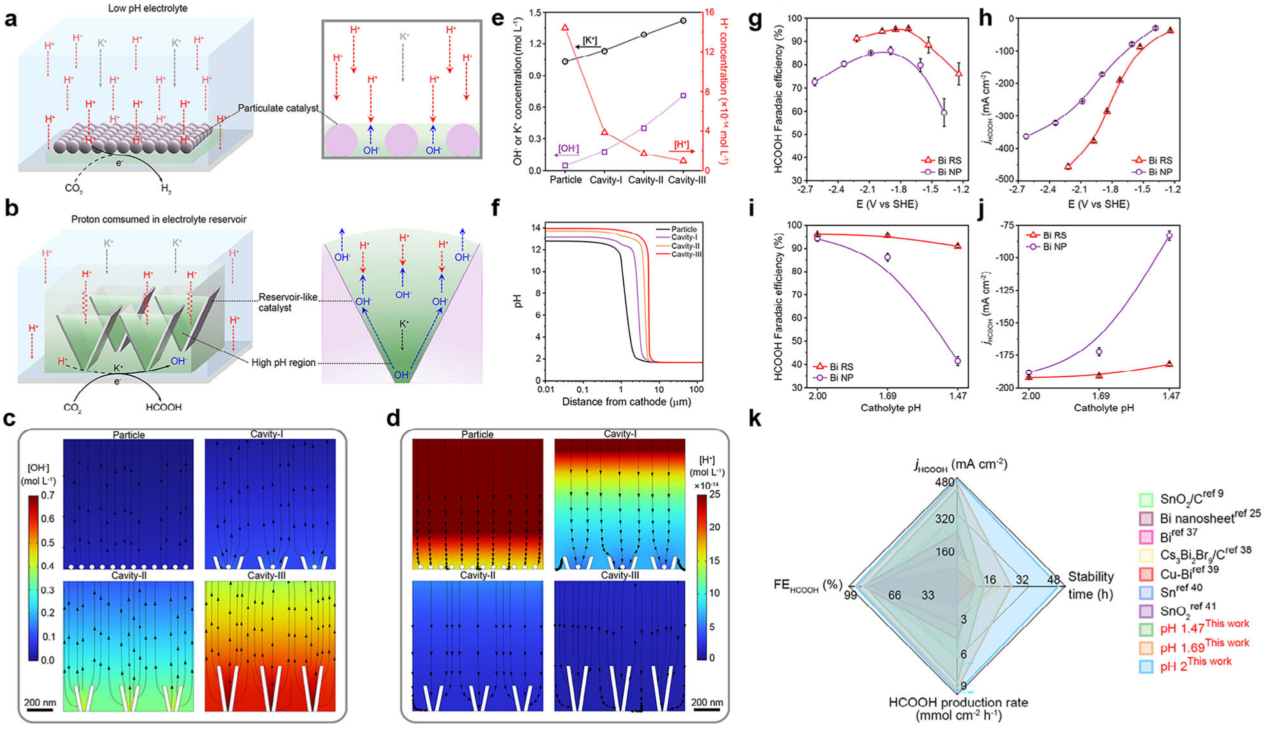

Figure 5. The schematics of the proton transport in the near catalyst layer of (a) conventional particulate and (b) sheet-shaped reservoir catalysts. c) The OH^- concentration profiles of conventional particulate catalysts and different sheet-shaped reservoir models. d) The H^+ concentration profiles of conventional particulate catalysts and different sheet-shaped reservoir models. Arrows imply the species migration direction, scale bars: 200 nm. e) The local K^+ and OH^- concentrations of conventional particulate catalyst and different sheet-shaped reservoir models. f) The pH distribution of conventional particulate catalyst and different sheet-shaped reservoir models. The simulations were performed at −1.7 V vs standard hydrogen electrode (SHE) with a bulk pH value of 1.69. g) The potential-dependent HCOOH FE of Bi nanoparticle (NP) and the Bi reservoir structure (RS) and (h) the HCOOH current density on Bi NP and Bi RS in the electrolyte of 0.5 M K_2SO_4 with 0.1 M H_2SO_4 (pH 1.69). i) The HCOOH FE and (j) the HCOOH partial current density of Bi RS and Bi NP catalysts at 200 mA cm^{-2} in different pH acidic electrolytes. k) The comparison of HCOOH operating lifetime, current density, FE, and production rate on different catalysts reported in acidic CO_2RR. Reproduced with permission from[37] under the terms of Creative Commons Attribution-NonCommercial-NoDerivatives License 4.0 (CC BY-NC-ND).

K^+ and the in situ-generated OH^- are constrained (Figure 5e), which provides local high pH regions (Figure 5f). Figure 5c,d demonstrates the computed OH^- and H^+ concentration distribution on different sheet-shaped models. The model of cavity-III acts as the best OH^- reservoir. The experimental results accord with the computed simulations. The electrolyte reservoir design adapts well to the acidic electrolyte, even in extremely low pH environments (Figure 5i,j). This sheet-shaped Bi GDE allows the HCOOH faradaic efficiency (FE) of 96.3% with a HCOOH production current density of 471 mA cm^{-2}, a 79% SPCE, and a stability over 45 h (Figure 5g,h,k). Other than the benefits of avoiding the flooding effect and increasing the SPCE, acid media are also proven to suppress the oxygen reduction reaction, which makes CO_2RR favorable when using flue gas.[38]

In short, the electrolytes applied in eCO_2RR are usually alkaline, acid, and neutral media. Generally, alkaline media are employed to suppress the competing HER and accelerate CO_2RR but raise the issues of carbonation and flooding. Acid and neutral media applications alleviate the carbonation issue but promote HER rather than CO_2RR during catalysis. To increase the CO_2 activation for CO_2RR in acid and neutral media, the introduction of alkaline metal cations in the electrolytes proves to be promising. To suppress HER in acid and neutral media, creating a local alkaline environment is important. It can be achieved by different approaches, such as the periodic injection of a small amount of alkaline electrolytes near the GDE cathode and the cathode catalyst structure engineering. To suppress the competing HER in the neutral and acid media, another way is to replace the liquid catholyte solution with the solid polymer electrolyte.

2.2. Electrode and MEA Engineering

The catholyte-free MEA, also known as a zero-gap electrolyzer, features a sandwich structure where a polymer electrolyte membrane is tightly sandwiched between the anode and the cathode, with the liquid anolyte circulating through the porous anode.[39] MEAs consist of various components, such as the ionomer membrane, catalyst layer, and gas diffusion layer, which are similar to those used in flow cells. As a result, MEAs inherit the advantages of flow cells, including ionomer membranes for ion transport and product separation and GDE for improved mass transfer and water management. The zero-gap design enables the direct contact of GDE and the membrane, minimizing resistance and facilitating the achievement of industrially relevant current densities. Additionally, the reduced ohmic loss contributes to lower

Table 4. Quantitative comparisons of Fe—N—C catalysts in H-cell, flow cell, and MEA for eCO_2RR.

Catalysts	Cell type	FE_{CO}	Current densities	Stability	Refs.
FeN_4	H-cell	>90%	$Jco = -25$ mA cm^{-2} at −0.8 V versus RHE	10 h at −0.5 V versus RHE ≈−5 mA cm^{-2}	[18d]
Fe^{3+}—N—C	H-cell	>90%	$Jco = -20$ mA cm^{-2} at −0.47 V versus RHE	>12 h at −0.37 V versus RHE ≈−8 mA cm^{-2}	[40]
	Flow cell	>90%	$Jco = -94$ mA cm^{-2} at −0.45 V versus RHE	>28 h at −0.41 V versus RHE ≈−50 mA cm^{-2}	
Fe/Se—N—C	H-cell	>90%	$Jco = -6.5$ mA cm^{-2} at −0.55 V versus RHE	24 h at −0.45 V versus RHE ≈−7 mA cm^{-2}	[41]
	Flow cell	>90%	$Jco \approx -100$ mA cm^{-2} at −0.7 V versus RHE	12 h at −0.7 V versus RHE with <−100 mA cm^{-2}	
	MEA	>99%	$Jco = -250$ mA cm^{-2} at a cell voltage of 4 V	12 h at a cell voltage of ≈2.5 V at −100 mA cm^{-2}	

cell voltage, making MEAs more attractive for industrial applications requiring high EE. This unique architecture also addresses common challenges in flow cells, such as salt precipitation and electrode wetting during eCO_2RR.

Table 4 presents a brief quantitative comparison, including current densities, Faradaic efficiencies, and long-term stability of Fe—N—C catalysts in H-cell, flow cell, and MEA in eCO_2RR, highlighting the improvements that MEA provides to achieve industrially relevant current densities.

Yin et al. constructed a stable and conductive quaternary ammonia poly (*N*-methyl-piperidine-*co*-*p*-terphenyl) (QAPPT) as the alkaline polymer electrolyte membrane (APEM) to achieve the industrial-scale eCO_2RR activities with pure water.[42] **Figure 6a** depicts the cell structure of the APEM CO_2RR electrolyzer. The cathodic catalyst (Au/C) is impregnated with QAPPT and sprayed on the QAPPT APEM (Figure 6b). During eCO_2RR, the charge carrier in the APEM gradually transforms from OH^- to HCO_3^-/CO_3^{2-} because of the carbonation issue. In this case, the percentage of OH^- in the APEM depends on the ratio of the CO_2 flow rate and the CO_2 consumption rate (CO_2 stoichiometry) on the cathode. The CO_2 stoichiometry can be estimated by monitoring the CO_2 crossover on the anode side, as illustrated in Figure 6c. The shadow region in Figure 6c shows the realistic OH^- percentage. When the CO_2 flow rate is ten times the rate of CO_2RR, the OH^- percentage is around 80%. Under experimental conditions, the real CO_2 stoichiometry on the cathode is <10, revealing the minor carbonation and CO_2 cross-over effects that could jeopardize the long-term operation. OH^- is still the

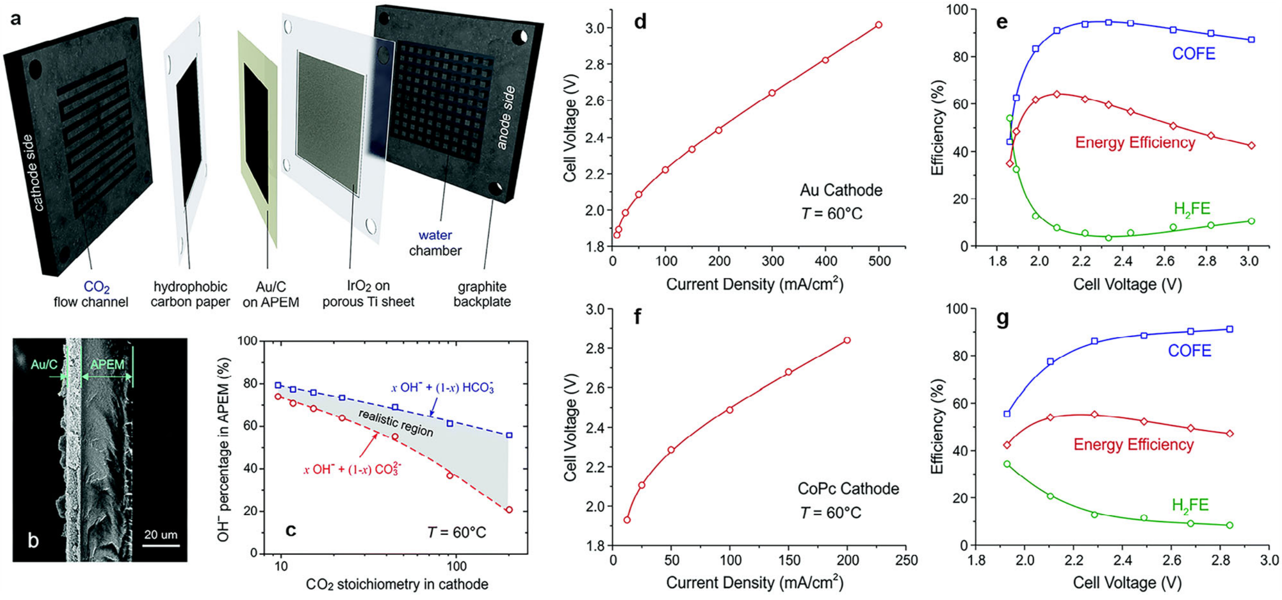

Figure 6. a) The schematic of the APEM CO_2RR electrolyzer with pure water supplied in the anode and dry CO_2 supplied in the cathode. b) The SEM cross-section image of the Au/C cathode catalyst APEM. c) The percentage of OH^- in APEM as a function of the CO_2 stoichiometry on the cathode, calculated based on the amount of CO_2 cross-over from cathode to anode, measured by gas chromatography (GC). The red dashed line represents the upper limit of $CO_3{}^{2-}/OH^-$. The blue dashed line represents the upper limit of $HCO_3{}^-/OH^-$. The CO_2 stoichiometry changes with the current densities while the CO_2 flow rate is kept at 100 SCCM. d) The *I*–*V* curves, e) FE_{CO} (denoted as COFE) and EE of Au, f) the *I*–*V* curves, and (g) FE_{CO} and EE of CoPc in the APEM CO_2RR electrolyzer. Reproduced with permission from.[42] Copyright 2019, RSC Publishing.

major charge carrier in this APEM CO_2RR electrolyzer, providing a strongly alkaline environment on the cathode for CO_2RR. The as-constructed APEM CO_2RR electrolyzer allows a 500 mA cm^{-2} at a cell voltage of 3 V at 60 °C and is stable at a cell voltage of 2.25 V over 100 h while providing high EE and maintaining the FE_{CO} at a range of 90–95% (Figure 6d–g). Note that the development of APEM is quite recent. The commercialization awaits the successful fabrication of the highly stable and conductive APEM. Hence, there is still a lot to explore in the aspect of APEM.

2.2.1. Gas Diffusion Electrode Catalyst Engineering for Enhanced Catalytic Performance

The catalyst is always the key to catalytic reactions. Herein, the GDE (GDL + catalyst layer), where the active catalysts are attached, determines the final activity of the electrolyzer. Modifying either the GDL part or the catalyst part in GDE shows the potential to augment the CO_2RR performance. For example, Vichou et al. immobilized a layer of ionic liquids (ILs) on a glassy carbon to benefit from the high selectivity of ILs for molecular complex catalysts in acid-aqueous media CO_2RR. The imidazolium cation organic layer immobilized on the electrode–electrolyte interface creates a local electric field, positively charging the electrode surface, suppressing the HER, and favoring CO_2RR to formate.[43] Sun et al. constructed a GDE with the ultrathin superhydrophobic macropore structure to promote CO_2 diffusion in acid media.[44] **Figure** 7a depicts the schematic structure of this all-metal Cu-GDE with the enhanced gas diffusion ability, prepared by the in situ electrooxidation of the porous Cu foil. The thin hydrophobic Cu nanoneedles with a large pore diameter, coated with a water-barrier of 1-octadecanethiol on the porous Cu surface, result in the high CO_2 concentration on the catalyst–electrolyte interface. SEM images of Figure 7b–d confirm that the GDE is a macroporous Cu foil densely covered with nanoneedles with a thickness of ≈100 µm. EDX images in Figure 7e reveal the uniformly distributed S from alkanethiol on the Cu nanoneedle surfaces. The coating layer of 1-octadecanethiol is also visible on the nanoneedles (Figure 7f). The prepared Cu-GDE is extremely hydrophobic and mechanically flexible (Figure 7g). High FE for C_{2+} can be achieved at both pH = 1 and pH = 6 electrolytes (Figure 7h). By changing the electrooxidation time of the porous Cu foil, the amount of Cu nanoneedles varies, leading to different roughness factors (rf) that reflect the number of active sites for CO_2RR. Figure 7i shows that the formation rate (FR) of C_{2+} is in a linear correlation with rf at pH = 6, while FR_{C2+} is in a linear correlation with rf^2 at pH = 1. It is because CO_2RR at pH = 6 is determined by the number of active sites on the catalyst (first-order reaction) while CO_2RR at pH = 1 is determined by the amount of OH^- and the active sites on the catalyst (second-order reaction). The nanoneedle structure enables a local alkaline environment with a pH of ≈10.9, which can suppress the local H^+ concentration (Figure 7j). The conversion efficiency of C_{2+} and SPCE increases with the decrease of the CO_2 flow rate (Figure 7k). Further, the CO product selectivity decreases with the decrease of the CO_2 flow rate (Figure 7l) while the C_{2+} product selectivity increases with the decrease of the CO_2 flow rate (Figure 7m). It suggests that with this nanoneedle-shaped Cu-GDE, a slow CO_2 flow can achieve a high secondary CO utilization for C_{2+} production (Figure 7n) in the acid electrolytes.

Apart from the optimization of cathode catalyst designs, the catalyst mass loading, binders applied when fabricating the GDE, etc., are also pivotal for CO_2 electrolysis, which affects the performance and stability of the cell. For example, the mass loading of the catalyst affects the number of active sites and the thickness of the GDE. They will reflect on the catalytic performance and the wettability (fast flooding when the catalyst layer is too thin) of GDE during eCO_2RR.[45] The polymer binders are inevitably used to combine powder electrocatalysts with the substrate. However, the binders (e.g., Nafion and polytetrafluoroethylene, PTFE) will block the active sites, inhibit diffusion, and increase the series resistance, which weakens the catalytic performance.[46] The different binder materials can also affect the wettability of the GDE and the product selectivity of CO_2RR.[47] The amounts of the catalyst powder and binders in the ink need to be optimized. To address this concern, it would be best to optimize the GDE fabrication parameters (e.g., mass loading, binder materials, fabrication techniques) for different catalysts to obtain the highest catalytic performance of the catalyst.[48]

2.2.2. Membrane Electrode Assembly Engineering

Anion Exchange Membrane, Cation Exchange Membrane, and Bipolar Membrane: In conventional flow cells, both the cathode and anode sides require electrolyte liquid flows. It raises the worries of corrosion on the cell and the total operation cost. Inspired by the H_2 fuel cell design,[19e,49] MEA cell designs are free from or reduce the solution supplies. Consequently, the cell assembly and the operation and maintenance will all be simplified (e.g., the APEM cell design presented above in this review). In MEA, the commonly applied Nafion membrane is a proton exchange membrane (PEM), which favors HER during CO_2RR.[20a,50] To find a proper membrane designated to CO_2RR is important for the CO_2RR MEA electrolyzer design. Some of the examples in the previous sections are already using the MEA cell structure. Advanced cell designs with the AEM and the cation exchange membrane (CEM) show superior CO_2RR catalytic performance under different conditions. Xia et al. designed a solid-state electrolyte (SSE) MEA cell where pure HCOOH can be produced without the participation of impurity ions.[51] As demonstrated in **Figure** 8a, the Bi-based cathode GDE and the IrO_2/C anode GDE are separated by AEM and CEM, respectively. A porous H^+ or $HCOO^-$-conductor SSE is sandwiched between the AEM and CEM. Humidified CO_2 is supplied on the cathode to be reduced to negatively charged $HCOO^-$ while 0.5 M H_2SO_4 is circulated in the anode side for water oxidation and to produce H^+. Driven by the electric field, $HCOO^-$ and H^+ travel through AEM and CEM, respectively, to combine in SSE to generate HCOOH. Depending on the type of SSE (H^+ conductor or $HCOO^-$ conductor), the final HCOOH product is generated at either the right ($HCOO^-$ conductor) or left (H^+ conductor) interface between SSE and the membranes. A deionized water stream flows through the SSE, producing pure HCOOH solutions with different concentrations based on the different flow rates. The authors further improved this SSE MEA design for more economically appealing applications. Figure 8b depicts a four-chamber symmetric MEA

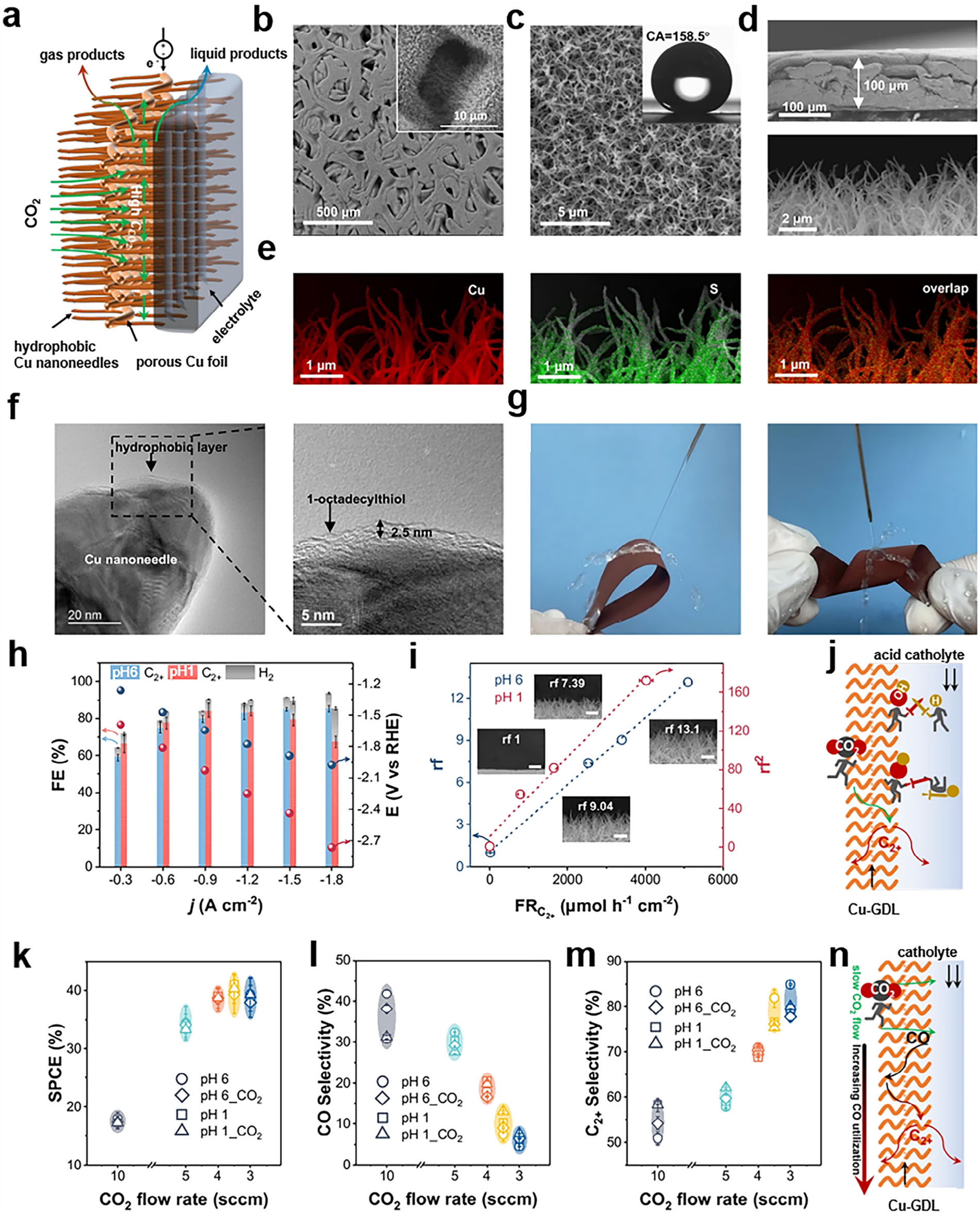

Figure 7. a) The schematic illustration of the nanoneedle-shaped Cu-GDL in CO_2RR. The SEM images of b) the macropore structure (inset: the channel of the macroporous) and (c) Cu nanoneedles with a large contact angle. d) The SEM cross-section images of the Cu-GDE. e) The EDX mapping of the Cu and S elemental distribution in the Cu-GDE. Red: Cu; green: S. f) The TEM images of one 1-octadecylthiol single layer (≈2.5 nm) on the Cu nanoneedle. g) The twisting and bending flexibility tests. h) The C_{2+} and H_2 FEs, and potential (E vs RHE, right) as functions of current density. i) rf² (right) and rf (left) as functions of FE_{C2+}. Inset: SEM images of Cu-GDL with different rf (error bars = 2 μm). j) The function of OH^- on Cu-GDL during CO_2RR in acid media. k) The SPCE, l) CO product selectivity, and (m) C_{2+} product selectivity as a function of the CO_2 flow rate at −0.5 A cm⁻² in pH = 6, pH = 1, and CO_2-saturated pH = 3.8 (pH 6_CO_2) and pH = 0.9 (pH 1_CO_2) electrolytes. n) The secondary CO conversion in CO_2RR at a slow CO_2 flow rate. Reproduced with permission from[44] under the terms of the Creative Commons CC BY license.

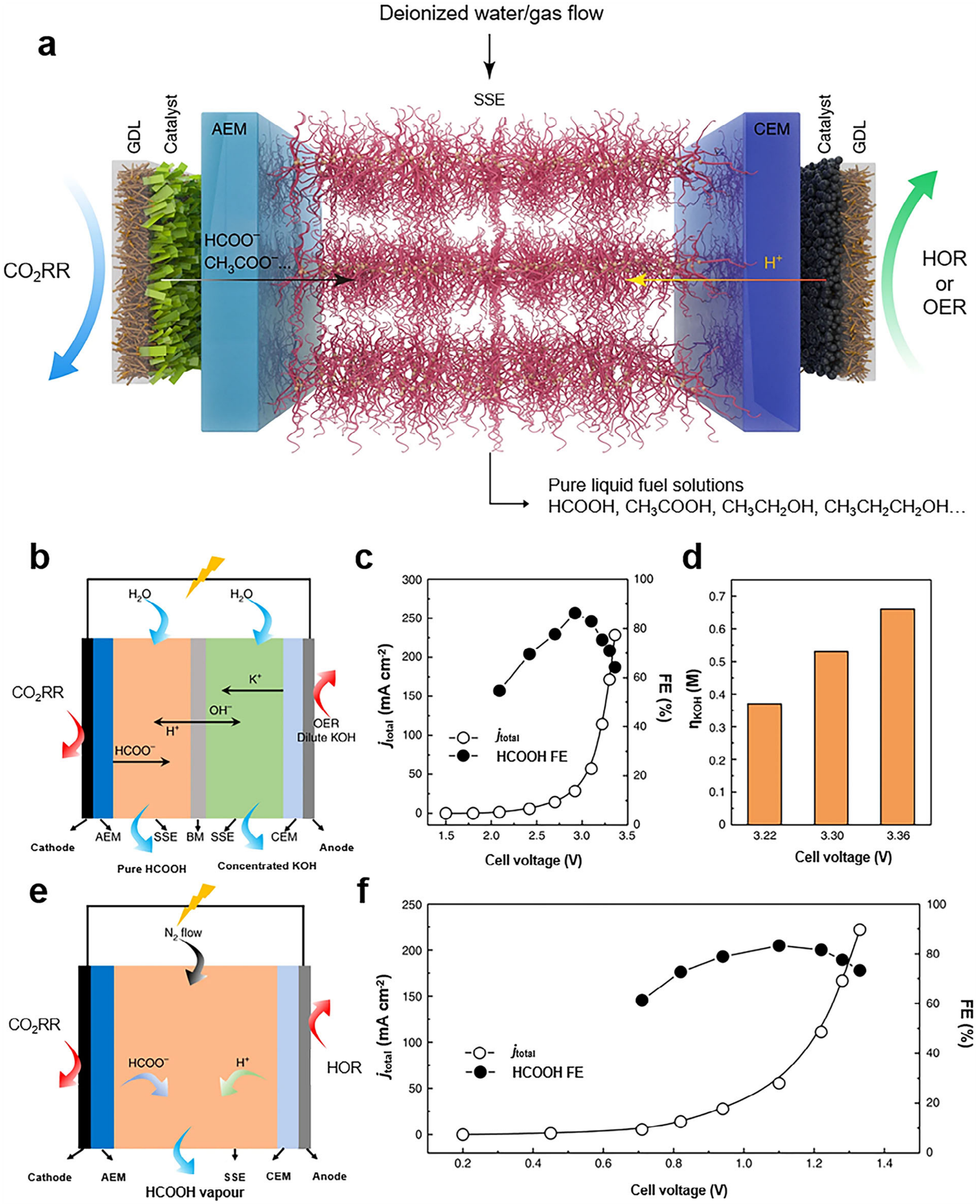

Figure 8. a) The schematic diagram of the SSE MEA CO$_2$RR electrolyzer. b) The schematic demonstration of the four-chamber symmetric SSE CO$_2$RR electrolyzer. Yellow and green SSE layers represent highly porous SSE-50 and SSE-OH$^-$, respectively. c) The current densities against cell voltages of a 2D-Bi//SSE-50 | BPM | SSE-OH$^-$// NiFe-LDH cell, and the corresponding HCOOH FEs. d) The concentration of pure KOH, which is simultaneously produced using the four-chamber solid cell during CO$_2$ reduction. e) Schematic illustration of the proposed all-solid–state cell for direct CO$_2$ hydrogenation. SSE is a highly porous SSE-50 proton solid conductor. f) The current densities and the corresponding HCOOH FEs against cell voltages on a 2D-Bi//Pt-C all-solid–state cell using the SSE-50 H$^+$ conducting solid electrolyte. The generated pure HCOOH vapor was brought out from the middle solid electrolyte using 100 SCCM humidified N$_2$. Reproduced with permission from.[51] Copyright 2019, Chuan Xia et al., under exclusive license to Springer Nature Limited.

configuration. In this design, a bipolar membrane (BPM) is used to separate cathode and anode compartments, where water is dissociated into H^+ and OH^- within the membrane, which are drawn toward the cathode and anode, respectively. The H^+ generated at the $HCOO^-$-conductor SSE side of BPM combines with $HCOO^-$ generated in the cathode compartment to produce pure HCOOH in the cathode-SSE. The OH^-, generated at the OH^--conductor SSE side of BPM, combines with K^+ in the anode compartment to regenerate KOH in the anode-SSE. The highest HCOOH current density in this four-chamber SSE MEA reaches 150 mA cm^{-2} at a cell voltage of 3.36 V (Figure 8c). And the concentration of the produced KOH solution can go up to 0.66 м (Figure 8d). Besides, the KOH solution produced can be recirculated into the anode electrolyte to reduce the operation cost. In another SSE MEA design (Figure 8e), by replacing the OER in the anode with hydrogen oxidation reaction (HOR), a 100% atom utilization can be achieved ($CO_2 + H_2 \rightarrow HCOOH$). In addition, the HCOOH vapor generated in the SSE is extracted by the humidified N_2 flow, which results in the all-vapor–phase cell operation without the liquid stream involved. It allows an 83.3% FE_{HCOOH} at a cell voltage of 1.1 V and the highest HCOOH current density of 163 mA cm^{-2} at a cell voltage of 1.33 V (Figure 8f).

Besides, it is proven that the augmentation of the catalyst surface area and the ion-exchange capacity of the membrane can contribute to the enhanced production rate while maintaining high CO_2 utilization,[52] which could be taken into consideration for the industrial large-scale production of the balance between the productivity and CO_2 utilization efficiency in eCO_2RR.

2.3. SOEC for High-Temperature Operations

With the technique of MEA assembly evolving, the temperature effect on the cell performance can be evaluated systematically. The temperature increase improves ionic conductivity, CO_2 mass transport, and water management, which allows the high current densities for eCO_2RR. In the meantime, the temperature difference of the cell can result in different reduction product selectivity due to the variations in adsorption energies of intermediates (i.e., *CO) on the catalyst surface.[53] In this case, the cells that can operate under robust conditions provide extra advantages. SOEC consists of a solid oxide electrolyte for conducting oxygen ions, which can operate at high temperatures (typically from 600–800 °C for CO_2RR, **Figure** 9a cascade 2). In a CO_2RR oxygen ion-conducting SOEC, CO_2 is first converted to carbonate on the cathode and then dissociated into CO and O^{2-} at the triple-phase interface. Then, the produced CO desorbs from the cathode surface while O^{2-} travels through the dense electrolyte (oxygen ion-conductor) to the anode to form O_2 via OER.[54] The SOEC device does not require liquid input and does not generate carbonate ions, realizing high carbon utilization for eCO_2RR. The basic requirements for the materials in SOEC are ionic conduction, electronic conduction, and catalytic activity (cathode: CO_2RR and anode: OER). It makes the oxides (e.g., perovskites, Ruddlesden–Popper phase oxides, etc.) the most popular materials for SOEC fabrications.[55] Coupling heat and electricity, SOEC can perform under high temperatures, achieving high current density (ampere level) easily.[56] For example, a SOEC using single Ru atoms anchored $Ce_{0.8}Sm_{0.2}O_{2-\delta}$ as the oxygen ionic conductor can provide a current density of 2.39 A cm^{-2} at a cell voltage of 1.6 V at 800 °C.[57] The final CO_2RR product from SOEC is mainly CO, which serves as a major feedstock in syngas-related industries and other CO conversions.[58] SOEC is also scalable from single cells to stacks. It demonstrates high efficiency toward CO_2RR with a high potential for large-scale CO_2 conversion.[59] However, the most reported lifetimes of SOEC are <10 000 h, which is not satisfactory for economic competitiveness (at least 44 000 h or 5 years).[60] To achieve the industrial lifetimes of SOEC, the thermal compatibility of electrode materials, ionic conductors, and electronic conductors is pivotal. The discovery of novel compatible materials and the modification strategies of current state-of-the-art materials (e.g., yttria-stabilized zirconia [YSZ] as an ionic conductor and perovskite oxides as electrode materials) need to continue.[61] Moreover, the application of SOEC requires high energy input. For future industrialization, SOEC should be applied in clean energy-rich areas or with industries generating extra waste energy.

2.4. Cascade Electrolyzer Designs for Future Industrialization

As discussed in the previous sections of this review, CO_2RR occurs differently under different conditions (e.g., electrolytes with different pH values, different temperatures, and different electrolyzers). The catalysts are not always compatible under all operational conditions. Integration of multiple incompatible catalysts in one continuous-flow reaction system is of paramount significance for green synthetic chemistry.[62] For example, to produce C_{2+} products from CO_2RR, there are several options. As depicted in Figure 9a, the purified CO_2 can be obtained from industrial waste and direct air capture. For a direct one-route production of C_{2+} products in CO_2RR, the most capable catalyst is Cu-based materials that can directly convert CO_2 into C_{2+} products under room temperature with a CO_2RR electrolyzer (direct route at the top of Figure 9a). Although simple, this direct route production demands highly efficient catalysts with high FE, which is still a challenge for Cu-based CO_2RR catalysts.[63] Since *CO is the key intermediate for C_{2+} production in CO_2RR, decoupling the one-route CO_2—C_{2+} reaction into the two-route CO_2—CO + CO—C_{2+} reactions seems attractive. The electrochemical reduction reaction of CO (CORR) undergoes the C—C coupling more easily than CO_2RR, which allows high FE for C_{2+} products at low overpotentials without the concerns for the carbonation and the CO_2 cross-over issues (Figure 9b,c).[64] Many metal-based catalysts exhibit industrial-relevant activities for CO_2RR to CO, such as Au, Ag, and transition-metal single-atom catalysts (SACs).[65] By employing these CO-production catalysts first to efficiently produce CO from CO_2RR and then Cu-based catalysts to perform CO—C_{2+} production, the CO_2—C_{2+} reaction is decoupled into two room-temperature CO_2RR electrolyzer operations (cascade 1 in the middle of Figure 9a) with better C_{2+} product selectivity and activity than that of the direct one-route reaction. Moreover, the SOEC can operate CO_2—CO at high temperatures without the concerns of carbonation that happens in the room temperature CO_2RR electrolyzer, giving a higher carbon utilization efficiency. Applying the SOEC to fulfill the CO_2—CO step is also a promising approach to achieve the two-route reaction of CO_2—C_{2+} (cascade 2 at the bottom of Figure 9a). By applying highly selective

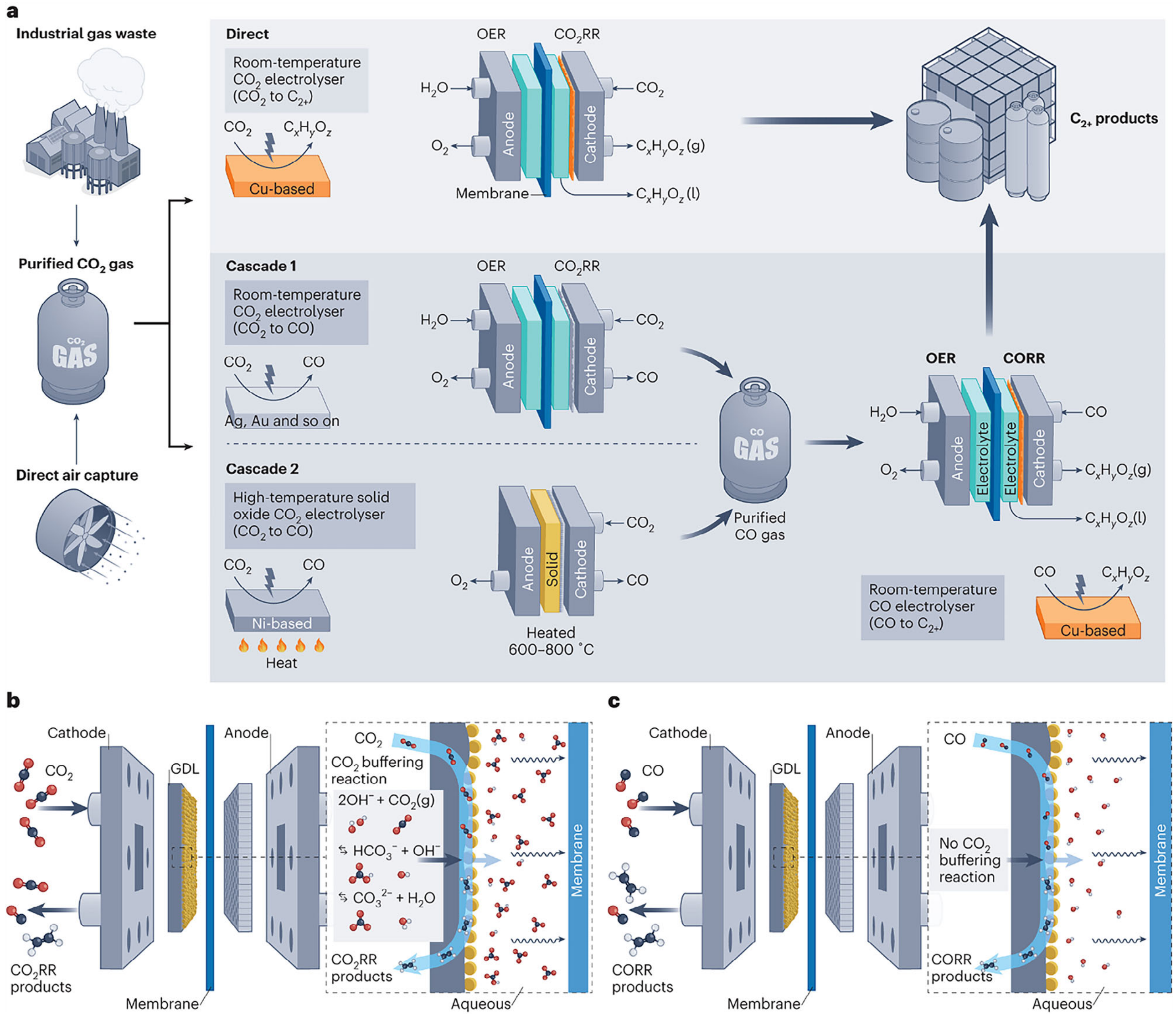

Figure 9. a) The setup diagrams of the CO_2RR electrolyzer for C_{2+} products. Top: direct route; middle: cascade 1 route of the two-route CO_2—C_{2+} reaction; bottom: cascade 2 route of the two-route CO_2—C_{2+} reaction. b) The schematic of CO_2RR in MEA electrolyzer, emphasizing the reaction between CO_2 and the generated OH^- to generate (bi)carbonate ions (CO_3^{2-}/HCO_3^-). The carbonate ions formed on the cathode side are then transported to the anode side. Atom code: O, red; C, black; H, white. c) The schematic of CORR in the MEA electrolyzer, illustrating that no pH buffering reactions with the generated OH^- ions populate on the catalyst surface. Reproduced with permission from.[67] Copyright 2023, Springer Nature Limited.

catalysts in the second step of the two-route cascade reaction, the continuous production of a specific chemical with high purity can be achieved. For example, the combination of a covalent organic framework (PcNi-DMTP) and a metal–organic framework (MAF-2) allows the highly efficient reaction of CO_2—CO-acetate to produce a 20 mM acetic acid aqueous solution with 95+% purity in 200 h.[66] With the support of the renewable/recyclable energy supply, these cascade electrolyzer designs are likely to be adapted in future large-scale industrialization because of the efficiency and economic benefits.

The cascade strategy is not limited to electrolyzers. The integration of CO_2RR electrolyzers with other catalytic techniques and devices, such as photovoltaic and conventional catalysis, can achieve the production of daily necessities for a grand market. By coupling the photovoltaic-powered CO_2RR electrolyzers with a five-enzyme cascade platform, Xiong's group successfully achieved the conversion from CO_2 to formate to C_6 sugar (L-sorbose).[68] It has a 3.5% efficiency of solar-to-food energy conversion, opening a pathway for artificial food synthesis via CO_2 reduction.

2.5. Liquid-Fed Electrolyzer and Anodic Reactions other than OER

EE, the ratio of the energy stored in the CO_2RR product and the total electricity input of eCO_2RR, is an important metric for economic feasibility that guides industrial implementation.[69] The high EE requires the CO_2RR cell design to achieve high FE

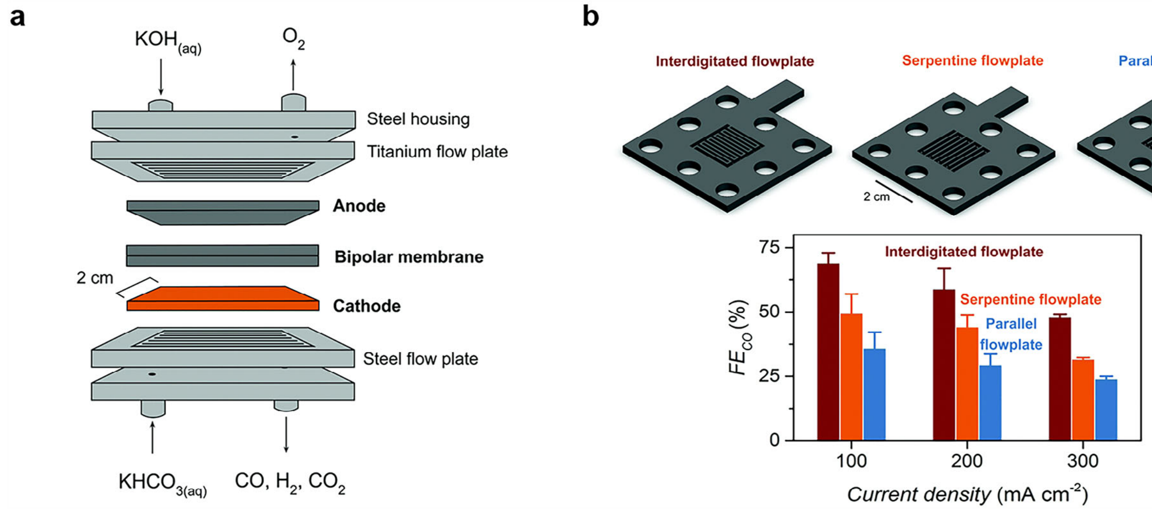

Figure 10. a) Schematic depiction of the flow cell with a bipolar membrane, silver cathode, and bicarbonate feedstock. b) Electrolysis using different flow plate geometries (Render of interdigitated, serpentine, and parallel cathodic flow plate patterns) and FE_{CO} as a function of current density for interdigitated, serpentine, and parallel flow plates tested in the bicarbonate electrolyzer with porous metal electrodes. Reproduced with permission from.[73] Copyright 2021, RSC Publishing.

at industrially relevant current densities, high CO_2 single-pass conversion, and high catalytic CO_2 utilization at the same time. During CO_2RR, CO_2 conversion usually comes with some non-catalytic CO_2 consumption (e.g., the carbonation issue aforementioned), which interferes with the calculation of the actual CO_2 consumption. Peter Strasser's group proposed a carbon crossover coefficient (CCC) that helps diagnose CO_2 loss in the zero-gap electrolyzer to validate the non-catalytic CO_2 consumption in CO_2RR.[70] The proposed CCC was formulated in three different limiting reaction-transport scenarios (i. pure OH^- crossover; ii. pure CO_3^{2-} crossover; iii. pure HCO_3^- crossover), which associates the exit flow rate with the applied cell current and FE. Under the ideal conditions (e.g., the aforementioned three limiting reaction-transport scenarios), CCC can experimentally predict the non-catalytic CO_2 consumption in acid-based media. It facilitates the analysis of the kinetic parameters of the electrolyzer (such as catalyst loading and single-pass conversion rate). Although the actual CO_2RR usually mingles different kinds of non-catalytic carbon transfers, making the ideal CCC model difficult to predict the real non-catalytic carbon crossovers, it is still a promising direction to the accurate calculation of CO_2 consumption (e.g., to predict undesired CO_2 losses) and the underlying mechanism demystification in CO_2RR to improve the electrolyzer design.

2.5.1. Liquid Bicarbonate Electrolytes as CO_2 Carrier

To achieve an operation with high EE, the focus falls on the optimizations of carbon utilization, FE of the catalysts, economic anodic oxidation reactions, etc. The bicarbonate electrolyzers (BCE) require OH- to react with CO_2 to form the bicarbonate-rich electrolyte, linking the upstream carbon capture and downstream CO_2RR for future industrialization. Liquid bicarbonate solutions, which serve as a liquid CO_2 carrier, deliver high concentrations of captured CO_2 to the cathode, while the low solubility of O_2 in aqueous media maintains a low O_2 concentration at the same cathode surface.[71] By optimizing the cell design, the efficiency of BCEs can be further improved. For example, Shen et al. prepared a CoPc@carbon nanotube catalyst to activate CO_2 in a hierarchical two-flow–path BCE design and obtained a one-third enhancement in total EE.[72] All these promising results demonstrate the potential of BCE in the practical flue gas (O_2:N_2:CO_2 = 5:80:15, volume ratio)-supplied eCO_2RR industry with high EE. Moreover, Zhang et al. employed the BPM strategy with flow pattern improvements in BCE to produce CO from CO_2RR (**Figure 10a**) without the gas supply of CO_2.[73] The BPM dissociates water into H^+ and OH^- and provides them to the cathode and anode, respectively. A porous Ag metal free-standing electrode is the working electrode for CO_2RR. Figure 10b exhibits the three different flow patterns (parallel, serpentine, and interdigitated flow plates) that the authors tested in this cell design. The interdigitated flow pattern presents the highest eCO_2RR performance among them (Figure 10b, bottom). It illustrates the enhancement of integrating different cell strategies in CO_2RR electrolyzer designs.

2.5.2. Replacing Anodic Oxygen Evolution with Hydrogen Oxidation and More

For the counter-reaction, OER is the most common one for CO_2RR as it uses water to proceed with the oxidation. However, some conditions in eCO_2RR (e.g., weak-alkaline or neutral media with low temperature) do not favor OER over other electrolyzers (such as alkaline water electrolyzers and SOEC).[74] OER also requires a high thermodynamic potential (1.23 V vs RHE) to occur, which demands a high cell voltage for the OER-paired CO_2RR electrolyzer. Zhang et al. replaced OER with HOR in a BCE electrolyzer to realize the highly efficient eCO_2RR to CO.[75] **Figure 11a** demonstrates the BCE cell configuration that the authors employed. The HOR|CEM|HCO_3^- electrolyzer configuration requires a much lower cell voltage (2.3 V, on the left

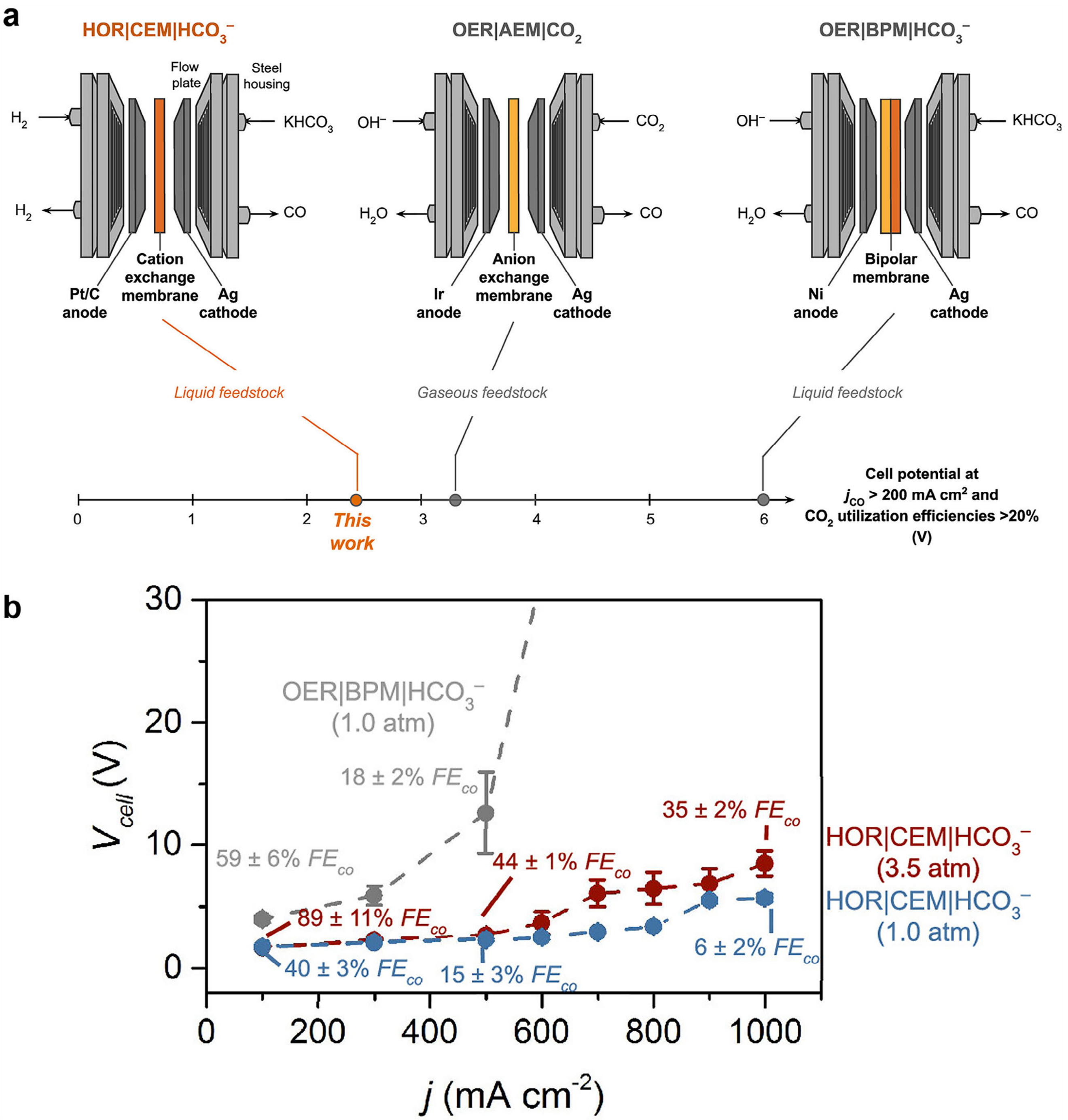

Figure 11. a) The CO_2—CO electrolyzer configurations. Left: HOR|CEM|HCO_3^-. Middle: the OER|AEM|CO_2 electrolyzer. Right: the OER|BPM|HCO_3^- electrolyzer. The nomenclature follows the rule of "anode|membrane|cathode". b) The cell voltage (V_{cell}) values as a function of current density from 100 to 1000 mA cm^{-2} for HOR|CEM|HCO_3^- and OER|BPM|HCO_3^- electrolyzers under 3.5 and 1.0 atm. Reproduced with permission from[75] under the terms of the CC-BY-NC-ND 4.0 license.

of Figure 11a) than those of the OER|AEM|CO_2 (≈3.2 V, on the middle of Figure 11a) and OER|BPM membrane|HCO_3^- (≈6 V, on the right of Figure 11a) to achieve a CO current density larger than 200 mA cm^{-2}. This HOR|CEM|HCO_3^- electrolyzer configuration can reduce 3 M $KHCO_3$ to CO at 220 mA cm^{-2} at a cell voltage of 2.3 V with a CO_2 utilization efficiency of 40% and outperform the OER|BPM|HCO_3^- electrolyzer configuration in the aspects of FE_{CO} and current density (Figure 11b). It is suggested that among all the three configurations in Figure 11a, HOR|CEM|HCO_3^- is the most profitable (with a net present value of 48.96 based on a 20-year plant life), considering the future market analyses (CO sale price of $ 0.6 Kg^{-1}, clean H_2 price of \$ 1 Kg^{-1}, CO_2 price of \$ 50 $tonne^{-1}$, and electricity of \$ 0.03 kW^{-1} h^{-1}).

In addition to HOR, several oxidation reactions, such as methanol oxidation reaction (MOR), glycerol oxidation reaction (GOR), urea oxidation reaction (UOR), and chloride oxidation reaction, have lower thermodynamic potentials than the OER are promising candidates to couple with CO_2RR, enabling the simultaneous production of value-added products at the anode during eCO_2RR.[76] For instance, Li et al. coupled CO_2RR with MOR, which has a thermodynamic potential of 0.103 V vs RHE for formic acid production, in a CO_2RR–MOR electrolyzer. They achieved formate production at both the cathode and anode with a total coulombic efficiency of over 180%, reaching a current density of 130 mA cm^{-2} at a cell voltage of 2.1 V for over 100 h of operation.[77] Similarly, coupling CO_2RR with allyl alcohol oxidation enabled a reduction in cell voltage by 0.7 V compared to typical acidic CO_2RR-OER electrolyzers at 100 mA cm^{-2}, simultaneously producing CO and acrolein.[78] Additionally, a CO_2RR/GOR coupled electrolysis system using a membraneless microfluidic flow electrolyzer cell achieved a 75–85% FE for GOR products (i.e., tartronate, formate, glycerate, glycolate, lactate, and oxalate) and ≈100% FE_{CO} for CO_2RR at a current density of 200 mA cm^{-2}. This setup lowered the cell voltage by ≈1 V compared to a CO_2RR/OER system and maintained stable operation for 5 h.[79] In another example, a CuNi-CNT catalyst used in a CO_2RR/UOR electrolyzer achieved a low cell voltage of 1.81 V at 10 mA cm^{-2}, which is 200 mV lower than that of a comparable CO_2RR/OER system.[80] These alternative anodic oxidation reactions provide valuable opportunities for simultaneously managing industrial waste and generating value-added products. However, durability remains a significant issue for practical electrolyzers. Rational and robust hybrid electrolyzer designs to accommodate cathodic and anodic reactions, which often require different operation environments, present challenges when switching anodic reactions.

3. Rational Water Electrolyzer Design

Although HER is the competing reaction in CO_2RR, H_2 produced from HER is a clean energy source that can be utilized in many practical applications, such as fuel cell vehicles. As aforementioned, HOR can replace OER in eCO_2RR to reduce the overall energy consumption. To conduct the sustainable operation of this practice, green H_2 produced from renewable techniques is a must to control the overall carbon emission. Thus, green H_2 plays an essential part in the global strategy of reducing carbon emissions.[81] Herein, water splitting that consists of HER and OER is also an attractive topic for clean energy production.[82] Similar to eCO_2RR, traditional three-electrode H-cells (such as alkaline water electrolysis) cannot provide commercially relevant activity for water splitting.[83] The highly efficient MEA electrolyzer (e.g., PEM and AEM) for water splitting awaits profound exploration.

3.1. PEM Electrolyzer

One of the promising electrolyzers for water splitting is PEMWE, which works normally in acid environments. In a typical PEMWE, the generated H^+ in the anode side from OER travels through PEM to the cathode side, forming H_2.[84] The zero-gap PEMWE provides great promise for the scalable and sustainable generation of green hydrogen. The sluggish OER remains a challenge for water electrolysis.[85] Many works are dedicated to the fabrication of highly efficient OER catalysts for water electrolysis, boosting HER.[86] PEMWE usually demands high-loading noble metal-based catalysts to survive the corrosive environment,[87] which is not cost-efficient and not ideal for industrialization. Kong et al. applied MnO_2 as the acid-stable and earth-abundant OER catalyst in PEMWE (**Figure** 12a).[88] The MnO_2 catalysts are designated as M94%, M85%, M67%, and M60% according to the concentration of planar oxygen (O_{pla}) in the samples. As shown in Figure 12b, MnO_2 catalysts exhibit close activities under cell voltages of 2.0 and 1.8 V with a Nafion-115 (N-115, thickness of 127 µm) membrane. When decreasing the electrical resistance by switching to Nafion-212 (N-212, thickness of 50.8 µm), the current density increases to 2000 mA cm^{-2} at a cell voltage of 2.0 V for the M94% sample. After the high-frequency correction, a cell voltage of 1.88 V is demanded to reach 1000 mA cm^{-2} (Figure 12c). Besides, Figure 12d shows that the sample of M94% can operate water electrolysis for over 1000 h at a current density of 200 mA cm^{-2}. It is attributed to the stability of the M94% sample at high current densities (Figure 12e). Tao et al. came up with a hierarchical IrRu sub-nanosheet/nanowire catalyst design to reduce the noble metal loading for PEMWE.[89] Figure 12f depicts the electrical contact of the conventional nanoparticle catalysts with high mass loading. When the catalyst loading is decreased, the inhomogeneous electrode gives poor electrical contact, leaving a big void area and decreasing the Ir utilization. As illustrated in Figure 12g, an enhanced electrical contact can be achieved through the ultrathin nanosheet catalyst engineering that augments through/in-plane conductivity. However, this nanosheet strategy results in the catalyst packing perpendicular to the reactant and product flows, increasing the mass transport resistance. Figure 12h depicts a hierarchical nanosheets/nanowires (HNWs) electrode with the gas/liquid diffusion layer design, which integrates the advantages of high conductivity and high mass transport. By applying this catalyst design with the catalyst-coated membrane (CCM) MEA electrolyzer, a peak current density of 6.0 A cm^{-2} at a cell voltage of 2.44 V can be achieved by IrRu HNWs (Figure 12i). IrRu HNWs can also reach an Ir mass current density of over 8.0 A g_{Ir}^{-1} at a cell voltage of 2.0 V (Figure 12j) in PEMWE.

Until now, the most commonly employed commercial PEM is the perfluorosulfonic acid membrane for PEMWE. This type of PEM suffers from issues such as fluorine-based, cross-over, and durability.[90] To be adapted to vast operating conditions, the alternatives need to be exploited.

3.2. AEM Electrolyzer

PEMWE requires acid-resistant catalysts with noble metal-based materials, which increases the total cost of the electrolysis. Switching the electrolyte to a basic one avoids these issues. When water splitting is operated in an alkaline environment, it requires an AEMWE.[91] Nowadays, many efficient AEMWE catalysts are adopted from PEMWE catalysts. AEMWE therefore focuses on

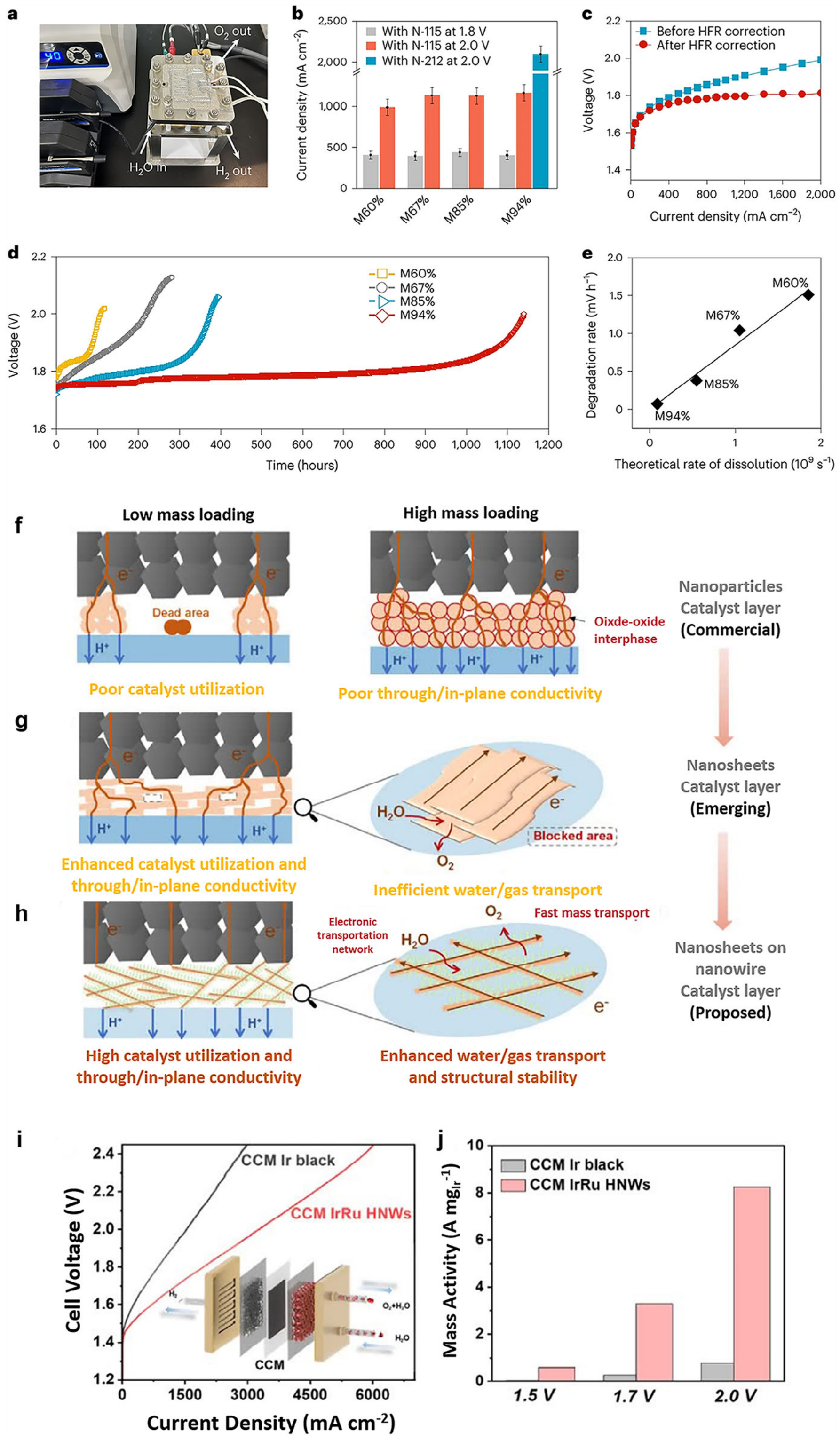

Figure 12. a) The set-up photo of the PEMWE. b) Current densities of M94%, M85%, M67%, and M60% at cell voltages of 2.0 and 1.8 V, respectively. c) The polarization curves of M94% in the N-212 membrane MEA. d) The long-term durability of M94%, M85%, M67%, and M60% in PEMWE at 200 mA cm^{-2} with Nafion-115 membrane. e) The MnO_2 theoretical dissolution rate was calculated at 80 °C versus the experimental degradation rate in PEMWE. Reproduced with permission.[88] Copyright 2024, Shuang Kong et al., under exclusive license to Springer Nature Limited. The schematics of f) the catalyst layer of commercial nanoparticles, g) the catalyst layer of ultrathin nanosheets, and (h) the catalyst layer of HNWs in PEMWE. Electrochemical performance of i) the polarization curves of the catalysts and (j) the Ir mass activities of the catalysts' various cell voltages in the CCM PEMWE. Reproduced with permission from.[89] Copyright 2024, Published by Elsevier Inc.

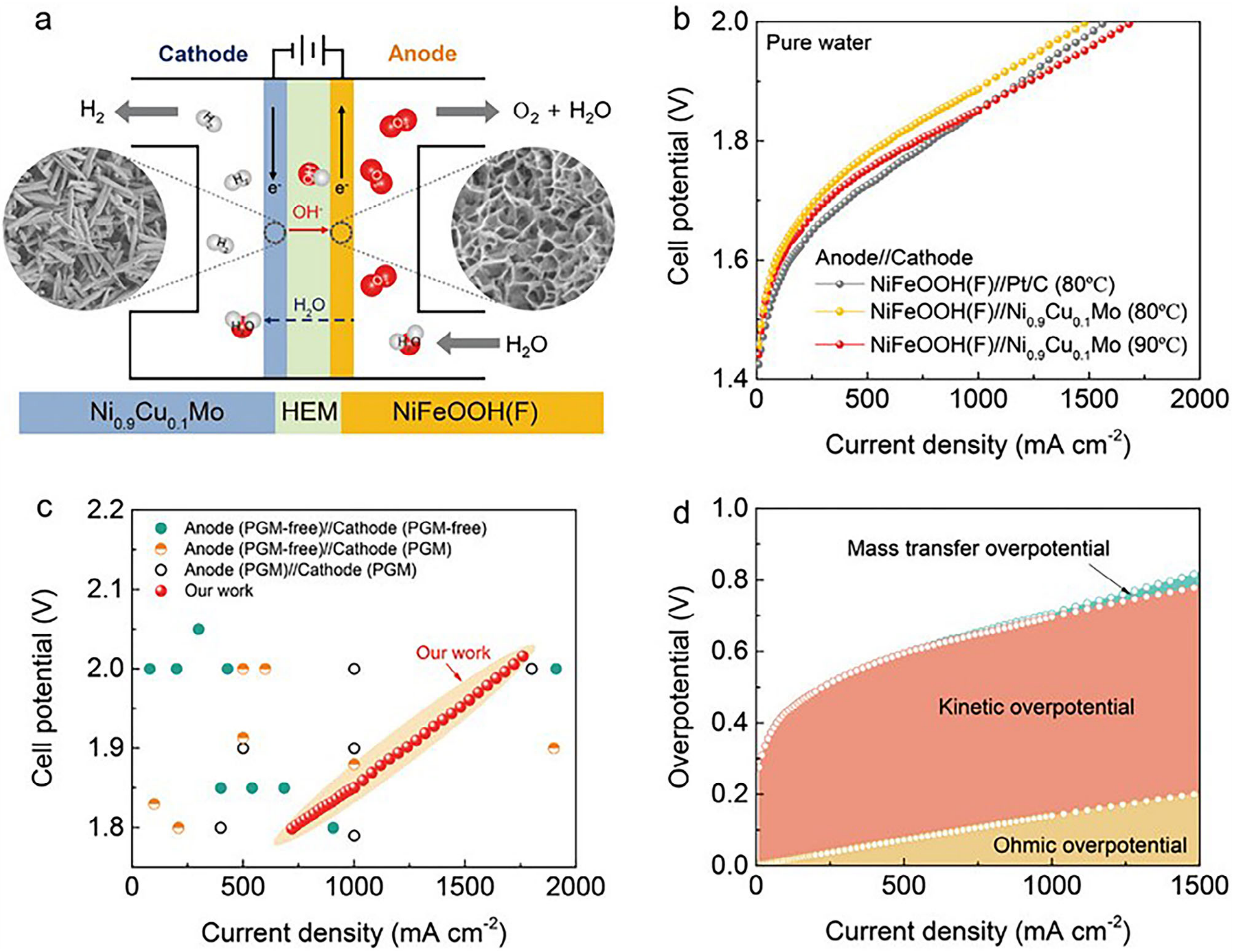

Figure 13. a) The structural schematic of the HEM water electrolyzer. b) The polarization curves of the NiFeOOH(F)//Ni0.9Cu0.1Mo and NiFeOOH(F)//Pt/C in the HEM water electrolyzer under 80 and 90 °C. c) The comparison of the state-of-the-art water splitting performance with the NiFeOOH(F)//Ni0.9Cu0.1 HEM water electrolyzer system. d) The breakdown of the mass transport, catalytic kinetics, and ohmic resistance contributions in overvoltage for the NiFeOOH(F)//Ni0.9Cu0.1 HEM water electrolyzer system under 80 °C. Reproduced with permission from.[96] Copyright 2024, Wiley-VCH GmbH.

discovering the unique, highly efficient materials on its own. Since noble metal-based catalysts are no longer a must in alkaline environments, many inexpensive catalyst options are put on the table, including transition metals,[92] metal oxides,[93] metal–organic frameworks,[94] etc.[95] Moreover, the membrane developed for AEMWE is still at the beginning stage. To make the commercial AEM product available, more studies need to be dedicated to the field. Yang et al. employed a hydroxide exchange membrane (HEM) with transition metal-based catalysts to allow pure water-fed water electrolysis (**Figure 13a**).[96] By using NiCuMo catalysts as cathode catalysts for HER and the fluoride NiFeOOH (NiFeOOH(F)) as the anode catalyst for OER, the HEM water electrolyzer allows the better catalytic water splitting performance than the system of the commercialized platinum-group material (PGM) catalyst (Pt/C, Figure 13b). The current density of this HER water electrolyzer system reaches 1.7 A cm^{-2} at a cell voltage of 2.0 V, which surpasses most of the reports (Figure 13c). Figure 13d analyzes the contribution of mass transport, catalytic kinetics, and ohmic resistance in overvoltage. It suggests that the high catalytic performance can be attributed to the low ohmic loss and low mass transport loss.

3.3. Bipolar Plates and Flow Patterns for Water Electrolyzers

Electricity expense plays a major role in industrial water electrolysis (e.g., for a 1 MW PEMWE operation). After the cost of electricity, the bipolar plate (BP, the electrically-conductive plate that holds stack components together in a cell) dominates the capital expense, accounting for over 50% of the cost of stack components in the PEMWE.[97] The oxidative and corrosive environment at the anode side of PEMWE limits BPs to be made of robust Ti-based materials.[90,98] However, long-term operation in water electrolysis inevitably leads to corrosion and degradation of metal-based BPs due to acidic and humid conditions. It has been found that protective coatings on BPs can mitigate

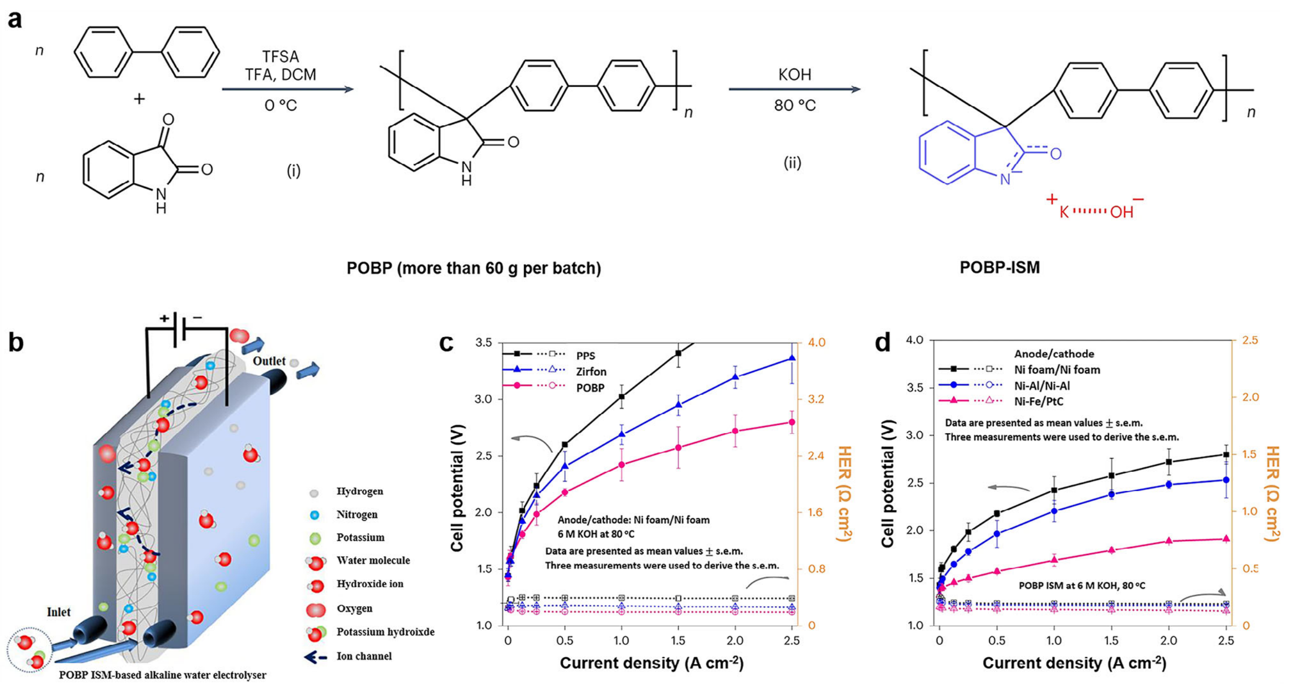

Figure 14. a) The schematic of the synthesis of POBP-ISM. TFSA: trifluoromethanesulfonic acid; TFA: trifluoroacetic acid; DCM: Dichloromethane. b) The schematic illustration of the POBP-ISMs AWE. c) The catalytic performance and HFR comparisons for different membranes: PPS diaphragm (700 ± 10 µm), POBP-ISM (45 ± 5 µm), and Zirfon (500 ± 10 µm). d) The catalytic performance and HFR comparisons for different electrode catalysts in POBP-ISMs AWE at 80 °C. Reproduced with permission from.[107] Copyright 2024, Xu Hu et al., under exclusive license to Springer Nature Limited.

degradation issues.[99] Since Ti itself is costly, especially when coated with noble metal-based materials, alloying Ti with low-cost metals presents a cost-efficient method to modify BPs.[100] According to IRENA, BPs offer a medium potential for reducing the capital expense of water electrolysis.[101] Popular BP alternative materials are nickel, graphite, and stainless steel (SS) due to cost considerations.[102] Several attempts to coat Ti-BPs with inexpensive protective layers have shown promising results.[103] For example, a nitrogen–chromium composite deposited by cathode plasma improved the performance of Ti-BPs.[98] In an anode compartment, the TiN/CrN-coated BPs demonstrated good conductivity and considerable corrosion resistance in PEMWE. Apart from metal-based BPs, carbon-based BPs are also of interest owing to their inexpensive nature. Messing et al. utilized the uncoated carbon BPs (C-BPs) as an alternative to Ti-BPs.[104] They found that C-BPs in PEMWE exhibited lower degradation rates (16.41 µV h^{-1} at 1 A cm^{-2} and 31.92 µV h^{-1} at 3 A cm^{-2}) compared to Ti-BPs. This highlights the potential of carbon-based BP applications in water electrolyzers, aiming to reduce cell setup costs.

Similar to eCO_2RR, the flow patterns embedded in BPs impact the overall performance of water electrolyzers. Li et al. analyzed three different flow patterns (i.e., cascade, parallel, and serpentine) in PEMWE. They found that the ohmic overpotential at the cathode was influenced by the flow pattern, while the flow pattern at the anode affected the overpotential by addressing the liquid water shortage issue at CL. The counter-flow and co-flow configurations had minimal impact on catalytic performance. Under conditions of 0.3 MPa and 120 °C, the serpentine and cascade flow patterns at the cathode and anode, respectively, exhibited the optimal performance, achieving a current density of 2 A cm^{-2} at a cell voltage of 1.69 V.[105] Hassan et al. investigated five types of circular flow patterns (i.e., one-path and two-path serpentine, two-segment serpentine, two-channel serpentine, and four-segment serpentine) in PEMWE with an MEA area of 38.5 cm^2. They analyzed the distributions of temperature, liquid saturation, pressure, velocity, and current density for these patterns. The study indicated that the higher flow velocities contributed to better distributions of current density and temperature. The decreases in velocity, the number of turns, and path length led to increased pressure drops. The one-path and two-path serpentine patterns demonstrated the most favorable temperature uniformity and flow distribution among all the patterns. Additionally, the two-path, two-segment, and four-segment serpentine flow patterns provided the optimal polarization curves at a cell voltage of 2.1 V.[106]

3.4. Ion-Solvating Membranes for Improved Alkaline Stability

Apart from PEM and AEM, research on other types of water electrolyzer membranes is always a popular topic. Ion-solvating membranes (ISMs) obtain ionic conductivity through the liquid electrolyte uptake rather than through the determined ionic groups in the structure. This unique property offers ISMs the opportunity to outperform AEM instability because of the absence of the issue of the anion exchange group degradation. Hu et al. fabricated poly(oxindole biphenylene)-based ISMs (POBP-ISM) for highly efficient AWE.[107] As depicted in **Figure 14a**, the biphenyl and isatin are first polymerized by super-acid catalysis. Then, oxindole is introduced to the aryl-ether–free polymer to form POBP. The authors further tested ISMs on an AWE (Figure 14b) to test the water electrolysis catalytic performance. Figure 14c shows that ISMs exhibit better AWE performance than the state-of-the-art Zifron and polyphenylene sulfide (PPS) membranes. By pairing the Ni—Fe anode electrode with the Pt/C cathode electrode, a current density of 2.0 A cm^{-2} at a cell voltage of 1.9 V can be realized, owing to the low high-frequency resistance (HFR) of POBP-ISM (Figure 14d). ISMs reveal excellent alkaline stability without appreciable conductivity loss over 15 000 h. In addition, this ISMs MEA water electrolyzer allows the utilization of transition metal-based inexpensive catalysts in a wide temperature range from −35 to 120 °C.

3.5. Floating Electrode Cell Design for Enhanced Water Electrolysis Performance

Other than the membrane part, the configuration modifications on the electrode part also demonstrate interesting results. Shi et al. designed a floating electrode strategy to evaluate HER of single-atom dispersed Pt (s-Pt) on MoS_2 (s-Pt/1T′-MoS_2) catalyst for the maximized mass transport and Pt utilization. The scheme of the floating electrode system is displayed in **Figure 15a**, where the produced H_2 does not interfere with the catalyst–electrolyte interface. Three groups of floating electrodes were prepared for both s-Pt/1T′-MoS_2 and the commercialized HiSPEC 9100 Pt/C (denoted as E1, E3, and E5 for s-Pt/1T′-MoS_2 with the loadings of 398, 583, and 618 ng cm^{-2}, respectively; E2, E4, and E6 for HiSPEC 9100 Pt/C with the loadings of 286, 570, and 833 ng cm^{-2}, respectively). Figure 15b,c shows that s-Pt/1T′-MoS_2 allows better HER performance than that of the commercialized HiSPEC 9100 Pt/C sample, both in the geometric and Pt mass current densities. The Pt mass current density at an overpotential of 50 mV of s-Pt/1T′-MoS_2 outperforms many state-of-the-art catalysts (Figure 15d). The mass-normalized exchange current densities ($j_{0,\,\mathrm{mass}}$) in Figure 15e,f further confirm the superior catalytic activity of s-Pt/1T′-MoS_2. s-Pt/1T′-MoS_2 affords a $j_{0,\,\mathrm{mass}}$ of 127 A $mg_{Pt}{}^{-1}$, which is in the same order as those of the high-mass transport techniques (Figure 15g).

3.6. SOEC for Highly Efficient Water Electrolysis

Both PEMWE and AEMWE operate at a temperature slightly higher than room temperature, with electrical efficiencies of between 65% and 75%. As mentioned in 2.4, SOEC offers highly efficient catalytic performance under high-temperature routes. It allows a 90% efficiency for H_2 production from water electrolysis.[109] On the one hand, for the conventional oxygen ion-conducting SOEC, H_2 is produced at the cathode from water electrolysis while O^{2-} travels through the YSZ electrolyte to generate O_2 at the anode, as depicted in **Figure 16a**. On the other hand, proton-conducting SOEC that uses proton-conducting oxides (e.g., barium-zirconates and barium-cerates) as electrolyte materials is also developed to produce H_2 from water electrolysis. Figure 16b shows the mechanism of the proton-conducting SOEC. O_2 is produced at the anode from water electrolysis while the proton travels through the proton-conducting oxide electrolyte to generate H_2 at the cathode. Due to the monotonicity of the electrolyte material, only one type of ion (O^{2-} or proton) can permeate the electrolyte. It limits the water electrolysis to occur only on one side of the electrodes (cathode and anode for oxygen ion-conducting SOEC and proton-conducting SOEC, respectively) in conventional SOECs. The fabrication of mixed ionic electrolytes that allow the permeation of both O^{2-} and protons can promote the H_2 and O_2 productions on the cathode and anode at the same time. Kim et al. designed a $BaZr_{0.1}Ce_{0.7}Y_{0.1}Yb_{0.1}O_{3-\delta}$ (BZCYYb) as the mixed ionic electrolyte to develop the hybrid-SOEC.[110] As illustrated in Figure 16c, the oxide ion and protonic defects in BZCYYb result in high mixed ionic conductivities for both O^{2-} and proton. It allows the counter diffusion of the oxygen and proton ions, realizing water electrolysis at both the cathode and anode of the hybrid-SOEC. By employing $NdBa_{0.5}Sr_{0.5}Co_{1.5}Fe_{0.5}O_{5+\delta}$ as the anode material and Ni as the cathode material, this hybrid-SOEC achieved a current density of 4.61 A cm^{-2} at a cell voltage of 1.5 V under 700 °C. This performance surpasses that of conventional SOECs under the same conditions, which typically reach 4.02 A cm^{-2} for oxygen ion-conducting SOECs and 3.17 A cm^{-2} for proton-conducting SOECs. However, the stability of this hybrid-SOEC was only tested for 60 h at 0.45 A cm^{-2} under 550 °C. It still demonstrates the potential of the novel SOEC design for the highly efficient water electrolysis industry.

With the high efficiency and scalability of SOEC, large-scale stacks of SOEC become promising for green H_2 production when coupled with renewable energy supplies.[111] The commercialization of H_2 production from SOEC is already underway. For example, FuelCell Energy utilizes SOEC technology to achieve up to 100% efficiency in H_2 production. Their SOEC platforms aim to reduce the cost and energy requirement of H_2 production by up to 35% compared to low-temperature electrolysis techniques. Furthermore, the company plans to expand its SOEC production facility capacity from 4 to 40 MW per year by 2024.[112]

4. In Situ Characterization Cell Design and Inspiration from Other Electrochemical Cells

To fully understand the mechanism of CO_2RR and HER, the techniques that can monitor the evolution of the reaction intermediates and the catalyst structure are of significance during the reaction. Given this concept, in situ and operando characterizations are developed.

4.1. In Situ Fourier-Transform Infrared Spectroscopy for the Detection of Essential Reaction Intermediates

Fourier-transform infrared spectroscopy (FTIR) is a powerful technique to detect the functional groups on the material surface. Since CO_2RR has many carbon-based intermediates formed during the catalytic process, FTIR is a desirable technique for demystifying the underlying mechanism of CO_2RR. Figure 16d depicts a stirred spectroelectrochemical in situ cell for attenuated total reflectance surface-enhanced infrared absorption spectroscopy (ATR-SEIRAS). The catalyst material is deposited on the ATR crystal to serve as the WE. The RE, gas inlet, and CE are connected through the designated cell configuration. Notably, the CE

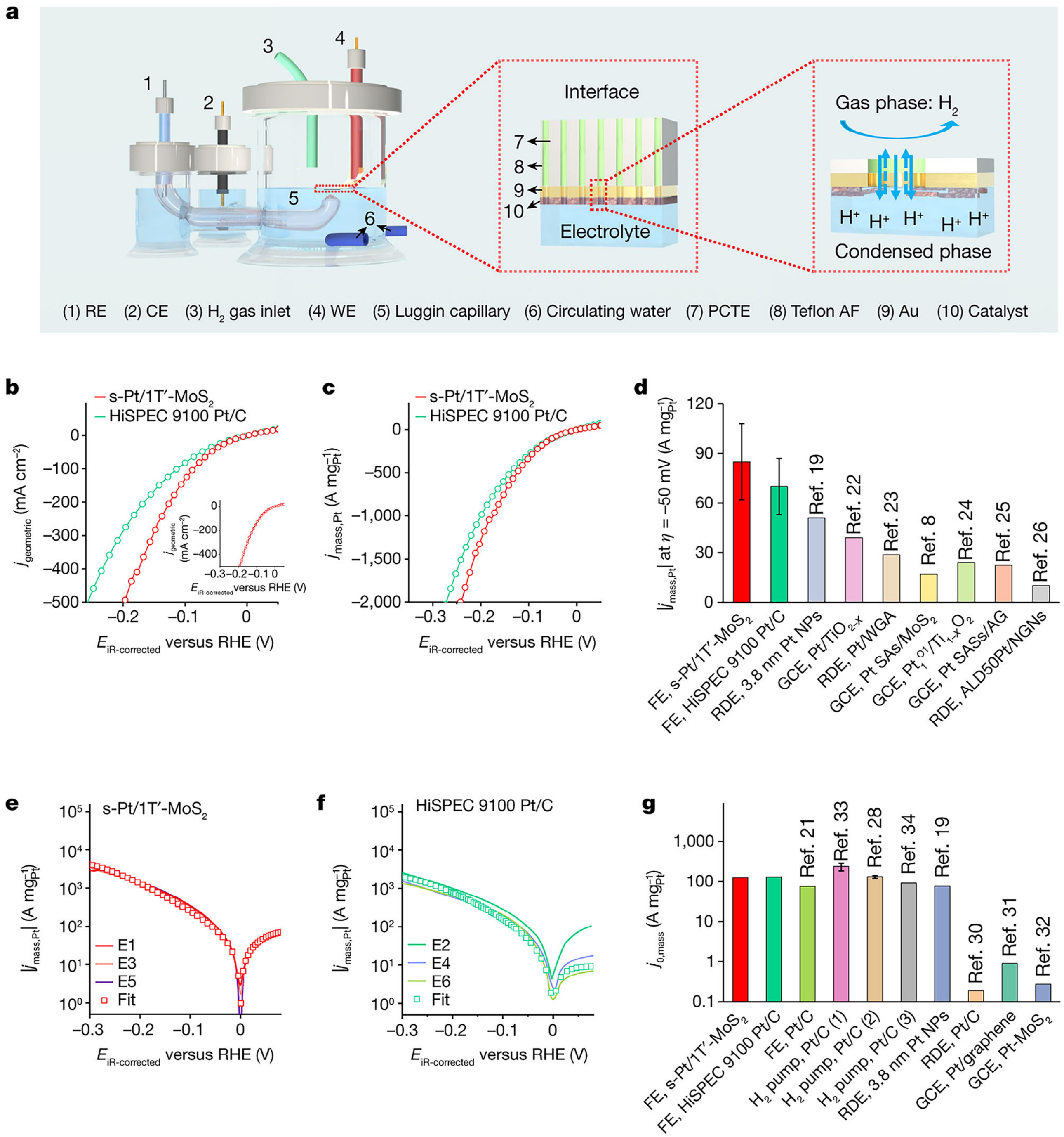

Figure 15. a) The schematic demonstration of the floating electrode setup. RE, reference electrode; CE, counter electrode; WE, working electrode; PCTE, polycarbonate track etch; Teflon AF, Teflon AF 2400 (DuPont). b) The geometric polarization curves of HER for HiSPEC 9100 Pt/C (E2) and s-Pt/1T′-MoS_2 (E1). The inset: the cyclic voltammogram of HER for s-Pt/1T′-MoS_2. c) The Pt mass-normalized polarization curves of HER for HiSPEC 9100 Pt/C (E2) and s-Pt/1T′-MoS_2 (E1). d) The mass activity comparisons at an overpotential of −50 mV ($\eta = -50$ mV) of HiSPEC 9100 Pt/C and s-Pt/1T′-MoS_2 with the state-of-the-art PGM electrocatalysts. e) The Pt mass activities of s-Pt/1T′-MoS_2 and the corresponding fitting result. f) The Pt mass activities of HiSPEC 9100 Pt/C and the corresponding fitting result. g) The comparison of the $j_{0,\text{mass}}$ of HiSPEC 9100 Pt/C and s-Pt/1T′-MoS_2 with the state-of-the-art electrocatalysts measured by different high mass transport techniques. The HER is performed in 1 M $HClO_4$ under H_2 (101 kPa) at 298 K with a 20 mV s^{-1} scan rate. FE in (d) and (g), floating electrode; RDE, rotating disk electrode; GCE, glassy carbon electrode. The reference numbers denoted in (d) and (g) are the reference numbers in the original article. Reproduced with permission from.[108] Copyright 2023, Zhenyu Shi et al., under exclusive license to Springer Nature Limited.

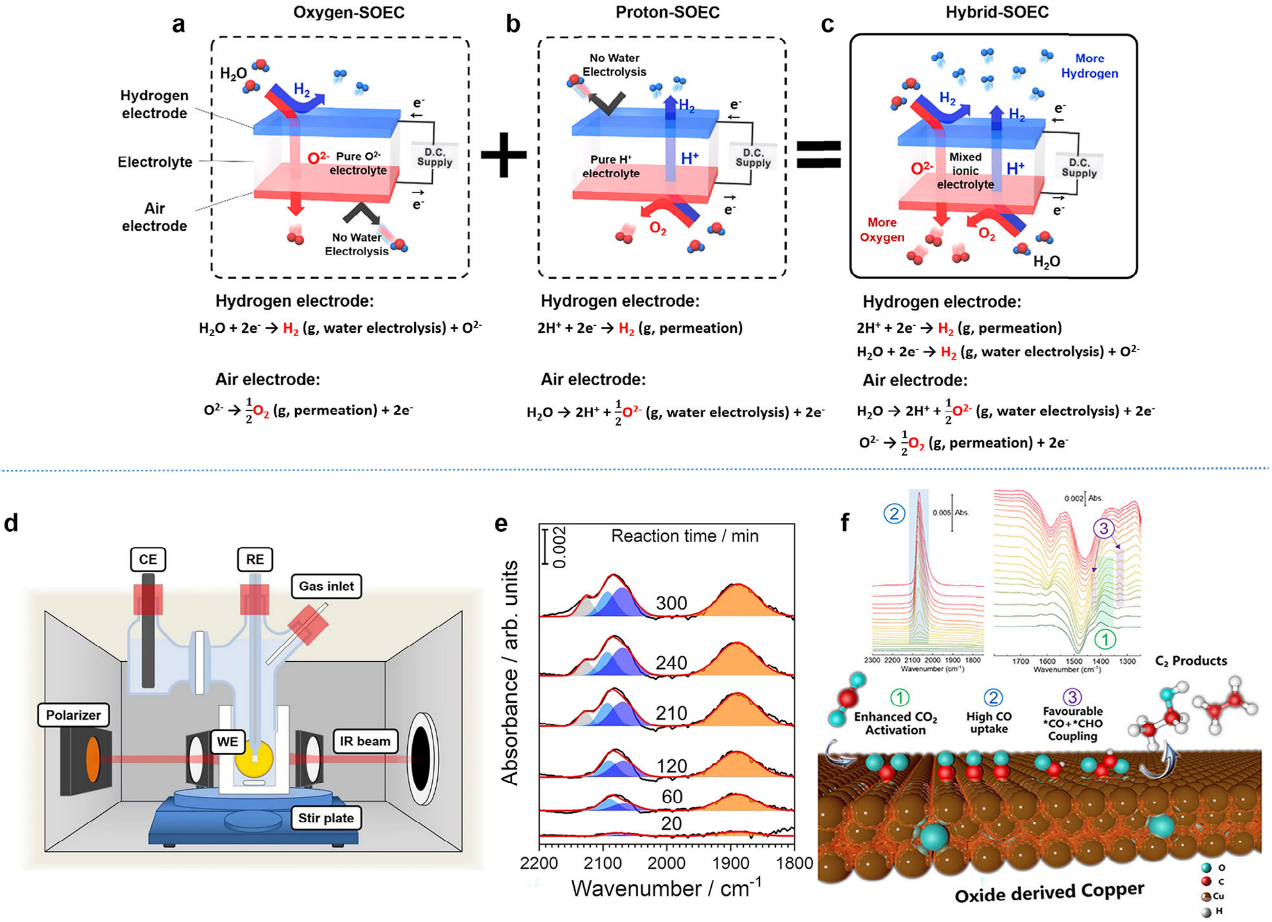

Figure 16. The schematics of a) Oxygen-SOEC, b) proton-SOEC, and (c) Hybrid oxygen–proton–SOEC systems. Reproduced with permission.[110] Copyright 2017, Elsevier Ltd. d) The demonstration of a stirred spectroelectrochemical in situ cell for ATR-SEIRAS. e) The four CO adsorptions with Gaussian fitting. Orange: the CO adsorption on the Cu single sites; blue: the CO adsorption on the Cu terrace sites; sky blue: the CO adsorption on the Cu step sites; gray: the CO interacting with K cationic species. Reproduced with permission from[113] under the terms of the Creative Commons CC BY license. f) The in situ infrared spectroscopic evidence of enhanced electrochemical CO_2 reduction and C—C coupling on oxide-derived copper. Reproduced with permission from.[114] Copyright 2024, American Chemical Society.

is separated from the main chamber by an ion exchange membrane to avoid contamination. In a typical ATR in situ FTIR cell, the ATR crystal is mounted on the bottom of the cell, allowing the IR beam to interact with the catalyst deposited on the ATR crystal. Differently, the ATR crystal of the in situ ATR-SEIRAS cell shown in Figure 16d is positioned at the side of the cell, which permits the use of a magnetic stir bar for improved uniformity. Combined with the time-resolved spectra, in situ FTIR becomes extremely practical in unveiling the reaction pathway. For example, in Figure 16e, the in situ SEIRAS finds that the sky blue peaks at ≈2100 cm^{-1} represent the CO adsorption on the Cu step site (denoted as CO_s). The blue peaks at ≈2070 cm^{-1} represent the CO adsorption on the Cu terrace site (denoted as CO_T). By monitoring the variations in wavenumbers and peak areas with time, in situ SERIRAS offers the opportunity to follow the trend of CO adsorption as CO_2RR progresses. In addition, with the association of FTIR peaks (corresponding to different Cu sites) and the applied potential during the electrochemical reaction, in situ SERIRAS also provides insights into the Cu site evolution with the different applied potentials.[113] Moreover, since different functional groups give fingerprint features in FTIR, the appearance and disappearance of FTIR peaks can reveal the evolution of CO_2RR intermediates to uncover the C_{2+} product formation pathway on Cu catalysts (Figure 16f).[114]

4.2. In Situ X-Ray Absorption Spectroscopy to Monitor the Variations in Chemical Properties

While the reaction intermediates are monitored by the functional group sensitive characterizations, such as FTIR, X-ray–powered techniques can keep track of the physical and chemical evolutions of the catalyst materials.[115] As illustrated in **Figure 17a**, the nano-focused X-ray can serve as the nanoprobe for Bragg coherent X-ray diffraction imaging (BCDI) to provide the structural evolution information, such as facets, defects, strain, and shape of the catalyst material. Besides, the X-ray absorption near edge spectroscopy (XANES) and extended X-ray fine structure spectroscopy (EXAFS) afford information on the chemical properties such as bonds, oxidation states, and coordination

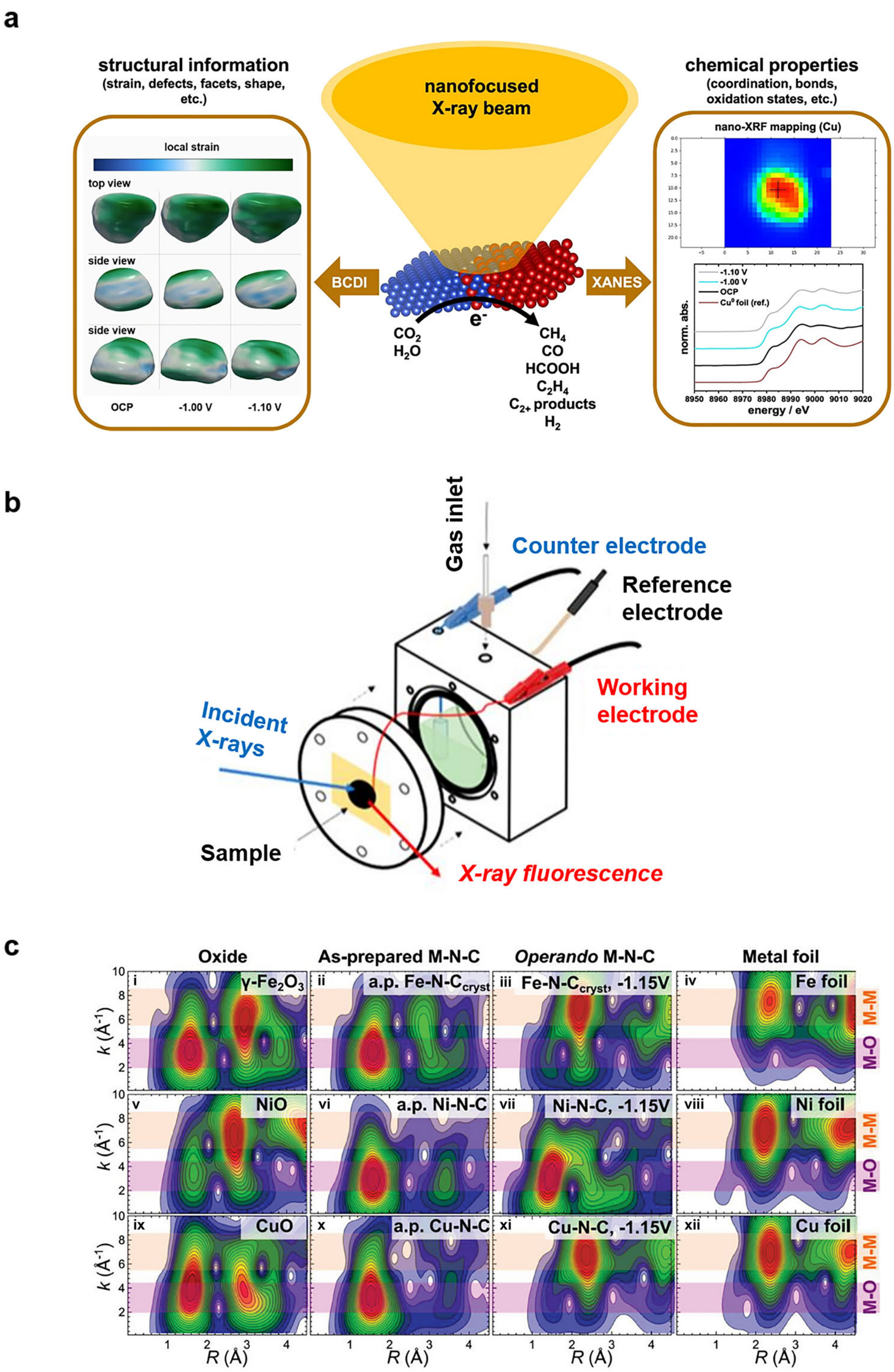

Figure 17. a) The nano-focused X-ray to identify active sites in Cu–Ag catalysts for exploring structure-reactivity relations during eCO_2RR by BCDI and XANES. OCP: open circuit potential. Reproduced with permission from[116] under the terms of the Creative Commons CC BY license. b) The schematic of the in situ electrochemical XAS cell. Reproduced with permission from[117] under the terms of the CC-BY 4.0 license. c) The short-time EXAFS for M—N—C and reference materials: i–iv) Fe K-edge EXAFS for Fe—N—C and reference Fe_2O_3, Fe foil samples; v–viii) Ni K-edge EXAFS for Ni—N—C and reference NiO, Ni foil samples; ix–xii) Cu K-edge EXAFS for Cu—N—C and reference NiO, Ni foil samples. c,g,k) M—N—C samples measured at −1.15 V versus RHE. Reproduced with permission from[118] under the terms of the Creative Commons CC-BY-NC license.

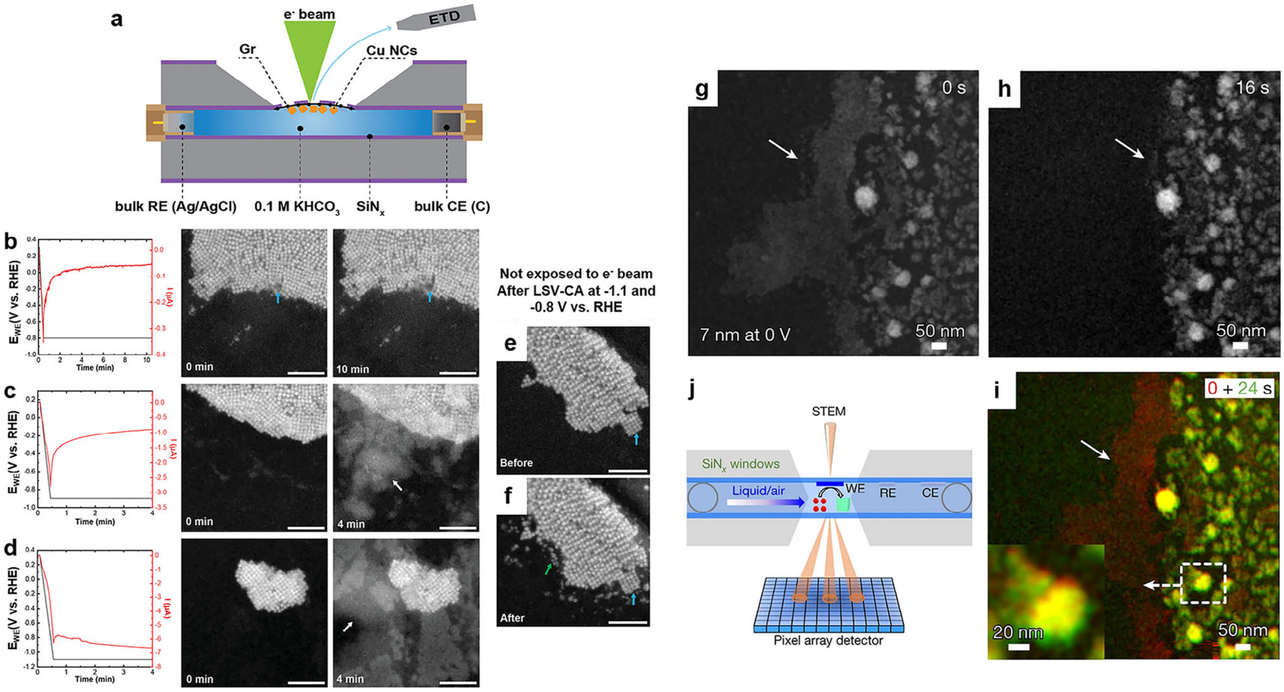

Figure 18. a) The cross-sectional schematic of LPEM with Cu NCs inside the SEM chamber, Everhart–Thornley detector (ETD) is used for imaging. b) The linear sweep voltammetry (LSV) at −0.8 V versus RHE with the LPEM images at 0 and 10 min. c) The LSV at −0.9 V versus RHE with the LPEM images at 0 and 4 min. d) The LSV at −1.1 V versus RHE with the LPEM images at 0 and 4 min. The blue arrows indicate the degraded Cu NC particles. The white arrows are the regions of graphene degradation after LSV-chronoamperometry (CA) at −0.9 and −1.1 V versus RHE. The LPEM images of (e) before and (f) after LSV-CA at −1.1 and −0.8 V vs RHE of a spot that was not exposed to the electron beam. Scale bar: 400 nm. Reproduced with permission from[119] under the terms of the Creative Commons CC BY license. The morphological evolution of 7 nm NPs in in situ STEM at 0 V versus RHE at (g) 0s, h) 16s, and i) 24s. j) The cross-sectional schematic of operando STEM for simultaneously tracking structural and morphological changes under eCO$_2$RR measurements. Reproduced with permission from.[120] Copyright 2023, Yao Yang et al., under exclusive license to Springer Nature Limited.

environment.[116] Hursán et al. utilized a custom-made X-ray absorption spectroscopy (XAS) in situ cell (Figure 17b)[117] to conduct the fine structure studies of catalyst materials during eCO$_2$RR. The cell is designed to accommodate the WE, RE, CE, electrolytes, gas inlets, and incident X-rays. Catalyst samples are sprayed on carbon paper as a WE. After being sealed with a KAPTON window, the carbon paper serves as a window for the incoming X-rays and the X-ray fluorescence. Taking EXAFS as an example, Figure 17c depicts the EXAFS of the as-prepared (a.p.) metal–N—C (M—N—C) catalysts Fe/Ni/Cu—N—C, the Fe/Ni/Cu—N—C at −1.15 V versus RHE, and the reference samples. It is obvious that after being applied with external potential, the metal–O (M—O) bonds in M—N—C transform into metal–metal (M—M) bonds, suggesting the metallization for SACs during eCO$_2$RR.[118]

4.3. In Situ Electron Microscopy for Visualizing the Electrolysis Evolution

CO$_2$RR and HER are usually conducted in liquid-involved electrolyzers. For the characterizations that do not require high vacuum conditions (e.g., hard X-ray involved XANES and EXAFS), the operational in situ cell design mainly demands an interactive window for the X-ray to interact with the target catalyst material. In other cases where vacuum conditions are required (e.g., SEM and transmission electron microscopy, TEM), a robust gas-tight in situ cell is inevitable. Herein, the rational in situ cell design that assures the interaction of the beam with the target material and the gas-tight liquid reactor helps the monitoring of the morphology evolution of the catalyst during the electrolysis. Under these circumstances, liquid phase electron microscopy (LPEM) cells are developed.[119] As depicted in **Figure 18a**, a typical LPEM consists of a pair of Si-based chips coated with a thin SiN$_x$/Gr membrane layer that is liquid/gas impermeable. This configuration allows the operation under high-vacuum conditions for electron microscopes. To adapt the microelectromechanical system, the top chip is patterned with WE (where the imaging/spectroscopy of the samples is performed), CE, and RE. Between the top and bottom chips, microchannels allow the filling of liquid electrolytes and are patterned on the bottom chip. Toleukhanova et al. optimized this in situ LPEM cell design by applying a tri-layer graphene membrane on the chip and successfully monitored the degradation of Cu catalysts during eCO$_2$RR.[119] At the applied potential of −0.8 V vs RHE, it is apparent that the Cu nano cube (Cu NC) undergoes the process of dissolution and redeposition (Figure 18b). However, when the applied potential increases, the tri-layer graphene membrane tends to degrade after a short period (2 and 1 min 30 s for −0.9 V vs RHE and −1.1 V vs RHE, respectively, (Figure 18c,d). To avoid this degradation effect, it is best to perform the test within the stable time window of the graphene membrane or to switch to an electron beam not exposed spot (Figure 18e,f).

Yang et al. designed an operando electrochemical scanning TEM (EC-STEM) cell that encapsulates a three-electrode configuration in a liquid pocket, with Pt and Cu NPs deposited on the carbon serving as CE and WE, respectively, and a Pt pseudo-reference electrode, as depicted in Figure 18j. This operando EC-STEM cell demonstrated consistent electrochemical behavior of Cu NPs compared to that observed in a standard H-cell setup. Typically, an EC-STEM cell has a liquid thickness of 500 nm or greater, which limits the resolution of nanoparticles smaller than 10 nm. By adopting a thin liquid strategy (≈100 nm thickness), the EC-STEM cell successfully resolved the structural evolution of a 7 nm Cu NP. Figure 18g–i illustrates the structural transformation of the 7 nm Cu NP after the LSV scan during eCO_2RR, capturing rapid changes over a time span of 0 to 24 s, including the formation of new Cu nanograins and particles. The inset in Figure 18i further highlights the growth process of these new particles on pre-existing Cu nanograins.[120] Furthermore, stabilizing catalysts in their metastable states with high spatial resolution is essential to understanding the catalytic mechanisms and the evolution of catalyst structures during catalysis. Recent advances in cryogenic electron microscopy (cryo-EM) spectroscopy and imaging have been developed to meet this need.[121]

In addition to SEM and TEM approaches, Lu et al. introduced an innovative optical coherence tomography (OCT) platform to visualize CO_2RR within a CO_2RR electrolyzer.[122] This OCT platform enables the real-time capture of 3D videos and images at high temporal and spatial resolutions, allowing the monitoring of dynamic movements of reactants, intermediates, and products on the cathode and membrane during eCO_2RR. Using this method, they revealed a clear link between CO production and regions of the electrolyzer, specifically membranes and catalyst layers, where CO_2 directly contacts the system.[122]

While in situ characterizations confirm the evolutions of catalysts during cell operation experimentally, density functional theory (DFT) calculation helps demystify the underlying mechanism for it theoretically. For example, oxide-derived Cu promotes C—C coupling in eCO_2RR, but it reconstructs during the reaction. Lian et al. employed DFT to investigate the reduction procedure of oxide-derived Cu through dynamics of large-scale molecular systems with accurate neural network potentials trained on introducing experimental conditions and first-principles data during ECO_2RR.[123] They found out that, under long-term operation, oxide-derived Cu would be completely reduced to Cu, providing a highly reconstructed surface of Cu catalyst to adsorb oxygen atoms. However, these surface-adsorbed oxygen atoms are not stable in conventional experimental situations, which brings thoughts to the relations between oxide-derived Cu evolution and oxygen residues during ECO_2RR.

4.4. Insights from Other Electrochemical Cell Devices

The concepts of CO_2RR, HER electrolyzers, and other chemical cell devices share many similarities. They can learn from each other for mutual improvement. For instance, the electrochemical cell designs for CO_2RR and HER usually get inspiration from fuel cell devices. Thus, discoveries in other electrochemical cell devices are likely to be transplanted to CO_2RR and HER. Here are some advanced electrochemical device designs that might inspire the next-generation CO_2RR and HER electrolyzer developments.

4.4.1. The Redox Flow Concept from the Aqueous Flow Battery

Battery cell designs can also provide some inspiration for CO_2RR and HER electrolyzers. For example, Xi et al. established an aqueous redox flow battery (ARFB) to realize pH-decoupling, which exceeds the thermodynamic water splitting potential window of 1.23 V. The mildly alkaline and mildly acidic electrolytes were employed to mitigate the crossover and allowed a high round-trip efficiency with the OCP larger than 1.7 V. An acid-based regeneration system was also implemented to restore the electrolytes to their initial pH value periodically. The ARFB system afforded a capacity fade rate of less than 0.07% per day, a round-trip EE larger than 85% (maintaining a Coulombic efficiency of 99% for over 1 week, **Figure 19**a).[124] Sodium and chloride ions are the major charge carriers in this battery cell design (Figure 19b). This pH-decoupling strategy demonstrates the ability to improve the life span of the electrolyzer with high EE, which can be practical for CO_2RR and HER electrolyzers.

4.4.2. Solar Energy Utilization of Photoelectrochemical Devices

Other than the sole electricity-powered electrolyzer, photoelectrochemical (PEC) cells that utilize both solar and electricity can integrate the CO_2RR and HER electrolysis with the green energy concept better.[125] Balog et al. employed PEC methods with concentrated sunlight to achieve current densities close to those of electrochemical cells but with lower energy input. **Figure 20**a,b depicts the detailed configuration of the PEC cell. Combining the PEC oxidation of glycerol and HER/CO_2RR in a MEA flow cell, the authors realized a photocurrent density over 110 mA cm^{-2} (Figure 20c), which is an order of magnitude larger than those reported for the conventional photocatalytic systems (Figure 20d).[126]

4.4.3. In Situ Cell Structure Designs from PEM Fuel Cell

The same thing goes for in situ characterization cell designs. For example, Ronovský designed a single PEM fuel cell for the in situ depth-sensitive high-resolution XAS.[127] **Figure 21**a displays the symmetric PEM fuel cell, where a graphite flow field, a two-part copper body with a KAPTON window, a resin heat shield, and a rubber gasket are embedded, allowing both fluorescence and absorption X-ray measurements. The details of the bottom half of the copper body, the inner body, and the groove design are displayed in Figure 21b–d, respectively. This deliberate design increases the signal-to-noise ratio, allowing the capture of X-ray fluorescence at different emission angles, thus providing depth information. Under the measurement of the actual setup (Figure 21e,f) at ID26 beamline European synchrotron radiation facility (ESRF), the standard high-resolution XAS can be obtained for Ni species in Nafion (Figure 21g). This PEM fuel cell design holds great potential to be adapted into CO_2RR and HER MEA electrolyzers for the XAS measurements.

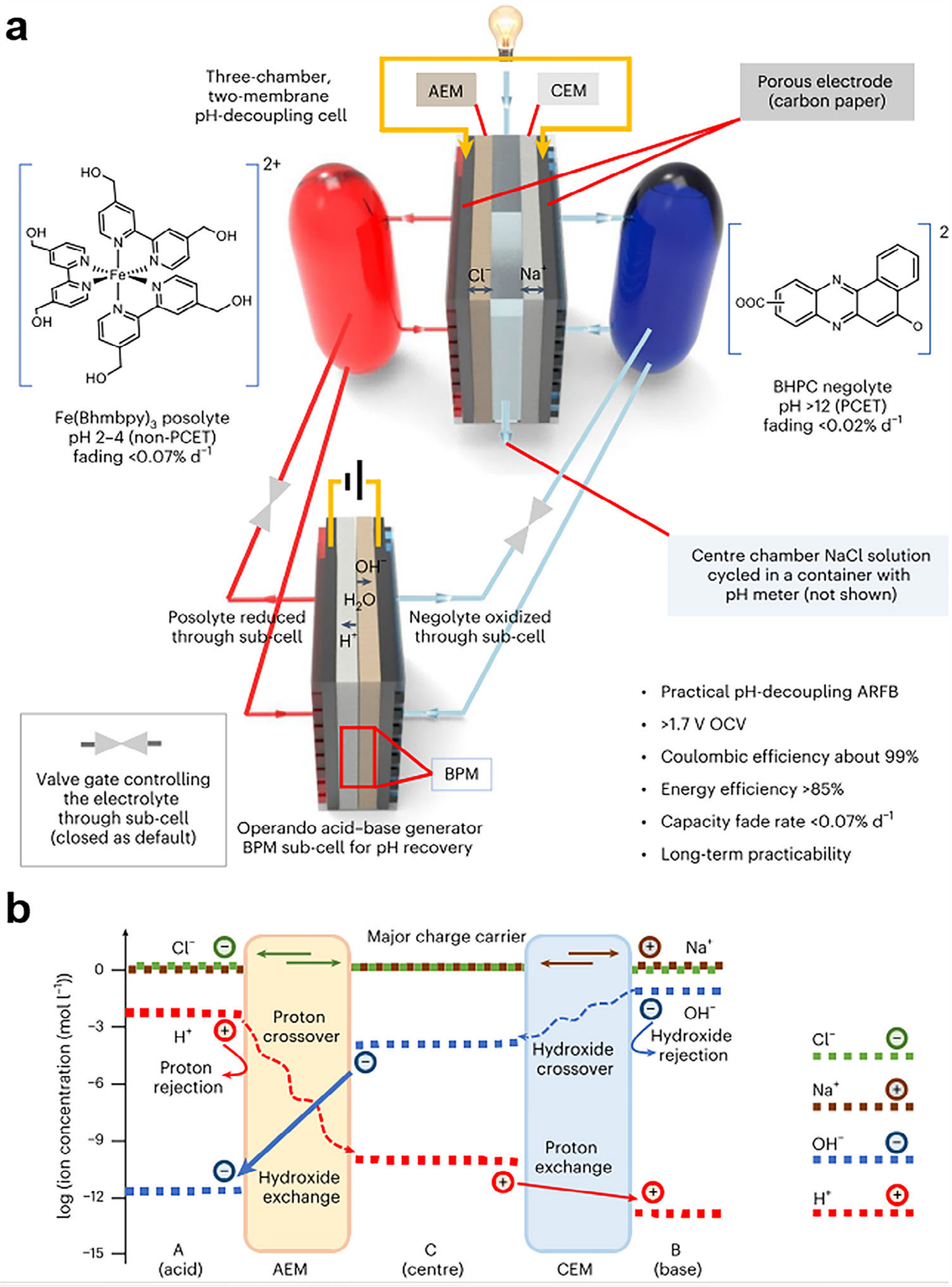

Figure 19. a) The schematic of a three-chamber two-membrane cell with a pH recovery sub-cell. b) Ion concentration and flow across three chambers. Reproduced with permission from.[124] Copyright 2024, Dawei Xi et al., under exclusive license to Springer Nature Limited.

Other than adapting the concepts in cell designs, the relations of HER, CO_2RR, and fuel cells are closely intertwined. The hydrogen produced from water electrolyzers (PEMWE and AEMWE) can supply the fuel cell industry, as H_2 is the most common gas for fuel cells. In addition, the reduction products from CO_2RR electrolyzers can also serve as the power source for fuel cells, such as methanol and formic acid. The integration of CO_2RR, HER, and fuel cell industries holds the possibility to further mitigate carbon emissions and promote a future decarbonized industry. For example, Zhang et al. successfully utilized lattice-distorted bismuth catalysts to produce 2 M formic acid from eCO_2RR (at 200 mA cm^{-2} for 300 h), which could substitute the conventional formic acid production from methyl formate hydrolysis. Importantly, the produced formic acid could directly serve as the power source for the air-breathing formic acid fuel cell, resulting in a 55 mW cm^{-2} power density and a 20.1% thermal efficiency.[128] Promising electrochemical productions can also be integrated into this decarbonized industry. For instance, electrochemical nitrate reduction shows potential for ammonia generation and water treatment. However, the need for high-concentration

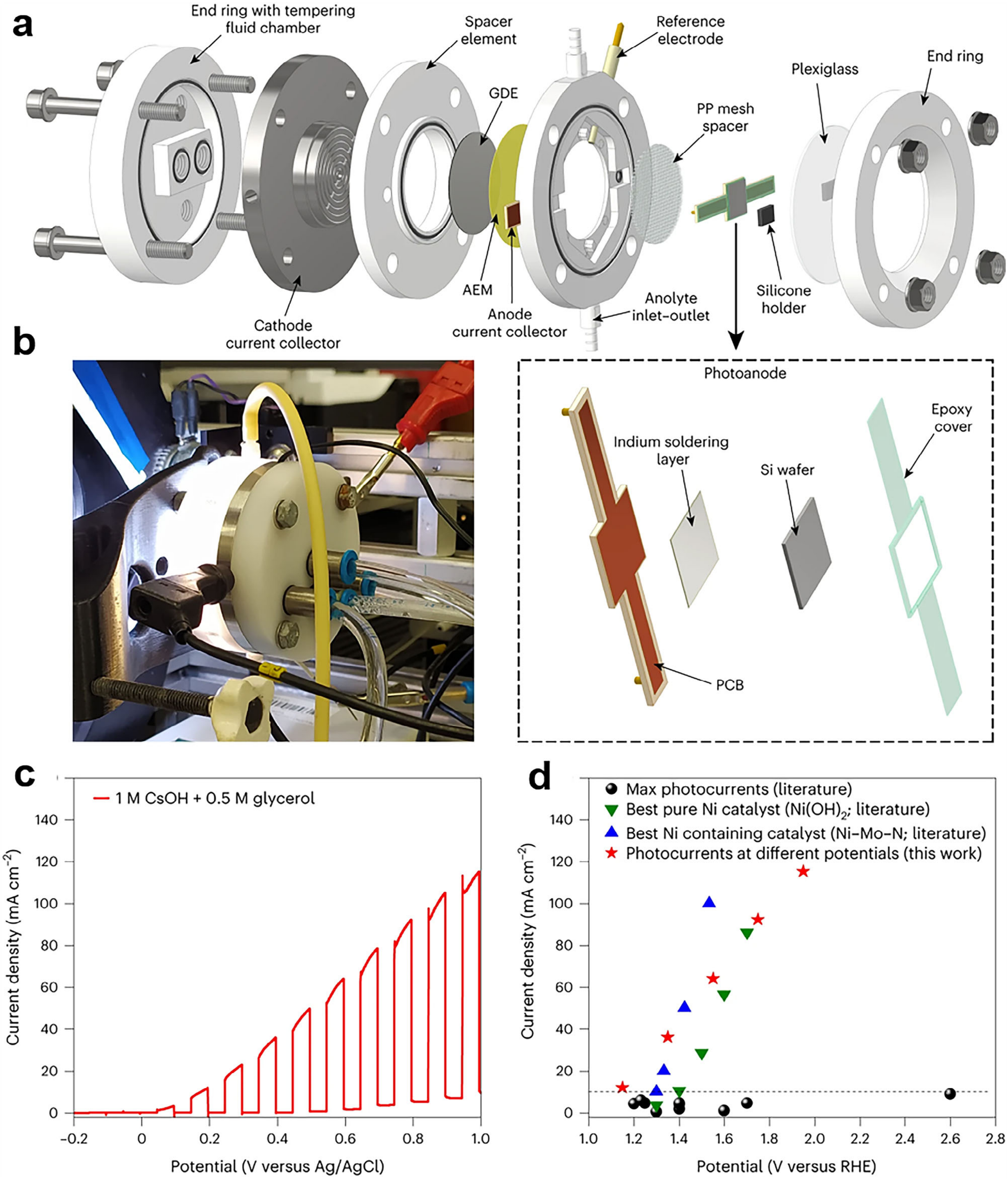

Figure 20. a) The schematic diagram of the PEC cell with the detailed photoanode structure. PCB, printed circuit board; PP, polypropylene. b) A photo of the PEC cell. c) The photovoltammogram of the Ni/Si photoanode. d) The glycerol oxidation photocurrents comparison of[126] (red stars) with the maximum photocurrents from the literature. Reproduced with permission from[126] under the terms of the Creative Commons CC BY license.

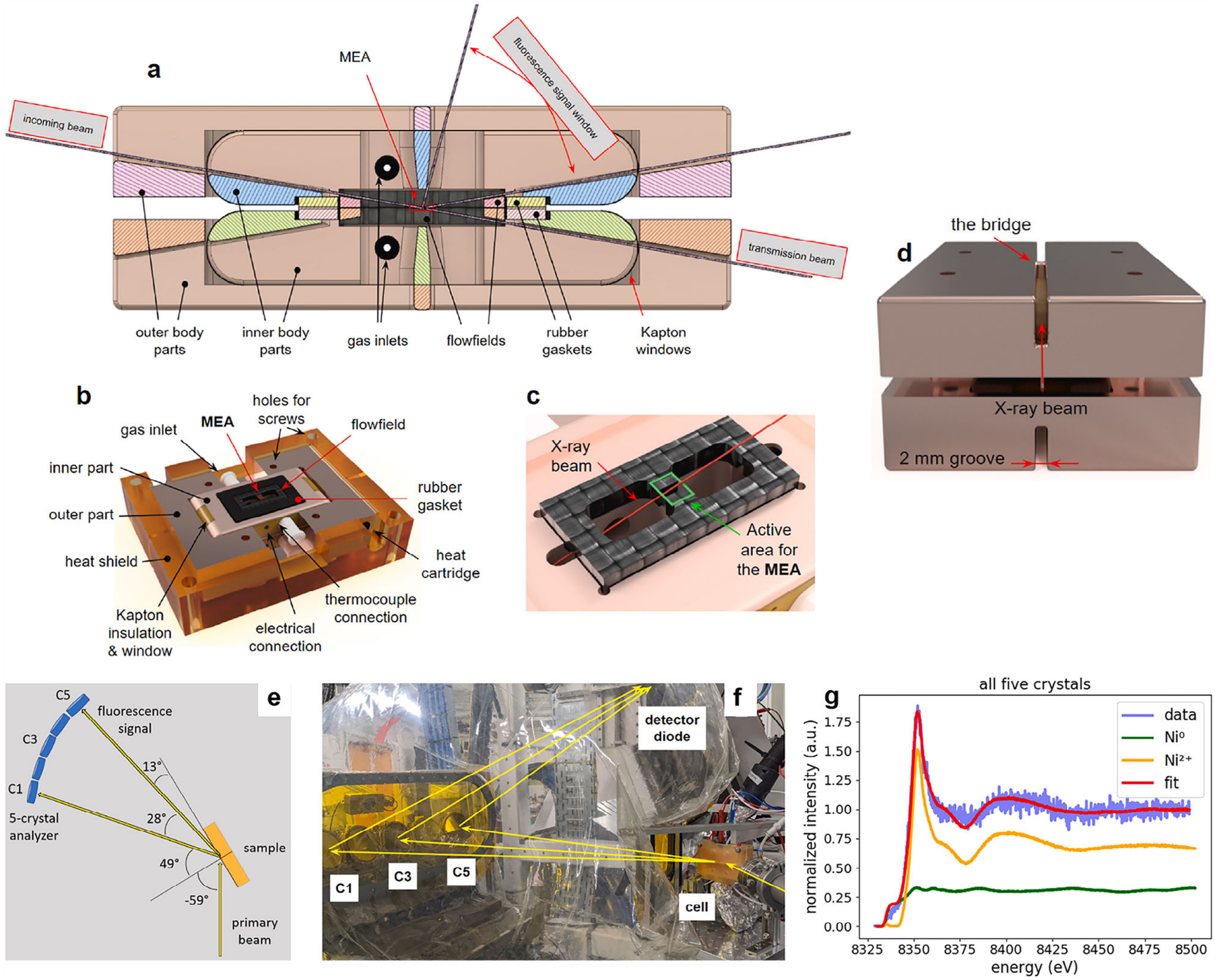

Figure 21. a) A cross-sectional schematic of the PEM fuel cell. b) The schematic illustration of the bottom half of the PEM fuel cell. c) The detailed schematic of the flow field with the active MEA area composed of two adjacent lands (in green) and one (1 × 2) mm channel. d) The schematic illustration along the beam path on the PEM fuel cell with a 2 mm groove in the middle for X-ray emission. e) The schematic illustration of the experimental setup with the hard X-ray emission spectrometer using five analyzer crystals (highlighted C1, C3, and C5), with the respective geometry. f) The photo of the actual setup at the ID26 beamline ESRF. g) The XANES of ionic Ni^{2+} in Nafion (0.1 м $NiSO_4$ solution pipetted on the Nafion membrane, orange), fitted (red), metallic nickel Ni_0 (Ni foil, green), and Ni K-alpha edge spectrum (blue). Reproduced with permission from.[127] Copyright 2023, Elsevier B.V.

electrolytes in the electrochemical nitrate reduction system presents a challenge. To address this, Chen et al. introduced wastewater to the middle of the porous solid electrolyte, coupling the cation shielding effect with a three-chamber porous solid electrolyte reactor. This approach enabled nitrate reduction without electrolytes, achieving ammonia FE of over 90% at current densities exceeding 100 mA cm^{-2}, under a 2000 ppm nitrate concentration in the wastewater.[129]

5. Summary, Challenges, and Perspectives

5.1. Summary

This review systematically summarizes recent advancements in CO_2RR and water electrolyzer cell designs, covering various strategies. The main issues of CO_2RR flow cell devices include unsatisfactory catalytic performance, salt precipitation, carbonate crossover, high solution resistance, and electrode wetting. This review highlights some solutions, such as optimizing flow pattern in the flow cell to improve mass transport for better performance; designing acidic and neutral electrolyte CO_2RR electrolyzer cell designs to mitigate salt precipitation and carbonation effects; using AEM, PEM, and BPM in MEA electrolyzers to facilitate CO_2RR by excluding the catholyte and controlling the ion diffusion; constructing hydrophobic GDE to enhance the catalytic performance at the three-phase boundary; employing a cascade electrolyzer strategy to produce long-chain carbon products; and utilizing liquid-fed BCE with rationalized counter-reactions for high EE during eCO_2RR. Water electrolyzers face challenges such as high costs, safety issues, stability issues, and unsatisfactory EE. This review summarizes advanced PEM and AEM water electrolyzers for water electrolysis; optimization of BP and flow patterns for cost-effective PEMWE with enhanced performance; development of novel ISMs for the HER under extreme operation conditions with improved stability; floating electrode cell designs to maximize the HER performance; high-temperature SOEC designs for industrial-scale applications with improved efficiency.

Additionally, the review discusses state-of-the-art in situ characterization techniques (e.g., FTIR, XAS, and EM) and highlights the importance of rational in situ cell designs for accurate measurements. The review also addresses electrochemical cell designs from fuel cells, batteries, and photoelectrochemical reactions, offering new insights into CO_2RR and water electrolyzer development.

Some industrial pilot projects have demonstrated the scalability of CO_2RR and water electrolysis. For example, during the NRG COSIA Carbon XPRIZE competition, the CERT team scaled up their system to achieve over 10 000 times the performance of a laboratory electrolyzer, with over 50% of CO_2 converted in a single pass. This system was deployed at a natural gas power plant in Alberta, Canada, operating robustly for over 1400 consecutive hours without the need for ultra-pure CO_2. Notably, each ton of ethylene produced using the CERT process sequesters over 3 tons of CO_2, making it the first electrochemical production of ethylene from an industrial CO_2 source.[130] Additionally, Air Liquide inaugurated the world's largest membrane electrolyzer (20 MW PEM electrolyzer) in January 2021 in Bécancour, Quebec, Canada. Powered by 99% renewable energy from Hydro-Québec, this unit produces over 8.2 metric tons of green H_2 per day, which prevents nearly 27 000 metric tons of CO_2 emissions annually compared to the traditional H_2 production process.[131] Despite these advancements, industrial challenges remain, especially regarding scalability and cost.

5.2. Industrial Challenges

1) **Large-scale industrializations:** Most laboratory-scale eCO_2RR experiments have been conducted on small cells (a few cm^2) for short durations (tens to hundreds of hours). While some studies report durability over thousands of hours, their current densities remain low, far from the standards required for industrial applications.[132]
2) **Industrial CO_2 supply:** Pure CO_2 is generally required for eCO_2RR, as the presence of oxidizing gases such as O_2, NO_x, or SO_x can inhibit CO_2RR. Some studies have explored CO_2RR using flue gas, but these are still at the laboratory scale. Efficient integration of CO_2 capture and eCO_2RR is essential for industrial-scale deployment.
3) **Engineering challenges at larger scales:** In MEA-based electrolysis, the heat generated at high current densities is often difficult to dissipate efficiently, leading to decreased catalytic activity and membrane degradation. Although switching from OER to HOR can reduce overall energy consumption, this approach still depends on a green hydrogen supply, which remains impractical at large scales. Besides, water accumulation within the GDE at high current densities causes flooding, which degrades overall performance. Addressing this issue requires optimizations of the flow channel, GDE, and membrane designs to effectively manage or remove excess water during operation.[133]
4) **Use of noble and rare metals:** Long-term operation of electrolyzers often relies on precious and rare metals, creating a significant bottleneck for the industrial application of both CO_2RR and water electrolysis.
5) **Cost issues:** Capital cost remains a major consideration for plant applications. The cost of power supply, particularly renewable electricity, plays a significant role in the overall plant economics. Cost reduction strategies should be applied to electrolyzer components (e.g., BP, membranes, cell assemblies, and noble metal catalysts) while ensuring reliability, efficiency, and longevity.[103]

5.3. Perspectives

1) **Electrolyte and catalyst regeneration via external flow pulses:** As discussed in this review, the regeneration of the electrolyte and catalyst by external flow pulse is possible. Moreover, the potential pulse controlled by the electrochemical workstation can also reactivate the catalysts, offering a viable method for reactivating catalysts and enabling long-term electrolyzer operation.[134]
2) **Powder catalysts on GDLs:** Powder catalysts are typically applied to GDLs using catalyst inks. Research into ink composition, such as the ratio of catalyst to binder (e.g., Nafion or PTFE) and variations in the equivalent weight of binders, could provide valuable insights to enhance catalytic performance. Peter Strasser's group has extensively investigated catalyst ink preparation and MEA fabrication.[135] Optimizing catalyst loading and binder selection is crucial for improving overall system performance, stability, and scalability.
3) **Integration of HER, CO_2RR, and other electrolyzers:** Integrating HER, CO_2RR, and other electrolyzers could enable the production of long-chain carbon chemicals. For instance, expanding CO_2RR cascade reactions to fabricate more complex chemicals such as glycine could create significant market opportunities in future industrial applications.[136] Besides, with the proper coupling of counter-reactions, membrane-free electrolyzers can be proposed to reduce the electricity consumption in a large-scale system.[137]
4) **Advancements in characterization techniques:** Advanced in situ X-ray–based characterization techniques are not always accessible, making it difficult to investigate reaction mechanisms. Therefore, developing more affordable and accessible techniques is essential. For example, rotating disk electrodes and rotating ring-disk electrodes could detect reduction products during CO_2RR, offering another approach to studying catalytic mechanisms.[138]
5) **Membrane and electrolyte innovations:** The economic implications of electrolyte selection are significant.[139] Currently, PEMs are the most commonly used in MEAs. However, alternatives like BPMs and AEMs are less commercially mature.[140] The development of membranes tailored to specific reaction conditions is therefore essential.[141] For instance, a watermelon skin-shaped membrane has demonstrated high ion conductivity (282.3 mS cm^{-1} in 1 M KOH electrolyte at room temperature), offering promising performance advantages.[142] Additionally, membranes capable of operating under high temperatures could further enhance

electrolyzer performance under extreme conditions.[53] Composite membranes offer multifunctional improvements.[143] For example, the formation of through-plane conducting pathways induced by a magnetic field in AEMs significantly enhances hydroxide ion transport efficiency between electrodes, leading to improved power output.[144] Furthermore, self-healing membranes represent an innovative route to enhance membrane durability. Membranes such as poly(vinyl alcohol) and graphene oxide-modified Nafion membranes have demonstrated the ability to heal micrometer-scale mechanical damage while maintaining intrinsic ion conductivity, thereby strengthening mechanical properties and prolonging operational stability.[145]

6) **Large-scale stack constructions (e.g., SOEC) for industrialization:** The commercialization of SOEC stacks for H_2 production has already been achieved, paving the way for the CO_2RR industry to follow suit. Large-scale production of H_2 and CO from SOECs could serve as the foundation for downstream chemical production, creating a promising pathway for CO_2RR to enter the industrial market and unlock economic incentives. As for the power supply, the stack of seawater–freshwater osmotic energy cells has been proven to successfully direct the H_2 production from water electrolysis, which provides another pathway to the renewable energy input for industrialization.[146]

Acknowledgements

This work was supported financially by the Natural Sciences and Engineering Research Council of Canada (NSERC), the NRCan project (Project Code: A1-022527), the Fonds de Recherche du Québec-Nature et Technologies (FRQNT), the Centre Québécois sur les Materiaux Fonctionnels (CQMF, https://doi.org/10.69777/341666), the Institut National de la Recherche Scientifique (INRS), and the École de Technologie Supérieure (ÉTS). G.Z. thanks for the support from the Marcelle-Gauvreau Engineering Research Chair program, and the Canada Research Chair Programs.

Conflict of Interest

The authors declare no conflict of interest.

Keywords

CO_2 reduction, electrochemical cell design, electrolyzers, hydrogen evolution, in situ characterizations

Received: March 18, 2025
Revised: April 28, 2025
Published online:

[1] Q. Yang, H. Liu, Y. Lin, D. Su, Y. Tang, L. Chen, *Adv. Mater.* **2024**, *36*, 2310912.
[2] S. Fankhauser, S. M. Smith, M. Allen, K. Axelsson, T. Hale, C. Hepburn, J. M. Kendall, R. Khosla, J. Lezaun, E. Mitchell-Larson, M. Obersteiner, L. Rajamani, R. Rickaby, N. Seddon, T. Wetzer, *Nat. Clim. Change* **2021**, *12*, 15.
[3] F. P. Pan, X. X. Yang, T. O'Carroll, H. Y. Li, K. J. Chen, G. Wu, *Adv. Energy Mater.* **2022**, *12*, 2200586.
[4] H. Li, M. E. Zick, T. Trisukhon, M. Signorile, X. Liu, H. Eastmond, S. Sharma, T. L. Spreng, J. Taylor, J. W. Gittins, C. Farrow, S. A. Lim, V. Crocellà, P. J. Milner, A. C. Forse, *Nature* **2024**, *630*, 654.
[5] Y. Chen, J. Zhang, L. Yang, X. Wang, Q. Wu, Z. Hu, *Electrochem. Energy Rev.* **2022**, *5*, 11.
[6] C. Wang, Z. Lv, X. Feng, W. Yang, B. Wang, *Adv. Energy Mater.* **2024**, *14*, 2400160.
[7] Z. S. Chen, G. X. Zhang, J. Prakash, Y. Zheng, S. H. Sun, *Adv. Energy Mater.* **2019**, *9*, 1900889.
[8] Z. S. Chen, G. X. Zhang, H. R. Chen, J. Prakash, Y. Zheng, S. H. Sun, *Renewable Sustainable Energy Rev.* **2022**, *155*, 111922.
[9] X. Zou, Y. Zhang, *Chem. Soc. Rev.* **2015**, *44*, 5148.
[10] H. Kouchaki-Penchah, O. Bahn, H. Bashiri, S. Bedard, E. Bernier, T. Elliot, A. Hammache, K. Vaillancourt, A. Levasseur, *Int. J. Hydrogen Energy* **2024**, *49*, 173.
[11] D. Pivetta, C. Dall'Armi, P. Sandrin, M. Bogar, R. Taccani, *Renewable Sustainable Energy Rev.* **2024**, *189*, 113912.
[12] Z. Pu, I. S. Amiinu, R. Cheng, P. Wang, C. Zhang, S. Mu, W. Zhao, F. Su, G. Zhang, S. Liao, S. Sun, *Nano-Micro Lett.* **2020**, *12*, 21
[13] A. S. Emam, M. O. Hamdan, B. A. Abu-Nabah, E. Elnajjar, *Int. J. Hydrogen Energy* **2024**, *64*, 599.
[14] M. Filippi, T. Möller, L. Liang, P. Strasser, *Energy Environ. Sci.* **2023**, *16*, 5265.
[15] a) L. Ge, H. Rabiee, M. R. Li, S. Subramanian, Y. Zheng, J. H. Lee, T. Burdyny, H. Wang, *Chem* **2022**, *8*, 663; b) D. Ma, T. Jin, K. Y. Xie, H. T. Huang, *J. Mater. Chem. A* **2021**, *9*, 20897; c) S. Y. Liang, N. Altaf, L. Huang, Y. S. Gao, Q. Wang, *J. CO2 Util.* **2020**, *35*, 90; d) X. She, Y. Wang, H. Xu, S. C. E. Tsang, S. P. Lau, *Angew. Chem., Int. Ed. Engl.* **2022**, *61*, 202211396.
[16] A. Bodard, Z. Chen, O. ELJarray, G. Zhang, *Small Methods* **2024**, *8*, 2400574.
[17] F. Chang, M. Xiao, R. Miao, Y. Liu, M. Ren, Z. Jia, D. Han, Y. Yuan, Z. Bai, L. Yang, *Electrochem. Energy Rev.* **2022**, *5*, 4.
[18] a) Z. Chen, G. Zhang, L. Du, Y. Zheng, L. Sun, S. Sun, *Small* **2020**, *16*, 2004158; b) Z. Chen, G. Zhang, Y. Wen, N. Chen, W. Chen, T. Regier, J. Dynes, Y. Zheng, S. Sun, *Nano-Micro Lett.* **2021**, *14*, 25; c) J. Ding, H. Bin Yang, X.-L. Ma, S. Liu, W. Liu, Q. Mao, Y. Huang, J. Li, T. Zhang, B. Liu, *Nat. Energy* **2023**, *8*, 1386; d) N. M. Adli, W. Shan, S. Hwang, W. Samarakoon, S. Karakalos, Y. Li, D. A. Cullen, D. Su, Z. Feng, G. Wang, G. Wu, *Angew. Chem., Int. Ed. Engl.* **2021**, *60*, 1022.
[19] a) C.-T. Dinh, T. Burdyny, M. G. Kibria, A. Seifitokaldani, C. M. Gabardo, F. P. García de Arquer, A. Kiani, J. P. Edwards, P. De Luna, O. S. Bushuyev, C. Zou, R. Quintero-Bermudez, Y. Pang, D. Sinton, E. H. Sargent, *Science* **2018**, *360*, 783; b) W. Ju, F. Jiang, H. Ma, Z. Pan, Y.-B. Zhao, F. Pagani, D. Rentsch, J. Wang, C. Battaglia, *Adv. Energy Mater.* **2019**, *9*, 1901514; c) R. Du, Q. Wu, S. Zhang, P. Wang, Z. Li, Y. Qiu, K. Yan, G. I. N. Waterhouse, P. Wang, J. Li, Y. Zhao, W.-W. Zhao, X. Wang, G. Chen, *Small* **2023**, *19*, 2301289; d) G. X. Zhang, X. H. Yang, M. Dubois, M. Herraiz, R. Chenitz, M. Lefèvre, M. Cherif, F. Vidal, V. P. Glibin, S. Sun, J.-P. Dodelet, *Energy Environ. Sci.* **2019**, *12*, 3015; e) J. Zhao, H. Liu, X. Li, *Electrochem. Energy Rev.* **2023**, *6*, 13.
[20] a) X. Wang, Q. Hu, G. Li, H. Yang, C. He, *Electrochem. Energy Rev.* **2022**, *5*, 28; b) X. Yu, Y. Xu, L. Li, M. Zhang, W. Qin, F. Che, M. Zhong, *Nat. Commun.* **2024**, *15*, 1711; c) D. Zhou, C. Chen, Y. Zhang, M. Wang, S. Han, X. Dong, T. Yao, S. Jia, M. He, H. Wu, B. Han, *Angew. Chem., Int. Ed. Engl.* **2024**, *63*, 202400439; d) G. F. Wu, C. Zhu, J. N. Mao, G. Li, S. Li, X. Dong, A. Chen, Y. Song, G. Feng, X. Liu, Y. Wei, J. Wang, W. Wei, W. Chen, *ACS Energy Lett.* **2023**, *8*, 4867.
[21] B. Jung, S. Park, C. Lim, W. H. Lee, Y. Lim, J. Na, C.-J. Lee, H.-S. Oh, U. Lee, *Chem. Eng. J.* **2021**, *424*, 130265.

[22] P. V. Suresh, S. Jayanti, A. P. Deshpande, P. Haridoss, *Int. J. Hydrogen Energy* **2011**, *36*, 6067.
[23] C. Xu, T. S. Zhao, *Electrochem. Commun.* **2007**, *9*, 497.
[24] F. P. G. de Arquer, C.-T. Dinh, A. Ozden, J. Wicks, C. McCallum, A. R. Kirmani, D.-H. Nam, C. Gabardo, A. Seifitokaldani, X. Wang, Y. C. Li, F. Li, J. Edwards, L. J. Richter, S. J. Thorpe, D. Sinton, E. H. Sargent, *Science* **2020**, *367*, 661.
[25] B. Endrodi, E. Kecsenovity, A. Samu, F. Darvas, R. V. Jones, V. Török, A. Danyi, C. Janáky, *ACS Energy Lett.* **2019**, *4*, 1770.
[26] a) R. Subbaraman, D. Tripkovic, D. Strmcnik, K.-C. Chang, M. Uchimura, A. P. Paulikas, V. Stamenkovic, N. M. Markovic, *Science* **2011**, *334*, 1256; b) A. Ali, F. Long, P. K. Shen, *Electrochem. Energy Rev.* **2022**, *5*, 1.
[27] Z. Zhang, L. Melo, R. P. Jansonius, F. Habibzadeh, E. R. Grant, C. P. Berlinguette, *ACS Energy Lett.* **2020**, *5*, 3101.
[28] a) M. E. Leonard, L. E. Clarke, A. Forner-Cuenca, S. M. Brown, F. R. Brushett, *ChemSusChem* **2020**, *13*, 400; b) A. S. Hall, *Nat. Catal.* **2023**, *6*, 744.
[29] J. Feng, L. Zhang, S. Liu, L. Xu, X. Ma, X. Tan, L. Wu, Q. Qian, T. Wu, J. Zhang, X. Sun, B. Han, *Nat. Commun.* **2023**, *14*, 4615.
[30] J. A. Gauthier, Z. Lin, M. Head-Gordon, A. T. Bell, *ACS Energy Lett.* **2022**, *7*, 1679.
[31] a) C. Ye, F. Dattila, X. Chen, N. Lopez, M. T. M. Koper, *J. Am. Chem. Soc.* **2023**, *145*, 19601; b) X. Yang, H. Ding, S. Li, S. Zheng, J. F. Li, F. Pan, *J. Am. Chem. Soc.* **2024**, *146*, 5532; c) X. Qin, T. Vegge, H. A. Hansen, *J. Am. Chem. Soc.* **2023**, *145*, 1897; d) M. C. O. Monteiro, F. Dattila, B. Hagedoorn, R. García-Muelas, N. López, M. T. M. Koper, *Nat. Catal.* **2021**, *4*, 654.
[32] Z. Zhang, H. Li, Y. Shao, L. Gan, F. Kang, W. Duan, H. A. Hansen, J. Li, *Nat. Commun.* **2024**, *15*, 612.
[33] X. Zhang, J. Li, Y. Y. Li, Y. Jung, Y. Kuang, G. Zhu, Y. Liang, H. Dai, *J. Am. Chem. Soc.* **2021**, *143*, 3245.
[34] B. Endrodi, A. Samu, E. Kecsenovity, T. Halmagyi, D. Sebok, C. Janaky, *Nat. Energy* **2021**, *6*, 439.
[35] W. Wu, L. Xu, Q. Lu, J. Sun, Z. Xu, C. Song, J. C. Yu, Y. Wang, *Adv. Mater.* **2024**, *37*, 2312894.
[36] J. E. Huang, F. Li, A. Ozden, A. S. Rasouli, F. P. G. de Arquer, S. Liu, S. Zhang, M. Luo, X. Wang, Y. Lum, Y. Xu, K. Bertens, R. K. Miao, C.-T. Dinh, D. Sinton, E. H. Sargent, *Science* **2021**, *372*, 1074.
[37] L. P. Chi, Z. Z. Niu, Y. C. Zhang, X.-L. Zhang, J. Liao, Z.-Z. Wu, P.-C. Yu, M.-H. Fan, K.-B. Tang, M.-R. Gao, *Proc. Natl. Acad. Sci. U. S. A.* **2023**, *120*, 2312876120.
[38] M. Wang, B. Wang, J. Zhang, S. Xi, N. Ling, Z. Mi, Q. Yang, M. Zhang, W. R. Leow, J. Zhang, Y. Lum, *Nat. Commun.* **2024**, *15*, 1218.
[39] Z. Zhang, X. Huang, Z. Chen, J. Zhu, B. Endrodi, C. Janáky, D. Deng, *Angew. Chem., Int. Ed. Engl.* **2023**, *62*, 202302789.
[40] J. Gu, C. S. Hsu, L. Bai, H. M. Chen, X. Hu, *Science* **2019**, *364*, 1091.
[41] Z. Li, Z. Zhu, J. Wang, Y. Lin, W. Li, Y. Chen, X. Niu, X. Qi, J. Wang, J. S. Chen, R. Wu, *Adv. Funct. Mater.* **2024**, *34*, 2410552.
[42] Z. Yin, H. Peng, X. Wei, H. Zhou, J. Gong, M. Huai, L. Xiao, G. Wang, J. Lub, L. Zhuang, *Energy Environ. Sci.* **2019**, *12*, 2455.
[43] E. Vichou, Y. Adjez, Y. Li, M. Gomez-Mingot, M. Fontecave, C. M. Sanchez-Sanchez, *J. Am. Chem. Soc.* **2024**, *146*, 2824.
[44] M. Sun, J. Cheng, M. Yamauchi, *Nat. Commun.* **2024**, *15*, 491.
[45] J. Zeng, M. Fontana, A. Sacco, D. Sassone, C. F. Pirri, *Catal. Today* **2022**, *397*, 463.
[46] Y. Shi, B. Zhang, *Chem. Soc. Rev.* **2016**, *45*, 1529.
[47] Y. Chen, J. A. Wrubel, A. E. Vise, F. Intia, S. Harshberger, E. Klein, W. A. Smith, Z. Ma, T. G. Deutsch, K. C. Neyerlin, *Chem Catal.* **2022**, *2*, 400.
[48] J. A. Abarca, G. Díaz-Sainz, I. Merino-Garcia, G. Beobide, J. Albo, A. Irabien, *J. Environ. Chem. Eng.* **2023**, *11*, 109724.
[49] E. Berretti, L. Osmieri, V. Baglio, H. A. Miller, J. Filippi, F. Vizza, M. Santamaria, S. Specchia, C. Santoro, A. Lavacchi, *Electrochem. Energy Rev.* **2023**, *6*, 30.
[50] Q. Meyer, C. J. Yang, Y. Cheng, C. Zhao, *Electrochem. Energy Rev.* **2023**, *6*, 16.
[51] C. Xia, P. Zhu, Q. Jiang, Y. Pan, W. Liang, E. Stavitski, H. N. Alshareef, H. Wang, *Nat. Energy* **2019**, *4*, 776.
[52] E. W. Lees, J. C. Bui, O. Romiluyi, A. T. Bell, A. Z. Weber, *Nat. Chem. Eng.* **2024**, *1*, 340.
[53] C. A. G. Rodriguez, N. C. Kani, A. B. Moss, B. O. Joensen, S. Garg, W. Deng, T. Wilson, J. R. Varcoe, I. Chorkendorff, B. Seger, *EES Catal.* **2024**, *2*, 850.
[54] S. Hu, L. Zhang, H. Liu, W. Li, Z. Cao, L. Cai, Y. Zhu, X. Zhu, W. Yang, *J. Energy Chem.* **2019**, *36*, 87.
[55] Y. Zheng, Z. W. Chen, J. J. Zhang, *Electrochem. Energy Rev.* **2021**, *4*, 508.
[56] a) A. Ozden, Y. Wang, F. Li, M. Luo, J. Sisler, A. Thevenon, A. Rosas-Hernández, T. Burdyny, Y. Lum, H. Yadegari, T. Agapie, J. C. Peters, E. H. Sargent, D. Sinton, *Joule* **2021**, *5*, 706; b) T. Tan, Z. Wang, M. Qin, W. Zhong, J. Hu, C. Yang, M. Liu, *Adv. Funct. Mater.* **2022**, *32*, 2202878; c) H. Lv, L. Lin, X. Zhang, R. Li, Y. Song, H. Matsumoto, N. Ta, C. Zeng, Q. Fu, G. Wang, X. Bao, *Nat. Commun.* **2021**, *12*, 5665; d) H. Lv, L. Lin, X. Zhang, D. Gao, Y. Song, Y. Zhou, Q. Liu, G. Wang, X. Bao, *J. Mater. Chem. A* **2019**, *7*, 11967.
[57] Y. Song, J. Min, Y. Guo, R. Li, G. Zou, M. Li, Y. Zang, W. Feng, X. Yao, T. Liu, X. Zhang, J. Yu, Q. Liu, P. Zhang, R. Yu, X. Cao, J. Zhu, K. Dong, G. Wang, X. Bao, *Angew. Chem., Int. Ed. Engl.* **2024**, *63*, 202313361.
[58] D. S. Ripatti, T. R. Veltman, M. W. Kanan, *Joule* **2019**, *3*, 2581.
[59] F. He, M. Hou, F. Zhu, D. Liu, H. Zhang, F. Yu, Y. Zhou, Y. Ding, M. Liu, Y. Chen, *Adv. Energy Mater.* **2022**, *12*, 2202175.
[60] C. P. O'Brien, R. K. Miao, A. S. Zeraati, G. Lee, E. H. Sargent, D. Sinton, *Chem. Rev.* **2024**, *124*, 3648.
[61] a) X. Wang, H. Wang, L. Hu, B. Ge, L. Guo, Z. Yang, *J. Eur. Ceram. Soc.* **2023**, *43*, 6974; b) Y. Wang, C. R. Wu, B. F. Zu, M. Han, Q. Du, M. Ni, K. Jiao, *J. Power Sources* **2021**, *516*, 230660.
[62] M. Zhang, R. Ettelaie, T. Li, J. Yang, L. Dong, N. Xue, B. P. Binks, F. Cheng, H. Yang, *Nat. Catal.* **2024**, *7*, 295.
[63] a) Z. Liu, L. Song, X. Lv, M. Liu, Q. Wen, L. Qian, H. Wang, M. Wang, Q. Han, G. Zheng, *J. Am. Chem. Soc.* **2024**, *146*, 14260; b) J. Ding, F. Li, X. Ren, Y. Liu, Y. Li, Z. Shen, T. Wang, W. Wang, Y.-G. Wang, Y. Cui, H. Yang, T. Zhang, B. Liu, *Nat. Commun.* **2024**, *15*, 3641; c) N. Sakamoto, K. Sekizawa, S. Shirai, T. Nonaka, T. Arai, S. Sato, T. Morikawa, *Nat. Catal.* **2024**, *7*, 574.
[64] a) E. Shirzadi, Q. Jin, A. S. Zeraati, R. Dorakhan, T. J. Goncalves, J. Abed, B.-H. Lee, A. S. Rasouli, J. Wicks, J. Zhang, P. Ou, V. Boureau, S. Park, W. Ni, G. Lee, C. Tian, D. M. Meira, D. Sinton, S. Siahrostami, E. H. Sargent, *Nat. Commun.* **2024**, *15*, 2995; b) J. Hou, B. Xu, Q. Lu, *Nat. Commun.* **2024**, *15*, 1926; c) W. Deng, P. Zhang, Y. Qiao, G. Kastlunger, N. Govindarajan, A. Xu, I. Chorkendorff, B. Seger, J. Gong, *Nat. Commun.* **2024**, *15*, 892; d) C. Long, K. Wan, Y. Chen, L. Li, Y. Jiang, C. Yang, Q. Wu, G. Wu, P. Xu, J. Li, X. Shi, Z. Tang, C. Cui, *J. Am. Chem. Soc.* **2024**, *146*, 4632; e) S. Y. Lee, J. Kim, G. Bak, E. Lee, D. Kim, S. Yoo, J. Kim, H. Yun, Y. J. Hwang, *J. Am. Chem. Soc.* **2023**, *145*, 23068.
[65] a) S. Li, A. V. Nagarajan, D. R. Alfonso, M. Sun, D. R. Kauffman, G. Mpourmpakis, R. Jin, *Angew. Chem., Int. Ed. Engl.* **2021**, *60*, 6351; b) M. C. O. Monteiro, M. F. Philips, K. J. P. Schouten, M. T. M. Koper, *Nat. Commun.* **2021**, *12*, 4943; c) W. Choi, J. W. Park, W. Park, Y. Jung, H. Song, *Nanoscale* **2021**, *13*, 14346; d) W. Song, K. He, C. Li, R. Yin, Y. Guo, A. Nie, Y. Li, K. Yang, M. Zhou, X. Lin, Z.-J. Wang, Q. Ren, S. Zhu, T. Xu, S. Liu, H. Jin, J.-J. Lv, S. Wang, Y. Yuan, *Adv. Mater.* **2024**, *36*, 2312566; e) S. Li, X. Dong, J. Mao, W. Chen, A. Chen, G. Wu, C. Zhu, G. Li, Y. Wei, X. Liu, J. Wang, Y. Song, W. Wei, *Small* **2023**, *19*, 2301338; f) S. Li, X. Dong, Y. Zhao, J. Mao, W. Chen, A. Chen,

Y. Song, G. Li, Z. Jiang, W. Wei, Y. Sun, *Angew. Chem., Int. Ed. Engl.* **2022**, *61*, 202210432. g) X. Sheng, W. Ge, H. Jiang, C. Li, *Adv. Mater.* **2022**, *34*, 2201295; h) L. Lin, H. Li, Y. Wang, H. Li, P. Wei, B. Nan, R. Si, G. Wang, X. Bao, *Angew. Chem., Int. Ed. Engl.* **2021**, *60*, 26582.

[66] H. L. Zhu, J. R. Huang, M. D. Zhang, C. Yu, P. Q. Liao, X. M. Chen, *J. Am. Chem. Soc.* **2024**, *146*, 1144.

[67] J. Y. Kim, C. Sellers, S. Y. Hao, T. P. Senftle, H. T. Wang, *Nat. Catal.* **2023**, *6*, 1115.

[68] G. Liu, Y. Zhong, Z. Liu, G. Wang, F. Gao, C. Zhang, Y. Wang, H. Zhang, J. Ma, Y. Hu, A. Chen, J. Pan, Y. Min, Z. Tang, C. Gao, Y. Xiong, *Nat. Commun.* **2024**, *15*, 2636.

[69] W. Lai, Y. Qiao, J. Zhang, Z. Lin, H. Huang, *Energy Environ. Sci.* **2022**, *15*, 3603.

[70] S. Brückner, Q. Feng, W. Ju, D. Galliani, A. Testolin, M. Klingenhof, S. Ott, P. Strasser, *Nat. Chem. Eng.* **2024**, *1*, 229.

[71] D. J. D. Pimlott, A. Jewlal, Y. Kim, C. P. Berlinguette, *J. Am. Chem. Soc.* **2023**, *145*, 25933.

[72] M. Shen, L. Ji, D. Cheng, Z. Wang, Q. Xue, S. Feng, Y. Luo, S. Chen, J. Wang, H. Zheng, X. Wang, P. Sautet, J. Zhu, *Joule* **2024**, *8*, 1999.

[73] Z. S. Zhang, E. W. Lees, F. Habibzadeh, D. A. Salvatore, S. Ren, G. L. Simpson, D. G. Wheeler, A. Liua, C. P. Berlinguette, *Energy Environ. Sci.* **2022**, *15*, 705.

[74] X. Jiang, L. Ke, K. Zhao, X. Yan, H. Wang, X. Cao, Y. Liu, L. Li, Y. Sun, Z. Wang, D. Dang, N. Yan, *Nat. Commun.* **2024**, *15*, 1427.

[75] Z. Zhang, E. W. Lees, S. Ren, B. A. W. Mowbray, A. Huang, C. P. Berlinguette, *ACS Cent. Sci.* **2022**, *8*, 749.

[76] Z. Xu, C. Peng, G. Zheng, *Chem. - Eur. J.* **2023**, *29*, 202203147.

[77] X. Li, Q. Chen, W. Sun, C. He, Z. Wen, *Angew. Chem., Int. Ed. Engl.* **2024**, *63*, 202412410.

[78] X. Wang, P. H. Li, J. Tam, J. Y. Howe, C. P. O'Brien, A. S. Rasouli, R. K. Miao, Y. Liu, A. Ozden, K. Xie, J. Wu, D. Sinton, E. H. Sargent, *Nat. Sustain.* **2024**, *7*, 931

[79] A. Kormanyos, A. Szirmai, B. Endrodi, C. Janaky, *ACS Catal.* **2024**, *14*, 6503.

[80] W. Wu, H. Zhou, Y. Liu, Y. Pan, Q. Chen, Y. Zhang, J. Mao, W. Ma, P. Yu, *Nano Res.* **2025**, *18*, 94907051.

[81] Z. H. Pu, G. X. Zhang, A. Hassanpour, D. Zheng, S. Wang, S. Liao, Z. Chen, S. Sun, *Appl. Energy* **2021**, *283*, 116376.

[82] a) P. Wang, Y. Luo, G. Zhang, M. Wu, Z. Chen, S. Sun, Z. Shi, *Small* **2022**, *18*, 2105803; b) Z. Pu, T. Liu, G. Zhang, H. Ranganathan, Z. Chen, S. Sun, *ChemSusChem* **2021**, *14*, 4636.

[83] a) Z. Pu, T. Liu, G. Zhang, Z. Chen, D. Li, N. Chen, W. Chen, Z. Chen, S. Sun, *Adv. Energy Mater.* **2022**, *12*, 2200293; b) Y. Liu, L. Li, L. Wang, N. Li, X. Zhao, Y. Chen, T. Sakthivel, Z. Dai, *Nat. Commun.* **2024**, *15*, 2851.

[84] L. A. Cohen, M. S. Weimer, K. Yim, J. Jin, D. V. F. Alvarez, A. A. Dameron, C. B. Capuano, R. J. Ouimet, S. Fortiner, D. V. Esposito, *ACS Energy Lett.* **2024**, *9*, 1624.

[85] X. W. Lv, W. W. Tian, Z. Y. Yuan, *Electrochem. Energy Rev.* **2023**, *6*, 23.

[86] D. Simondson, M. Chatti, S. A. Bonke, M. F. Tesch, R. Golnak, J. Xiao, D. A. Hoogeveen, P. V. Cherepanov, J. L. Gardiner, A. Tricoli, D. R. MacFarlane, A. N. Simonov, *Angew. Chem., Int. Ed. Engl.* **2021**, *60*, 15821.

[87] a) J. W. Zhao, K. Yue, H. Zhang, S.-Y. Wei, J. Zhu, D. Wang, J. Chen, V. Y. Fominski, G.-R. Li, *Nat. Commun.* **2024**, *15*, 2928; b) J. Zhu, L. Xu, Z. Lyu, M. Xie, R. Chen, W. Jin, M. Mavrikakis, Y. Xia, *Angew. Chem., Int. Ed. Engl.* **2021**, *60*, 10384.

[88] S. Kong, A. Li, J. Long, K. Adachi, D. Hashizume, Q. Jiang, K. Fushimi, H. Ooka, J. Xiao, R. Nakamura, *Nat. Catal.* **2024**, *7*, 252.

[89] L. Tao, F. Lv, D. W. Wang, H. Luo, F. Lin, H. Gong, H. Mi, S. Wang, Q. Zhang, L. Gu, M. Luo, S. Guo, *Joule* **2024**, *8*, 450.

[90] K. Zhang, X. Liang, L. Wang, K. Sun, Y. Wang, Z. Xie, Q. Wu, X. Bai, M. S. Hamdy, H. Chen, X. Zou, *Nano Res. Energy* **2022**, *1*, 9120032.

[91] a) S. Li, T. Liu, W. Zhang, M. Wang, H. Zhang, C. Qin, L. Zhang, Y. Chen, S. Jiang, D. Liu, X. Liu, H. Wang, Q. Luo, T. Ding, T. Yao, *Nat. Commun.* **2024**, *15*, 3416; b) X. Zhong, L. Sui, M. Yang, T. Koketsu, M. Klingenhof, S. Selve, K. G. Reeves, C. Ge, L. Zhuang, W. H. Kan, M. Avdeev, M. Shu, N. Alonso-Vante, J. Chen, S. Haw, C. Pao, Y. Chang, Y. Huang, Z. Hu, P. Strasser, J. Ma, *Nat. Catal.* **2024**, *7*, 546.

[92] a) J. Nie, J. Shi, T. Huang, M.-Y. Xie, Z.-Y. Ouyang, M.-H. Xian, G.-F. Huang, H. Wan, W. Hu, W.-Q. Huang, *Adv. Funct. Mater.* **2024**, *34*, 2314172; b) G. S. Cassol, C. Shang, A. K. An, N. K. Khanzada, F. Ciucci, A. Manzotti, P. Westerhoff, Y. Song, L. Ling, *Nat. Commun.* **2024**, *15*, 2617.

[93] a) B. Zhang, J. Wang, G. Liu, C. M. Weiss, D. Liu, Y. Chen, L. Xia, P. Zhou, M. Gao, Y. Liu, J. Chen, Y. Yan, M. Shao, H. Pan, W. Sun, *Nat. Catal.* **2024**, *7*, 441; b) Y. Zhu, M. Klingenhof, C. Gao, T. Koketsu, G. Weiser, Y. Pi, S. Liu, L. Sui, J. Hou, J. Li, H. Jiang, L. Xu, W. Huang, C. Pao, M. Yang, Z. Hu, P. Strasser, J. Ma, *Nat. Commun.* **2024**, *15*, 1447.

[94] Y. Chen, Q. Li, Y. Lin, J. Liu, J. Pan, J. Hu, X. Xu, *Nat. Commun.* **2024**, *15*, 7278.

[95] a) A. Goyal, S. Louisia, P. Moerland, M. T. M. Koper, *J. Am. Chem. Soc.* **2024**, *146*, 7305; b) R. L. Fan, C. H. Liu, Z. H. Li, H. Huang, J. Feng, Z. Li, Z. Zou, *Nat. Sustain.* **2024**, *7*, 158; c) X. Lin, W. Hu, J. Xu, X. Liu, W. Jiang, X. Ma, D. He, Z. Wang, W. Li, L. Yang, H. Zhou, Y. Wu, *J. Am. Chem. Soc.* **2024**, *146*, 4883.

[96] S. Yang, Z. Zhang, A. M. Oliveira, S. Xi, M. Zhiani, J. Zhang, Z. Tu, F. Xiao, S. Wang, Y. Yan, J. Xiao, *Adv. Funct. Mater.* **2024**, *34*, 2313275.

[97] H. Wakayama, K. Yamazaki, *ACS Omega* **2021**, *6*, 4161.

[98] H. Cheng, H. Luo, X. Wang, Z. Pan, Q. Zhao, C. Dong, X. Li, *Int. J. Hydrogen Energy* **2023**, *48*, 38557.

[99] J. H. Choi, H. E. Kang, D. J. Kim, Y. S. Yoon, *Chem. Eng. J.* **2024**, *493*, 152662.

[100] T. Liu, Y. K. Tao, Y. L. Wang, M. Q. Hu, Z. Zhang, J. Shao, *Fuel* **2024**, *368*, 131610.

[101] E. Taibi, H. Blanco, R. Miranda, M. Carmo, *Green Hydrogen Cost Reduction: Scaling up Electrolysers to Meet the 1.5^0C Climate Goal*, International Renewable Energy Agency, Masdar City, Abu Dhabi **2020**.

[102] Q. Xu, L. Zhang, J. Zhang, J. Zhang, J. Wang, Y. Hu, H. Jiang, C. Li, *EnergyChem* **2022**, *4*, 100087.

[103] H. Teuku, I. Alshami, J. Goh, M. S. Masdar, K. S. Loh, *Int. J. Energy Res.* **2021**, *45*, 20583.

[104] L. Messing, K. Pellumbi, L. Hoof, N. Imming, S. Wilbers, L. Kopietz, M. Joemann, A. Grevé, K. Puring, U. Apfel, *Adv. Energy Mater.* **2024**, *14*, 2402308.

[105] H. Li, H. Nakajima, A. Inada, K. Ito, *Int. J. Hydrogen Energy* **2018**, *43*, 8600.

[106] A. H. Hassan, Z. Liao, K. Wang, F. Xiao, C. Xu, M. M. Abdelsamie, *Int. J. Hydrogen Energy* **2024**, *49*, 1060.

[107] X. Hu, B. Hu, C. Niu, J. Yao, M. Liu, H. Tao, Y. Huang, S. Kang, K. Geng, N. Li, *Nat. Energy* **2024**, *9*, 401.

[108] Z. Shi, X. Zhang, X. Lin, G. Liu, C. Ling, S. Xi, B. Chen, Y. Ge, C. Tan, Z. Lai, Z. Huang, X. Ruan, L. Zhai, L. Li, Z. Li, X. Wang, G.-H. Nam, J. Liu, Q. He, Z. Guan, J. Wang, C.-S. Lee, A. R. J. Kucernak, H. Zhang, *Nature* **2023**, *621*, 300.

[109] T. Leo, How Does an Electrolyzer Work?, https://www.fuelcellenergy.com/blog/how-does-an-electrolyzer-work (accessed: July 2024).

[110] J. Kim, A. Jun, O. Gwon, S. Yoo, M. Liu, J. Shin, T.-H. Lim, G. Kim, *Nano Energy* **2018**, *44*, 121.

[111] L. A. Jolaoso, I. T. Bello, O. A. Ojelade, A. Yousuf, C. Duan, P. Kazempoor, *Int. J. Hydrogen Energy* **2023**, *48*, 33017.

[112] F. Energy, 2023 Sustainability Report, https://go.fuelcellenergy.com/hubfs/fuelcell-energy-2023-sustainability-report.pdf (accessed: November 2024).

[113] L. Zhang, X. Yang, Q. Yuan, Z. Wei, J. Ding, T. Chu, C. Rong, Q. Zhang, Z. Ye, F.-Z. Xuan, Y. Zhai, B. Zhang, X. Yang, *Nat. Commun.* **2023**, *14*, 8311.

[114] E. P. Delmo, Y. Wang, Y. Song, S. Zhu, H. Zhang, H. Xu, T. Li, J. Jang, Y. Kwon, Y. Wang, M. Shao, *J. Am. Chem. Soc.* **2024**, *146*, 1935.

[115] a) J. E. N. Swallow, E. S. Jones, A. R. Head, J. S. Gibson, R. B. David, M. W. Fraser, M. A. van Spronsen, S. Xu, G. Held, B. Eren, R. S. Weatherup, *J. Am. Chem. Soc.* **2023**, *145*, 6730; b) H. T. Wang, A. Ghosh, C. H. Wang, S. H. Hsieh, Y. C. Shao, J. W. Chiou, C. L. Chen, C. W. Pao, J. F. Lee, Y. S. Liu, Y. D. Chuang, J. H. Guo, M. K. Wu, W. F. Pong, *Proc. Natl. Acad. Sci. U. S. A.* **2019**, *116*, 22458.

[116] M. L. Frisch, L. Wu, C. Atlan, Z. Ren, M. Han, R. Tucoulou, L. Liang, J. Lu, A. Guo, H. N. Nong, A. Arinchtein, M. Sprung, J. Villanova, M.-I. Richard, P. Strasser, *Nat. Commun.* **2023**, *14*, 7833.

[117] A. Martini, D. Hursán, J. Timoshenko, M. Rüscher, F. Haase, C. Rettenmaier, E. Ortega, A. Etxebarria, B. R. Cuenya, *J. Am. Chem. Soc.* **2023**, *145*, 17351.

[118] D. Hursán, J. Timoshenko, E. Ortega, H. S. Jeon, M. Rüscher, A. Herzog, C. Rettenmaier, S. W. Chee, A. Martini, D. Koshy, B. R. Cuenya, *Adv. Mater.* **2024**, *36*, 2307809.

[119] S. Toleukhanova, T. H. Shen, C. Chang, S. Swathilakshmi, T. B. Montandon, V. Tileli, *Adv. Mater.* **2024**, *36*, 2311133.

[120] Y. Yang, S. Louisia, S. Yu, J. Jin, I. Roh, C. Chen, M. V. F. Guzman, J. Feijóo, P.-C. Chen, H. Wang, C. J. Pollock, X. Huang, Y.-T. Shao, C. Wang, D. A. Muller, H. D. Abruña, P. Yang, *Nature* **2023**, *614*, 262.

[121] Y. Li, Y. Liu, Z. Zhang, W. Zhou, J. Xu, Y. Ye, Y. Peng, X. Xiao, W. Chiu, R. Sinclair, Y. Li, Y. Cui, *Nano Lett.* **2024**, *24*, 10409.

[122] X. Lu, C. Zhou, R. S. Delima, E. W. Lees, A. Soni, D. J. Dvorak, S. Ren, T. Ji, A. Bahi, F. Ko, C. P. Berlinguette, *Nat. Chem.* **2024**, *16*, 979.

[123] Z. Lian, F. Dattila, N. López, *Nat. Catal.* **2024**, *7*, 401.

[124] D. Xi, A. M. Alfaraidi, J. Gao, T. Cochard, L. C. I. Faria, Z. Yang, T. Y. George, T. Wang, R. G. Gordon, R. Y. Liu, M. J. Aziz, *Nat. Energy* **2024**, *9*, 479.

[125] Y. B. Zhao, Z. J. Niu, J. W. Zhao, L. Xue, X. Z. Fu, J. L. Long, *Electrochem. Energy Rev.* **2023**, *6*, 14.

[126] Á. Balog, E. Kecsenovity, G. F. Samu, J. He, D. Fekete, C. Janáky, *Nat. Catal.* **2024**, *7*, 522.

[127] M. Ronovský, M. Myllymäki, Y. Watier, P. Glatzel, P. Strasser, A. M. Bonastre, J. Drnec, *J. Power Sources* **2024**, *592*, 233906.

[128] C. Zhang, X. Hao, J. Wang, X. Ding, Y. Zhong, Y. Jiang, M.-C. Wu, R. Long, W. Gong, C. Liang, W. Cai, J. Low, Y. Xiong, *Angew. Chem., Int. Ed. Engl.* **2024**, *63*, 202317628.

[129] F. Y. Chen, A. Elgazzar, S. Pecaut, C. Qiu, Y. Feng, S. Ashokkumar, Z. Yu, C. Sellers, S. Hao, P. Zhu, H. Wang, *Nat. Catal.* **2024**, *7*, 1032.

[130] a) Government of Canada, Chemical Manufacturing through Electrochemical Carbon Dioxide Utilization, https://natural-resources.canada.ca/funding-partnerships/chemical-manufacturing-through-electrochemical-carbon-dioxide-utilization (accessed: April 2025); b) CERT Systems, Essential Chemicals without Fossil Fuels, https://co2cert.com/about-2/ (accessed: April 2025).

[131] Air Liquide, Inauguration of the World's Largest PEM Electrolyzer to Produce Decarbonized Hydrogen, https://www.airliquide.com/stories/industry/inauguration-worlds-largest-pem-electrolyzer-produce-decarbonized-hydrogen#:H:text=The%20new%20electrolyzer%2C%20located%20at,%20currently%20operating%20in%20the%20world (accessed: April 2025).

[132] R. B. Kutz, Q. M. Chen, H. Z. Yang, S. D. Sajjad, Z. C. Liu, I. R. Masel, *Energy Technol.* **2017**, *5*, 929.

[133] S. Huang, Y. Zhao, X. Wang, J. Shi, S. Yao, D. Osinkin, *Int. J. Energy Res.* **2025**, 5554089.

[134] a) J. Timoshenko, A. Bergmann, C. Rettenmaier, A. Herzog, R. M. Arán-Ais, H. S. Jeon, F. T. Haase, U. Hejral, P. Grosse, S. Kühl, E. M. Davis, J. Tian, O. Magnussen, B. Roldan Cuenya, *Nat. Catal.* **2022**, *5*, 259; b) H. Liu, T. Yan, S. Tan, L. Sun, Z. Zhang, S. Hu, S.-H. Li, X. Kang, Y. L. Jiang, T. Hou, L. Liu, Q. Yu, B. Liu, *J. Am. Chem. Soc.* **2024**, *146*, 5333.

[135] M. Ronovský, O. Dunseath, T. Hrbek, P. Kúš, M. Gatalo, S. Polani, J. Kubát, D. Götz, H. Nedumkulam, A. Satori, E. Petrucco, F. R. Zepeda, N. Hodnik, P. Strasser, A. M. Bonastre, J. Drnec, *ChemRxiv* **2024**, *2*, https://doi.org/10.26434/chemrxiv-2024-g9lx2-v2.

[136] L. Li, C. Wan, S. Wang, X. Li, Y. Sun, Y. Xie, *Nano Lett.* **2024**, *24*, 2392.

[137] X. Gao, P. Wang, X. Sun, M. Jaroniec, Y. Zheng, S. Qiao, *Angew. Chem., Int. Ed. Engl.* **2024**, *64*, 202417987.

[138] X. Liu, M. T. M. Koper, *J. Am. Chem. Soc.* **2024**, *146*, 5242.

[139] S. K. Nabil, M. A. M. Raghuman, K. Kannimuthu, M. Rashid, H. S. Shiran, M. G. Kibria, M. A. Khan, *Nat. Catal.* **2024**, *7*, 330.

[140] F. Habibzadeh, P. Mardle, N. Zhao, H. D. Riley, D. A. Salvatore, C. P. Berlinguette, S. Holdcroft, Z. Shi, *Electrochem. Energy Rev.* **2023**, *6*, 26.

[141] D. A. Salvatore, C. M. Gabardo, A. Reyes, C. P. O'Brien, S. Holdcroft, P. Pintauro, B. Bahar, M. Hickner, C. Bae, D. Sinton, E. H. Sargent, C. P. Berlinguette, *Nat. Energy* **2021**, *6*, 339.

[142] Q. Liu, T. Tang, Z. Tian, S. Ding, L. Wang, D. Chen, Z. Wang, W. Zheng, H. Lee, X. Lu, X. Miao, L. Liu, L. Sun, *Nat. Commun.* **2024**, *15*, 6722.

[143] H. Lei, X. Yang, Z. Chen, D. Rawach, L. Du, Z. Liang, D.-S. Li, G. Zhang, A. C. Tavares, S. Sun, *Adv. Mater.* **2025**, *37*, 2410106.

[144] X. Liu, N. Xie, J. Xue, M. Li, C. Zheng, J. Zhang, Y. Qin, Y. Yin, D. R. Dekel, M. D. Guiver, *Nat. Energy* **2022**, *7*, 329.

[145] L. Zhu, Y. Li, P. Ye, J. Zhao, J. Liu, J. Lei, L. Wang, R. Xue, *Adv. Funct. Mater.* **2022**, *33*, 2210453.

[146] Q. Liang, Y. Huang, Y. Guo, X. Zhang, X. Hu, H. Zeng, K. Liang, D. Zhao, L. Jiang, B. Kong, *Nat. Sustain.* **2024**, *7*, 628.

Zhangsen Chen obtained his B.S. degree at Fuzhou University in 2014, a Master's degree in physical chemistry from the Research Institute of Photocatalysis, Fuzhou University, in 2017, and a Ph.D. degree in energy and material science from Institut National de la Recherche Scientifique (INRS), University of Québec, in 2023. He is now a postdoctoral fellow at Prof. Shuhui Sun's group at INRS-EMT. His current research interests focus on the development of advanced nanomaterials and their applications in H_2 production and CO_2 conversion to value-added chemicals and fuels.

Lei Zhang is a senior research officer at the National Research Council Canada. She is a Fellow of the Canadian Academy of Engineering (CAE). Her main research interests include electrocatalysis and advanced materials for energy conversion and storage, including PEM fuel cells, supercapacitors, batteries, and CO_2 reduction.

Shuhui Sun is a full professor at the Institut National de la Recherche Scientifique (INRS), Canada. He is a Fellow of both the Royal Society of Canada (RSC) and the Canadian Academy of Engineering (CAE). His current research interests focus on multifunctional nanomaterials for energy conversion and storage applications, including H_2 fuel cells, metal-ion (Li^+, Na^+, Zn^{2+}) batteries, lithium–metal batteries, metal–air batteries, solid-state batteries, etc. He is also interested in nanostructured photo- and electro-catalysts for H_2 production, CO_2 reduction, and water treatment.

Gaixia Zhang is a professor and Canada Research Chair on Energy Devices for Sustainability at École de Technologie Supérieure (ÉTS), University of Québec, Montréal, Canada. She received her Ph.D. degree from Polytechnique Montréal, and then continued her research at Western University and INRS, Canada. Her research interests focus on advanced materials (catalysts, electrodes, and electrolytes) for sustainable energy conversion and storage applications, including batteries, fuel cells, hydrogen production, and CO_2 reduction. She is also interested in interface and device engineering, as well as in situ characterizations and theoretical simulations.